Pittsburg State University
Pittsburg State University Digital Commons

Electronic Thesis Collection

5-2016

ELECTROSPUN NANOFIBERS OF METAL OXIDES FOR ENERGY STORAGE APPLICATIONS

Sara Alkhalaf
Pittsburg State University

Follow this and additional works at: https://digitalcommons.pittstate.edu/etd

 Part of the Chemistry Commons, and the Physics Commons

Recommended Citation

Alkhalaf, Sara, "ELECTROSPUN NANOFIBERS OF METAL OXIDES FOR ENERGY STORAGE APPLICATIONS" (2016). *Electronic Thesis Collection*. 95.
https://digitalcommons.pittstate.edu/etd/95

This Thesis is brought to you for free and open access by Pittsburg State University Digital Commons. It has been accepted for inclusion in Electronic Thesis Collection by an authorized administrator of Pittsburg State University Digital Commons. For more information, please contact mmccune@pittstate.edu, jmauk@pittstate.edu.

ELECTROSPUN NANOFIBERS OF METAL OXIDES FOR ENERGY STORAGE APPLICATIONS

A Thesis Submitted to the Graduate School
In Partial Fulfillment of the Requirements
For The Degree of Master of Science

Sara Alkhalaf

Pittsburg State University

Pittsburg, Kansas

May, 2016

ELECTROSPUN NANOFIBERS OF METAL OXIDES
FOR ENERGY STORAGE APPLICATIONS

Sara Alkhalaf

APPROVED:

Thesis Advisor _____
Dr. Ram Gupta, Chemistry Department

Committee Member _____
Dr. Khamis Siam, Chemistry Department

Committee Member _____
Dr. Pawan Kahol, Physics Department

Committee Member _____
Dr. John Franklin, English and Modern Languages Department

ACKNOWLEDGEMENTS

First of all, I would like to thank my mother and husband for their support and great patience at all times.

I would like to thank my advisor Dr. Ram Gupta for his guidance and motivation to achieve this work. I would like to thank him for his teaching and for his patience to improve my skills. Without his help, I could not have done this thesis or completed my master's degree.

In addition, I would like to express my sincere thanks to all my committee members Dr. Khamis Siam, Dr. Pawan Kahol and Dr. John Franklin and other faculty members in the Chemistry Department at Pittsburg State University. Also, I would like to thank Dr. Sanjay Mishra from Memphis University, Memphis for recording SEM and EDX images.

ELECTROSPUN NANOFIBERS OF METAL OXIDES FOR ENERGY STORAGE APPLICATIONS

An Abstract of the Thesis By
Sara Alkhalaf

Supercapacitors are considered the most prominent and efficient energy storage devices, next to lithium ion batteries due to their high power densities, fast charge-discharge capabilities and long cyclibility. Supercapacitors possess high power density in comparison to batteries and these are able to solve the increasing demand for energy in small consumer products, electrical vehicles and devices where quick power delivery is highly desired. Supercapacitors are classified into two categories based on their charge storage mechanism. The first group capacitors are called electrical double-layer capacitors (EDLCs), where the charge is stored at the interface. The second group is recognized as redox electrochemical capacitors (pseudocapacitors), where the charge storage arises due to Faradaic reactions at electrode/electrolyte interface. Although pseudocapacitors have higher charge storage capacity compard to EDLCs they suffer from high cost and poor cyclic stability. Since the charge-storage capacity of pseudocapacitors largely depends on the redox process at the electrode/electrolyte interface, their performance, which could be improved by using nano-structured redox active materials.

Nanostructured materials have attracted considerable research interest for their applications as catalyst, energy storage, fuel cells, etc. The main objective of this work is to synthesize and characterize nanofibers of metal oxides using electrospun technique

and use them for energy storage applications. Various metal oxides such as $NiMn_2O_4$, $CoMn_2O_4$ and $ZnMn_2O_4$ were prepared as 1 dimensional (1-D) architecture using processable polymers and metal salts. The synthesized nanofibers were structurally and electrochemically characterized. The supercapacitive performance of these nanofibers was examined using cyclic voltammetry (CV) and galvanostatic charge-discharge techniques. The $CoMn_2O_4$ nanofibers showed a promising value of ~ 120 F/g in 3M NaOH. The effect of different electrolytes such as LiOH, NaOH and KOH on the electrochemical properties of these metal oxide nanofibers was also investigated. It was observed that the charge storage capacity depends on the electrolyte used. The supercapacitor device fabricated using these nanofibers showed that charge storage capacity increases with increase in temperature. Our results suggest that electrospun nanofibers could be used for energy storage applications.

TABLE OF CONTENTS

LIST OF TABLES

LIST OF FIGURES

CHAPTER I

INTRODUCTION

The increasing number of people around the world has caused the demand for sources of energy in all forms to grow from simple and easy to complex. Everyone needs a power source because all the technological developments, such as cell phones and computers, require a power source to work. That is why improvements are needed to develop the sources of energy storage to meet our needs.

The simplest sources of energy includes coal and petroleum, but there are also non-conventional sources such as solar, hydro and wind. Solar light, hydro power and wind energy are very environment-friendly energy sources which are attracting tremendous research interest. Among these non-conventional energy resources, the solar cell is most popular because it is high efficiency, low cost and easy to manufacture. Solar cells convert solar light coming from the sun to earth into electricity. Solar cells are also called photovoltaic devices. Solar cells can be divided into three generations based on the materials used for their fabrication. First generation solar cells used silicon wafers. Second generation solar cells used amorphous silicon instead of silicon wafers.

Third generation solar cells used a variety of different materials such as small molecules and polymers.

The other common environmentally-friendly energy sources are hydro-energy and wind energy. Hydro-energy uses the force of water to generate energy in various ways, such as small hydro, micro hydro, conventional hydroelectric, run of the river hydroelectricity and pumped storage hydroelectricity. Wind powered devices, such as a wind turbine, can generate energy using the force of wind. For any practical applications, we need to store the generated energy so that it can be used when needed. Batteries, fuel cells and capacitors are the most commonly used energy storage devices. Supercapacitors provide high power density,are safer then batteries and have long cycle life.

This thesis will discuss the materials that store and save energy, such as batteries and supercapacitors. A battery is a device consisting of two or more electrochemical cells that convert stored chemical energy into electrical energy. There are two types of batteries. The first type is the primary (single use) batteries, such as alkaline batteries; and, the second type is rechargeable batteries, such as lithium-ion batteries. Batteries come in many shapes and sizes, from miniature cells to battery banks the size of a room [1].

Supercapacitors, which sometimes are called ultra-capacitors or electric double-layer capacitors (EDLC), are a high-capacity electrochemical capacitor with capacitance values much higher than others (but lower voltage limits) that bridge the gap between electrolytic capacitors and rechargeable batteries.

These unique properties of supercapacitor come from the interactions of the internal materials and from the basis of ways to store the electrical energy. Supercapacitor can be divided into three groups based on the charge storage mechanism. The first one is electrical double-layer capacitance (EDLC); the second one is electrochemical pseudocapacitance; and, the third one is hybrid capacitors. The classification of the capacitors and most commonly used materials to fabricate them is shown in Figure 1.1.

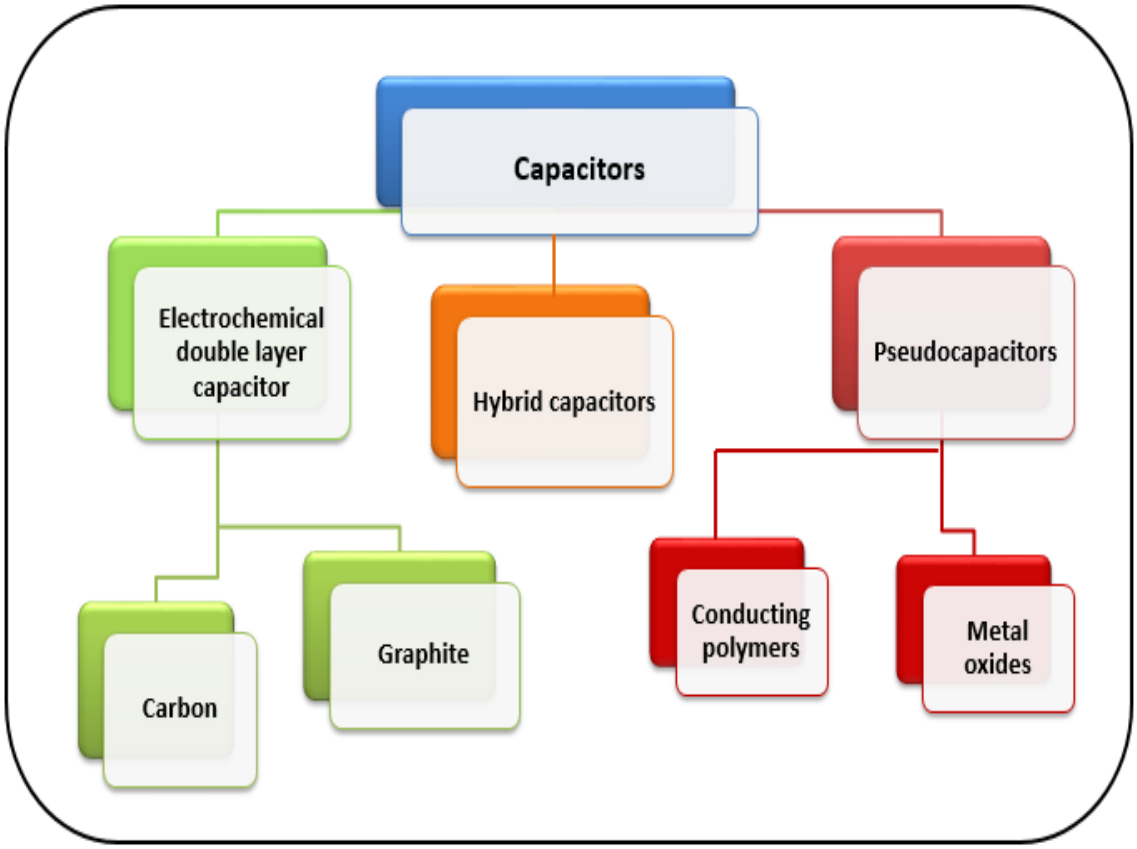

Figure 1.1: Types of supercapacitors and materials used.

1.1 Electric double-layer capacitors (EDLC):

The electrochemical double-layer capacitor (EDLC), exploits the double-layer of charge formed when voltage is applied to an electrode immersed in an electrolyte. Further, the electrodes of an EDLC are constructed of highly porous carbon, resulting in a very large surface area to volume ratio. As given below, the capacitance of any material is propositional to its surface area:

$$C = \epsilon A/d \quad \text{.....(1)}$$

where, C is the capacitance, ε is the dielectric constant and d is the distance between the two electrodes. Therefore, carbon based materials having large surface areas could provide EDLC with very high capacitance [2]. The mechanism of ion absorption and desorption to the electrical double layer contributes to the charge and discharge of EDLC. EDLC is charged by applying voltage to the fronting electrodes. During this process, ions are drawn to the surface of the electrode forming an electrical double layer. Equally, they move away when discharging EDLC.

EDLC consists of electrodes, an electrolyte, and a separator. The separator acts as in ion transporting layer and avoids short circuit between the two electrodes. Electrodes are generally fabricated by pasting carbon based materials on electrically conducting electrodes. The electrical double layer is formed on the surface of the electrode where each carbon powder connects with an electrolyte [3].

1.2. Pseudocapacitors:

The second most common capacitor is pseudocapacitor. Pseudocapacitors store electrical energy by electron charge transfer (redox process) between the electrode and electrolyte. This is accomplished through reduction-oxidation reactions and intercalation processes [4] [5] [6].

A good electrode used in a pesudocapacitor depends on two things: redox reactions, and intercalation or electro sorption. These two things also strongly depend on the chemical affinity of electrode materials to the ions adsorbed on the electrode surface as well as on the structure of the electrodeand the pores size[7].

Electrochemical pseudocapacitors use metal oxide and/or conductive polymer as electrode materials. The materials that show good redox behavior are transition-metal oxides like RuO_2, IrO_2, MnO_2. Also, conductive electrode materials such as active carbon, and conducting polymers such as polyaniline or derivatives of polythiophene cover the electrode material[8].

The advantage for pseudocapacitors is that they have a high charge storage capacity; but, the efficient materials such RuO_2 are expensive.

1.3. Hybrid Capacitors:

The principal store in hybrid capacitore uses asymmetric electrodes, one electrostatic and the other electrochemical, such as lithium-ion capacitors .In other words,a hybrid capacitor stores the energy by both the electrical double-layer capacitors (EDLC) principle and pseudocapacitors principle and therefore delivers higher charge storage capacity than the (ECLC) and pseudocapacitors [9].

The properties of hybrid capacitor are high cell capacity, because of the large anode capacity; high energy density; high power density; high reliability; operating temperatures ranging from −20 °C to 70 °C; and, low self-discharge [10].

Hybrid capacitors fit different applications which require a high energy density, high power densities and excellent stability as shown in Figure 1.2. Meanwhile they have both high energy density and high power density, so there is no need for other electrical storage devices in many kinds of applications, causing a reduction in cost.

Hybrid capacitors can be used for energy storage using wind power generation systems, uninterruptible power source systems (UPS), voltage sag compensation, photovoltaic power generation, energy recovery systems in industrial machinery, and transportation systems.

There are advantages and disadvantages of supercapacitors. They charge more simply and faster than batteries. They have a long cycle life and the charge is controllable. In addition, the supercapacitor provides high power density and they have wide range of operating temperatures. However, their energy density is low but they deliver their power very quickly. Also the self-discharge is high and supercapacitors require cell balancing.

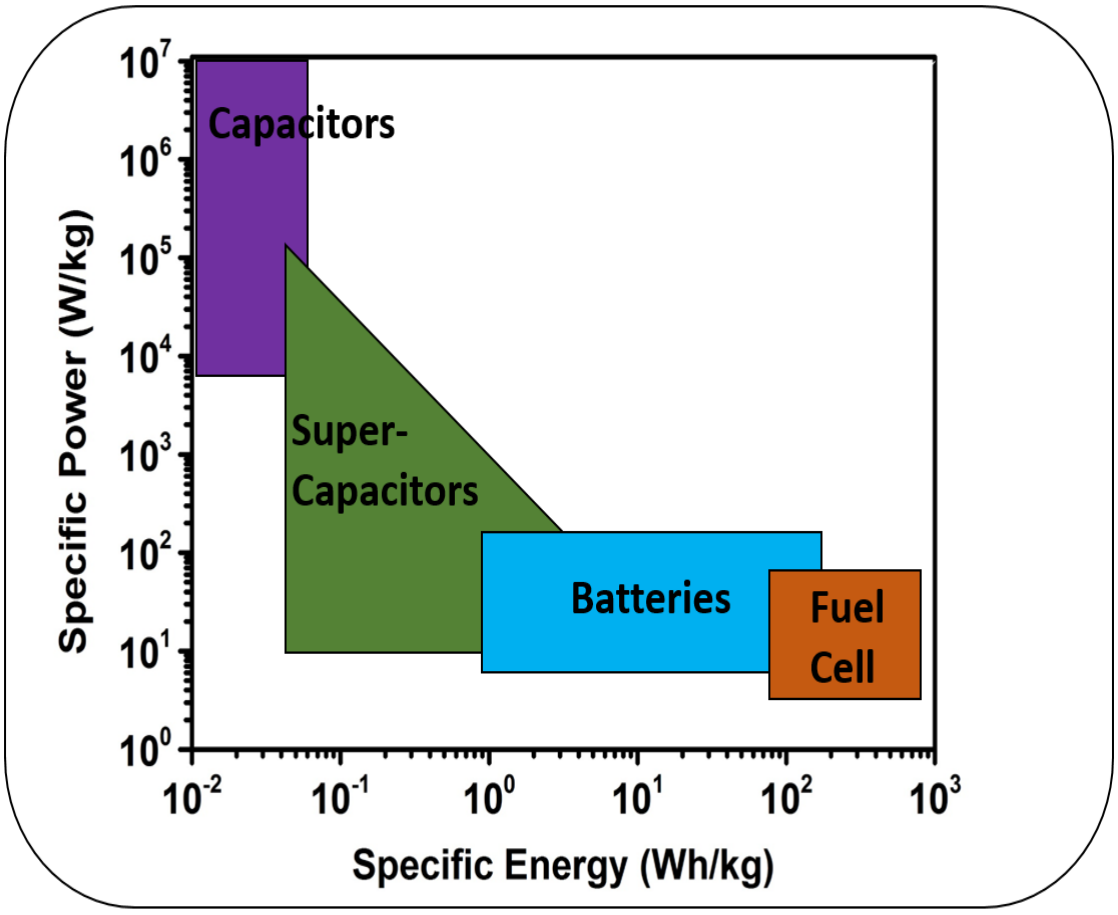

Figure 1.2: Ragone plot of common energy storage devices.

1.4 Nanofibers:

A nanofiber, as shown in Figure 1.3, is a fiber with a diameter of 100 nanometers or less. The nanofiber has unique properties such as high surface area, small pore size and high pore volume. These characteristics makes them an interesting field for researchers and companies to using this material in various applications such as in biomedical, energy and catalyst [11].

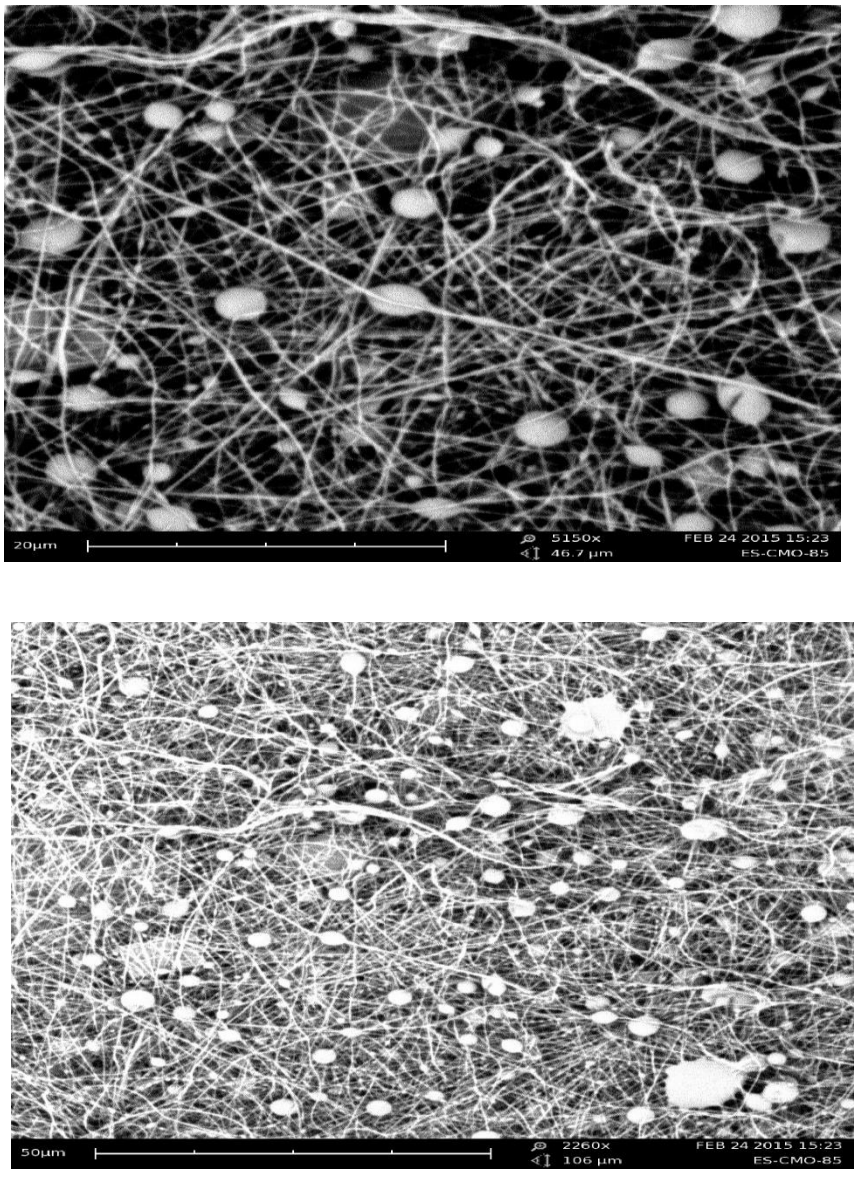

Figure 1.3: $CoMn_2O_4$ nanofibers at various magnifications.

Some examples of uses of nanofibers include capturing individual cancer cells circulating in the blood stream; using them as binder for fractured bones and as drug delivery; in batteries and supercapacitors; and, using them to make sensors for chemical gasses. Nanofibers are made in several ways, such as Drwaing, Template Synthesis, Phase Separation, Self-Assembly and Electrospining [12].

1.4.1 Drawing:

This process occurs by using a micropipette. First a drop from the fiber's soloution is placed on a plate, then a micropipette is dipped into the droplet. After that, the micropipette is pulled extremely quickly to make nanofibers as shown in Figure 1.4. This process is repeated many times with every droplet. The disadvantage in this method is that when the drop evaporation increases, the viscosity increases too [12].

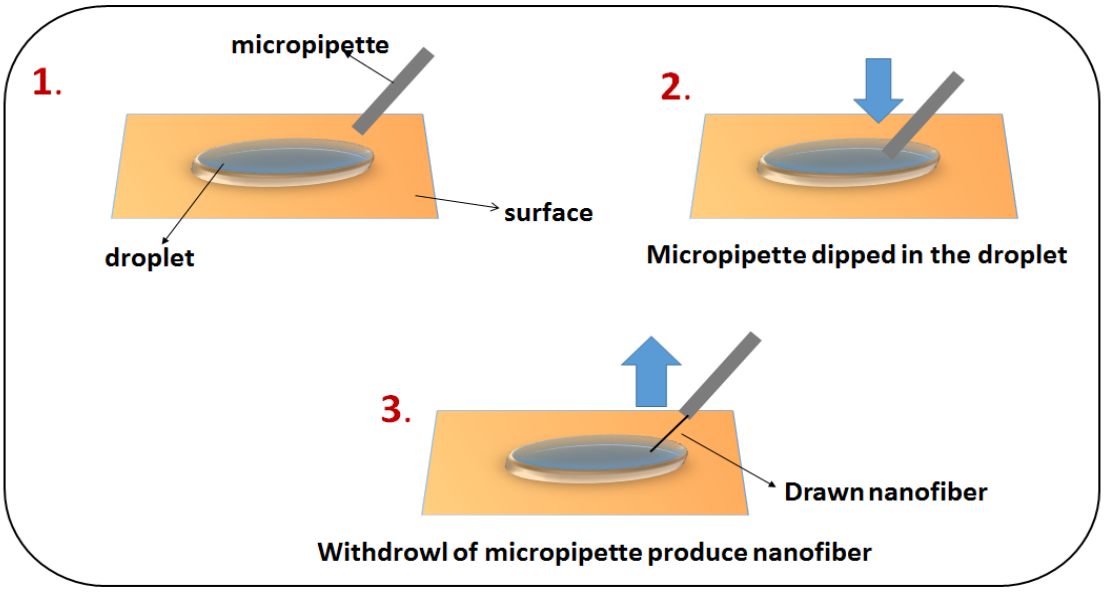

Figure 1.4: Obtaining nanofiber by drawing.

1.4.2 Template Synthesis:

In this method the main principle is to use the template to get desired nanofibers. The template basically contains four layers, which are water; a polymer solution; metal oxide that has nano pores; and, solidification solution. When pressure is applied on the water layer, it will push the polymer solution towards the metal oxide nano pores, which causes the nanofibers, as shown in Figure 1.5 [12].

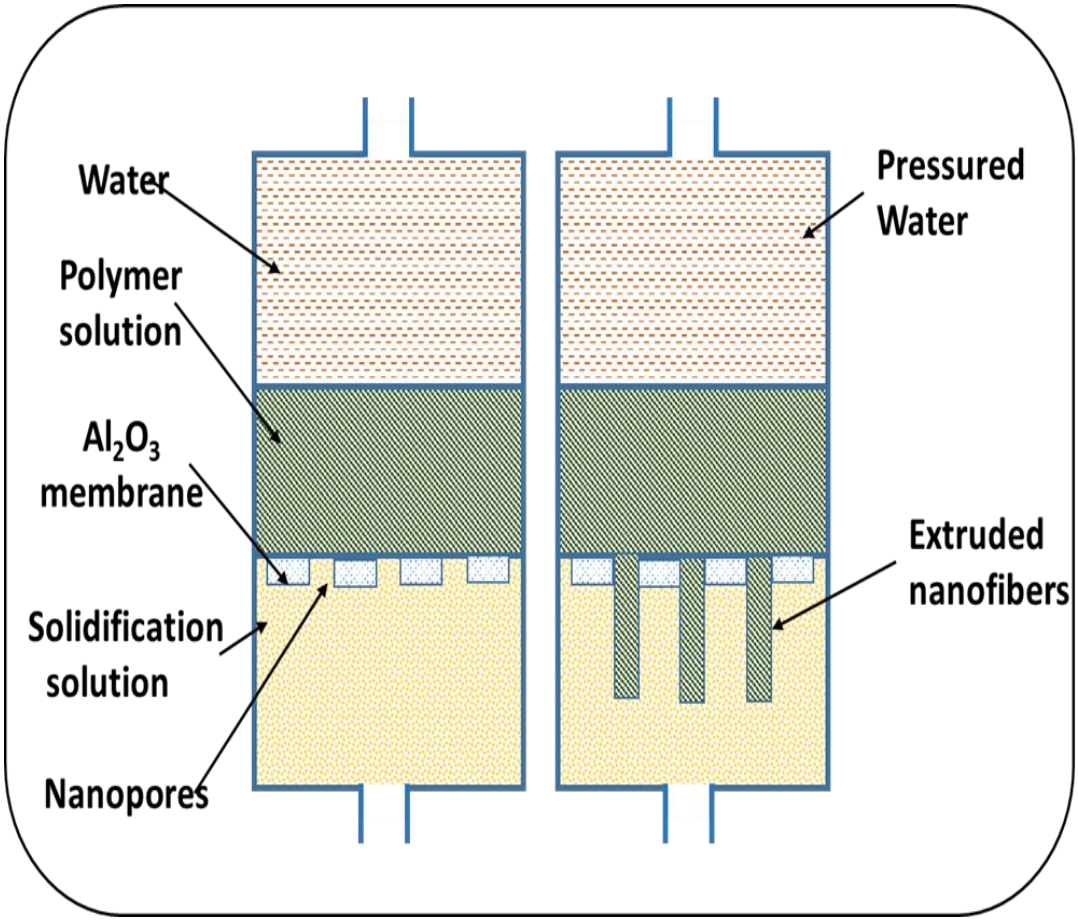

Figure 1.5: obtaining nanofibers by template synthesis.

1.4.3 Phase Separation:

This technique includes five steps: first, polymer dissolution; second, gelation; third, solvent extraction; fourth freezing; and, finally freeze-drying . First, the polymer is mixed with tetrahydrofuran to make the solution; then, the solution is stirred for two hours at 60° C to obtain a homogeneous solution. In the second step, 2 ml of the previous solution is transferred into a Teflon vial then put in the refrigerator to set on gelation temperature for 2 hours. The third step is putting the vial that has the gel into purified water for two days and changing it three times per day. Fourth, the vial is taken from the water then poured through filter paper then put into a freezer for two hours. Finally, the frozen gel goes to a freeze-drying vessel under vacuum for one week [12].

1.4.4 Self Assembly:

The main key for this method is using tiny molecules and building them up, because the intermolecular forces which make the smaller molecules close to each other and the architecture of the tiny molecules will determine the overall structure of the macromolecular nanofiber [12].

1.4.5 Electrospinning:

Electrospinning is a process that makes nanofibers by applying an electrical field on the polymer solution. This method in the simplest of the techniques and contains three main parts: the first part is a plastic syringe with a stainless steel needle that will hold the polymer solutions; the second part is a high voltage power source which creates an electrical field between the polymer solution and collector; and, the third part is an

aluminum plate as a collector for nanofibers. The polymer drops from the tip of the needle were drawn into the fibers due to the high voltage as shown in Figure 1.6. The distance between the needle tip and the collector should be not too small to create sparks between the aluminum plate and the stainless steel needle and should be large enough to evaporate the solvent in time for the nanofibers to form [12].

There are a lot of advanteges of electrospinning such as wide variety of polymers and materials have been used to form nanofibers, high surface area to volume ratio, low start up cost, variety of nanofibers structures have been constructed, and, doesn't take long time.

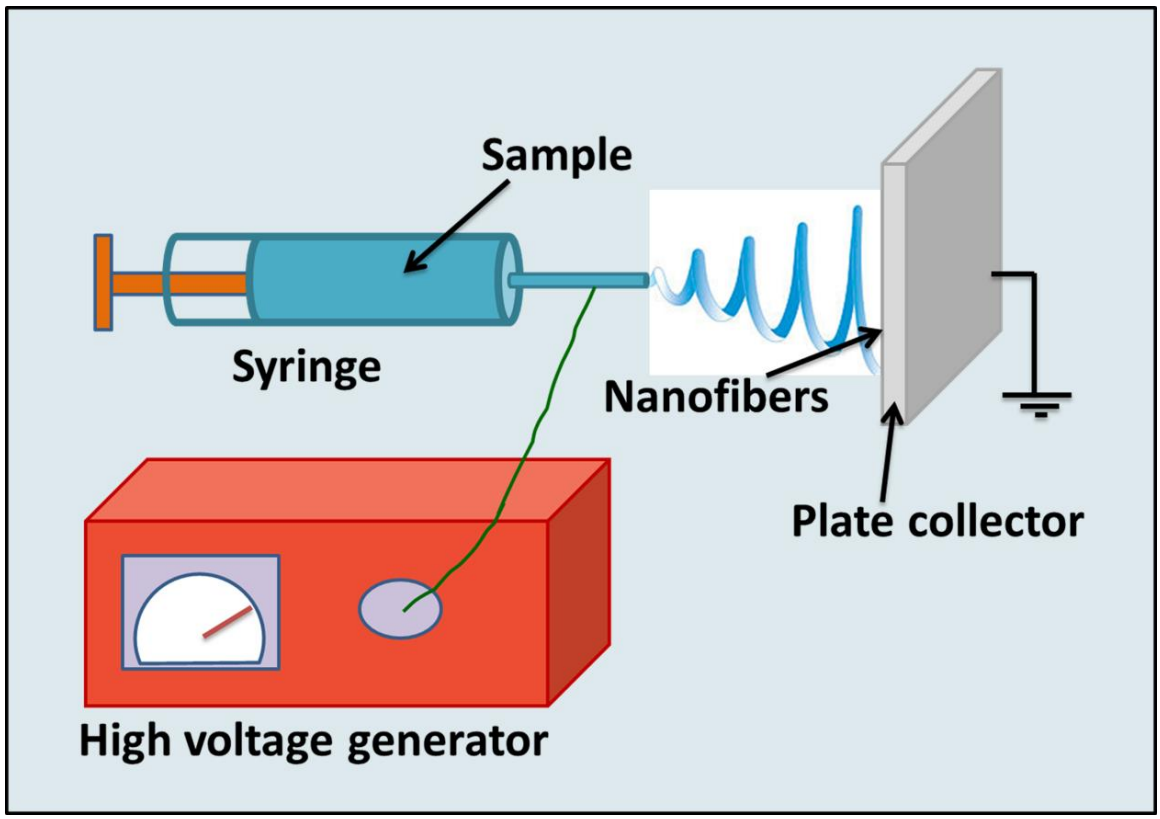

Figure 1.6: Schematics of electrospinning technique.

1.5 literature survey :

Because of the importance of metal oxide in the pseudocapacitor applications, we will take a look what has been done in the previous studies for $CoMn_2O_4$, $NiMn_2O_4$ and $ZnMn_2O_4$.

Shengjie Peng [13], found that "the ideal method to synthesize (1D) spinel composite oxides by electrospining is by adjusting the heating rates,"because the heating rates controlled the nanofiber structure.

Eunhee Lee [14], prepared electrospun nanofibers (NFs) from a poly(N-vinylpyrrolidone)/manganese (II) acetate com- posite by electrospinning for application in supercapacitors. TheRE WAS extraordinary performance for the unique three-dimensional morphology (solid 1D , tube in tube and nanotube) and the reduced interfacial resistance of the mixed-phase MnOx NFs within the matrix electrode and the electrolyte.

Bo Ren [15], found that "the NiO/CA nanofibers have good electrochemical reversibility and display superior capacitive performance with large capacitance," which is 2.5 times of NiO electrodes. Furthermore, the NiO/CA nanofibers display excellent cyclic performance after 1000 cycles.

Yongzhi Wu [16], concluded that the thermal sponsored electrospinning was applied for the fabrication of Ni/Ru embedded carbon nanofibers. Cyclic voltammetry results showed main peak voltages values during cathodic and anodic scans, individually. Also he made hybrid supercapacitors with activated carbon and in non-

aqueous electrolyte showed specific discharge capacitance ~60 F/g at the end of 30th cycle at a current rate of 30 mA/g.

Then Zexuan Dong [17], focused on using the electrospinnig method to make materials fit for four major energy-related applications such as fuel cells,dye-sensitized solar cells, Li-ion batteries, and supercapacitors.

Jian-Gan [18], made a supercapacitor with high energy and power densities by using MnO_2/carbon nanofiber. He found that the energy density in the asymmetric supercapacitor is much higher than symmetric supercapacitor. The excellent result show promise for applications in asymmetric supercapacitors with high energy and power densities delivery.

CHAPTER II

EXPERIMENTAL DETAILS

2.1. Materials and Synthesis

The materials needed to synthesize the 1D nanofiber were 0.25 g of polyvinylpyrrolidone (PVP), 0.25 g of polyacrylonitrile (PAN), 5 mL of N,N-dimethylformamide (DMF), 0.5 mmol of $Co(CH_3COO)_2.4H_2O$ and 1 mmol of $Mn(CH_3COO)_2.4H_2O$.

Three steps were involved in the fabrication of 1D nanofibers: the first step was to prepare a homogeneous solution; the second step involved electrospinning of the homogenized solution; and the last step was to calcine the nanofibers generated in the second step to fabricate 1D nanofibers of metal oxide.

The homogeneous solution was obtained by disolving 0.25 g of polyvinylpyrrolidone (PVP) and 0.25 g of polyacrylonitrile (PAN) in 5 mL of N,N-dimethylformamide (DMF) solution followed by stirring for one hour using a magnetic stirrer. After one hour of stirring, 0.5 mmol of $Co(CH_3COO)_2$ and 1 mmol of $Mn(CH_3COO)_2$ were added and the solution was stirred at room temperature for an additional 24 hours. After complete mixing for 24 hours, the homogeneous solution was

loaded into a plastic syringe with a stainless steel needle. A high voltage power source was connected between the stainless steel needle and the collector plate. A high voltage of 18 kV was applied between the needle tip and aluminum foil which acted as a collector. The separa0tion between the needle tip and the collector plate was 16 cm with a spinning rate of 1 mL/h. After fabrication of nanowires, the nanowires were taken from the aluminum plate and calcinated at 600° C for eight hours under air. Three different heating rates were chosen to study the effect of heating rate on the morphology of the metal oxides. Three different heating rates such as 1, 3 and 5 ^{o}C/min were chosen (Figure 2.1). A similar procedure was adoped to fabricate other metal oxide nano-fibers ($NiMn_2O_4$ and $ZnMn_2O_4$). The details for the synthesis of other nano-fibers are given in Table 2.1.

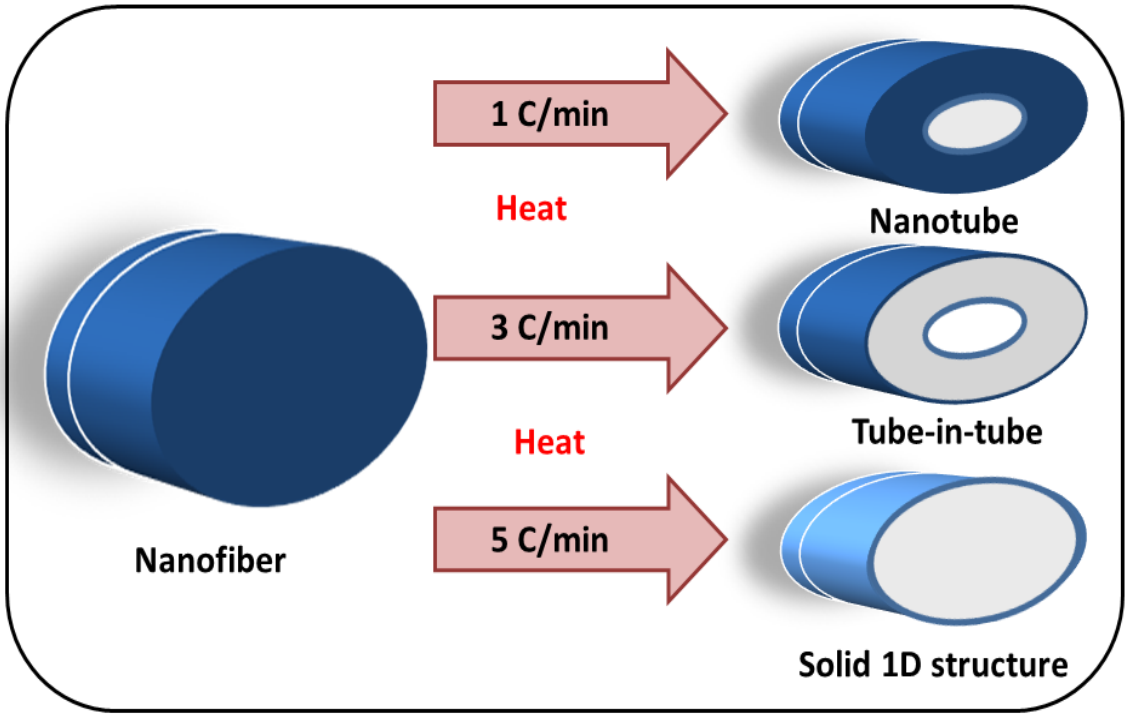

Figure 2.1: Effect of heating rate on the morphology of metal oxide.

Table 2.1: Experimental details for the synthesis of TMOs nanofibers.

Sample Code*	PVP (g)	PAN (g)	DMF (mL)	$Co(CH_3COO)_2$ Or $Ni(CH_3COO)_2$ Or $Zn(CH_3COO)_2$ (mmol)	$Mn(CH_3COO)_2$ (mmol)	Heating rate (^oC/min)
CMO-A	0.25	0.25	5	0.5	1	1
CMO-B	0.25	0.25	5	0.5	1	3
CMO-C	0.25	0.25	5	0.5	1	5
NMO-A	0.25	0.25	5	0.5	1	1
NMO-B	0.25	0.25	5	0.5	1	3
NMO-C	0.25	0.25	5	0.5	1	5
ZMO-A	0.25	0.25	5	0.5	1	1
ZMO-B	0.25	0.25	5	0.5	1	3
ZMO-C	0.25	0.25	5	0.5	1	5

*** CMO-$CoMn_2O_4$, NMO-$NiMn_2O_4$, ZMO-$ZnMn_2O_4$**

2.2. Materials Characterizations

The synthesized materials were characterized using several techniques such as scanning electron microscopy (SEM), energy dispersive X-ray spectroscope (EDX), X-ray diffraction (XRD)and electrochemical methods.

2.2.1. Scanning Electron Microscopy (SEM)

The morphologies and structure of the synthesized nanofibers were inspected by scanning electron microscopy (SEM). Electron microscopes are used extensively because they permit the observation and classification of the materials on a nanometer (nm) to micrometer (μm) scale range. The SEM has been a valued instrument in the improvement of scientific theories and has added greatly towards the progression of materials science and technology. The particle size and morphology of the powder samples were investigated using a JEOL JSM-840A scanning electron microscope equipped with an Oxford INCA 250 silicon drift X-ray energy dispersive spectrometer (EDX).

2.2.2. X-Ray Diffraction

The synthesized materials structures were examined using a Shimadzu X-ray diffractometer set on the 2θ-θ scan with $CuK_{\alpha 1}$ (λ=1.5406 Å) radiation. For the source and detector sides, 0.2 mm slits were used. The X-ray was generated using a voltage of 40 kV and a current of 30 mA. Using the detector, diffraction patterns in the form of X-ray counts were collected while the sample was rotated through 2θ = 25° - 70°. To satisfy the geometry, an X-ray detector was positioned so that the angle between the atomic planes and the detector was 2θ, as shown in Figure 2.2.

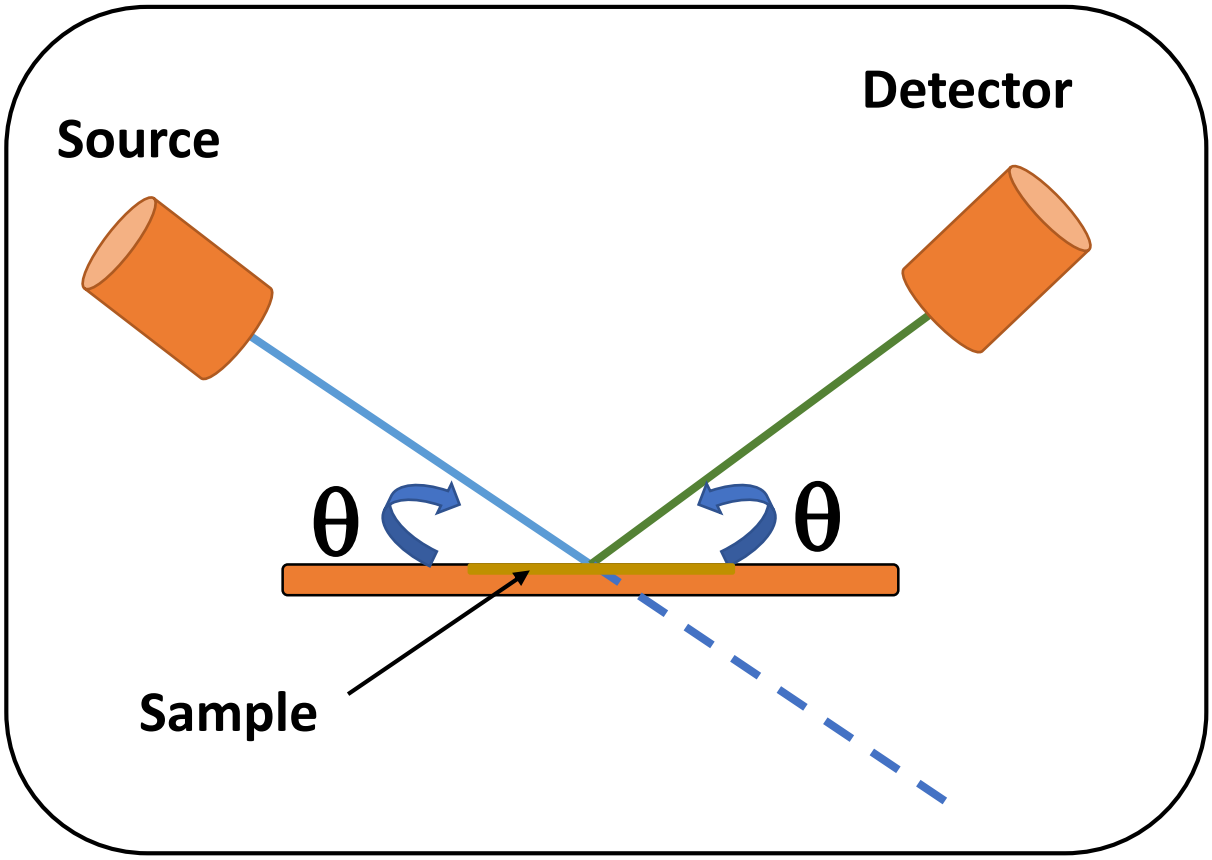

Figure 2.2: Schematic diagram of an X-ray diffractometer.

2.2.3. Electrochemical Measurements

The electrochemical measurements were performed in a typical three electrode cell system. A platinum wire as a counter electrode, a saturated calomel electrode as a reference electrode, and as-synthesized nanofibers ($CoMn_2O_4$, $NiMn_2O_4$ and $ZnMn_2O_4$) on nickel foam as a working electrode were used. The schematic diagram of the three electrode system is shown in Figure 2.4. Before making the working electrode, the nickel foam was cleaned using 3M HCl followed by cleaning using water and acetone with the help of a bath sonicator. The working electrode was prepared by applying a paste the consisted of 80 wt.% of the nanofiber sample, 10 wt.% of acetylene black and 10 wt.% of polyvinylidenedifluoride (PVDF). N-methyl pyrrolidinone (NMP) was used as a solvent for paste preparation. The paste was applied on the pre-cleaned and weighted nickel foam and dried under vacuum at 60 °C for 10 hours. Different electrolytes such as 3 M KOH, NaOH and LiOH were used for electrochemical testing.

The electrochemical testing were performed using a Versastat 4-500 electrochemical workstation (Princeton Applied Research, USA). Cyclic voltammetry (CV) and galvanostatic charge-discharge measurements were performed to study the electrochemical behavior of these metal oxides. In addition to electrochemical investigation on single electrode, a symmetric supercapacitor was fabricated and tested. The supercapacitor device was fabricated by sandwiching an ion transporting layer (Celgard, 25□m thick, 39% porosity) between two electrodes made using nanofibers of metal oxide. All the studies were performed in 3M NaOH. Cyclic voltammetry and galvanostatic charge-discharge measurements were used to evaluate the charge storage

capacity of the device. The effect of temperature on the electrochemical properties of the device was studied for its application in severe conditions.

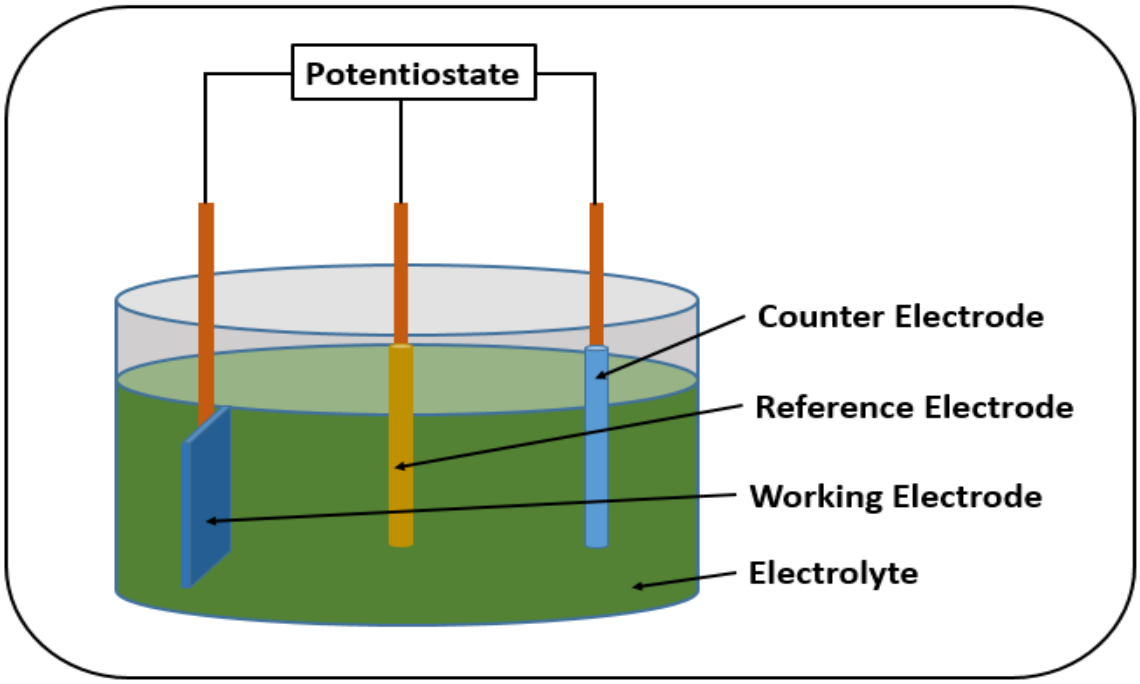

Figure 2.3: Schematic of three cell electrochemical measurement system.

CHAPTER III

RESULTS AND DISCUSSION

3.1. Scanning Electron Microscopic Analysis

Three different types of transition metal oxides (TMOs) such as $CoMn_2O_4$, $NiMn_2O_4$, and $ZnMn_2O_4$ were fabricated. The morphology and structure of the fabricated metal oxides were studied using scanning electron microscope (SEM). The SEM images of CMO, NMO and ZMO at different magnifications are shown in Figures 3.1-3.9. It was observed that morphologies of these metal oxides depend on the heating rate.

Energy-dispersive X-ray spectrometry (EDX) was performed to investigate the elements and their composition in the metal oxides. The EDX pattern demonstrates the presence of Co and Mn in CMO sample with their elemental ratio close to $CoMn_2O_4$. The EDX pattern of some of the samples are shown in Figure 3.10 and 3.11.

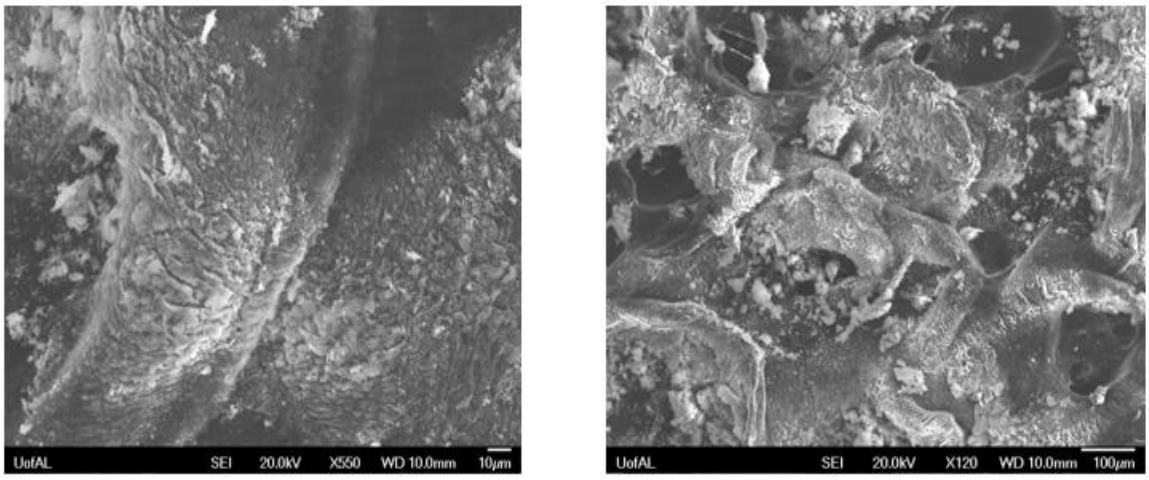

Figure 3.1: SEM images of CMO-A at various magnifications.

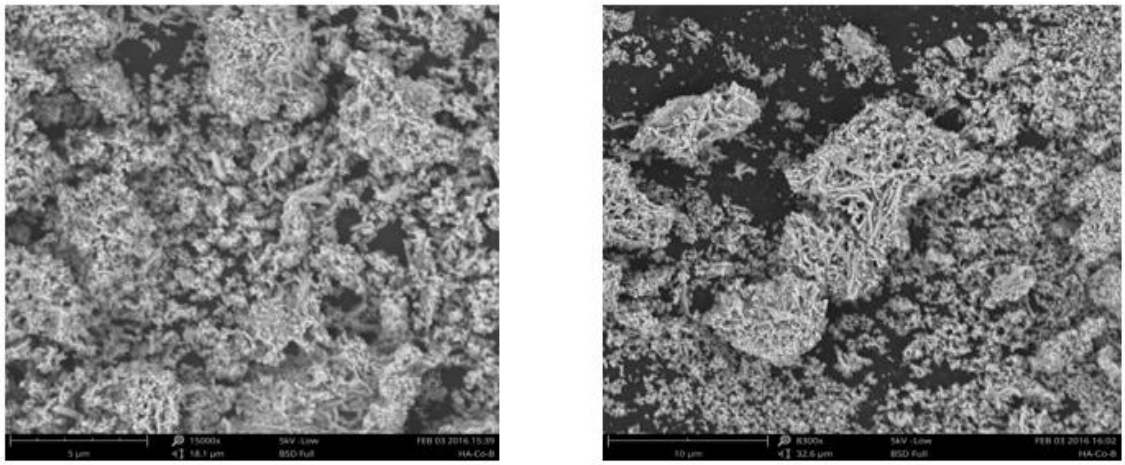

Figure 3.2: SEM images of CMO-B at various magnifications.

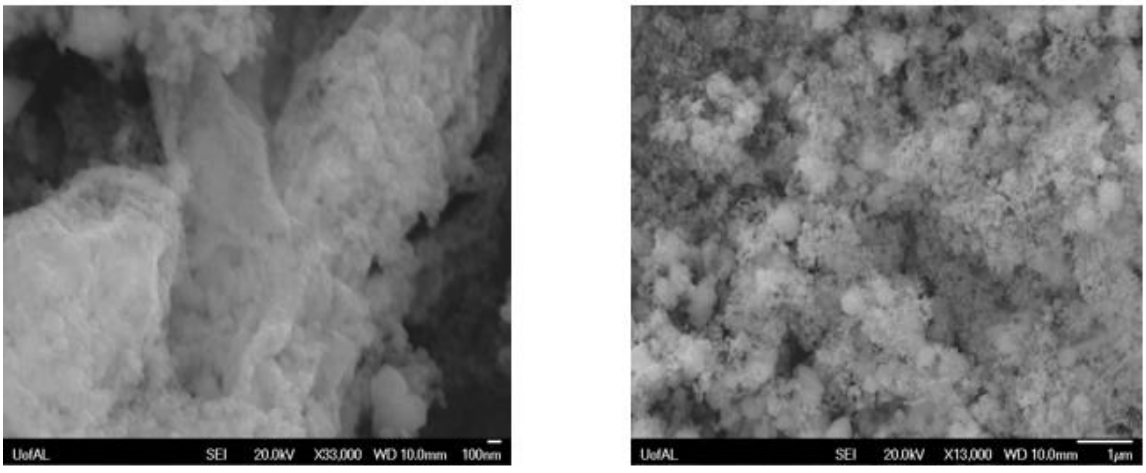

Figure 3.3: SEM images of CMO-C at various magnifications.

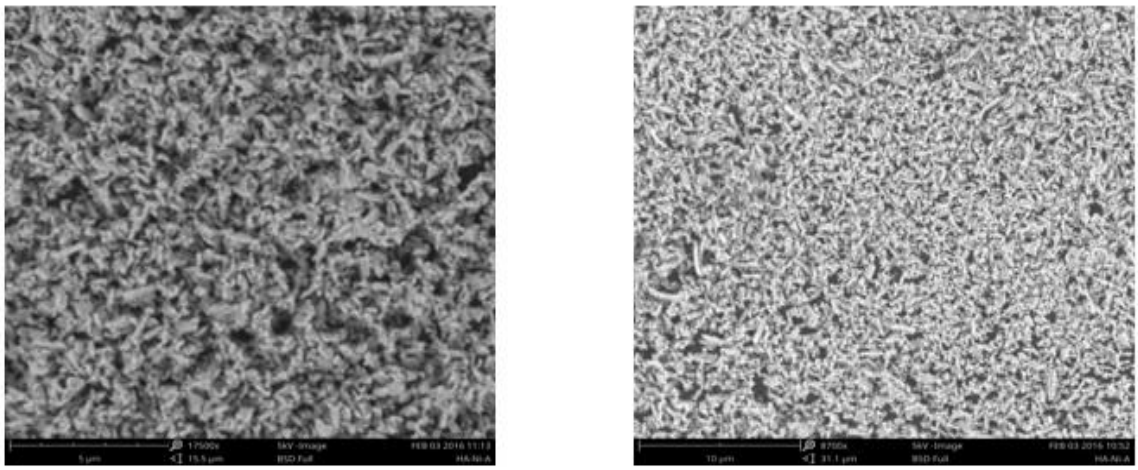

Figure 3.4: SEM images of NMO-A at various magnifications.

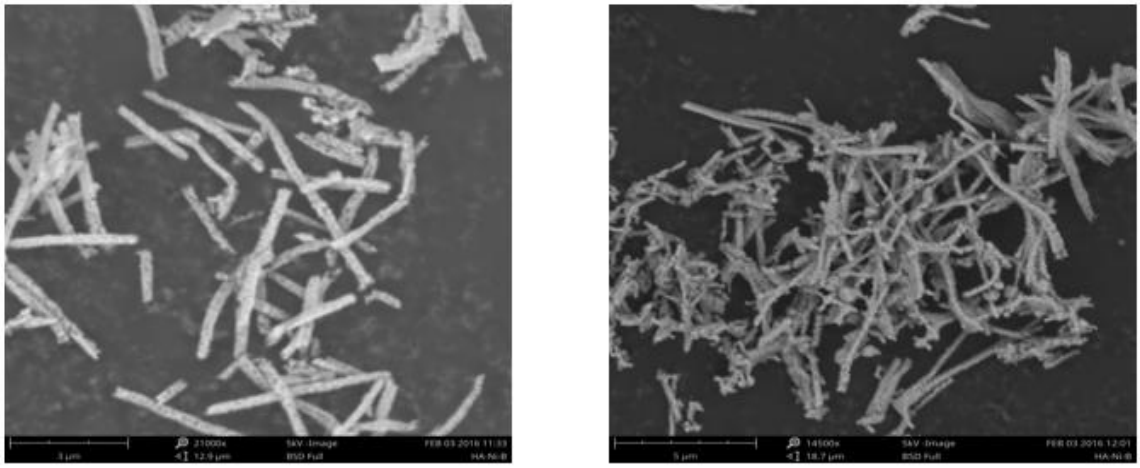

Figure 3.5: SEM images of NMO-B at various magnifications.

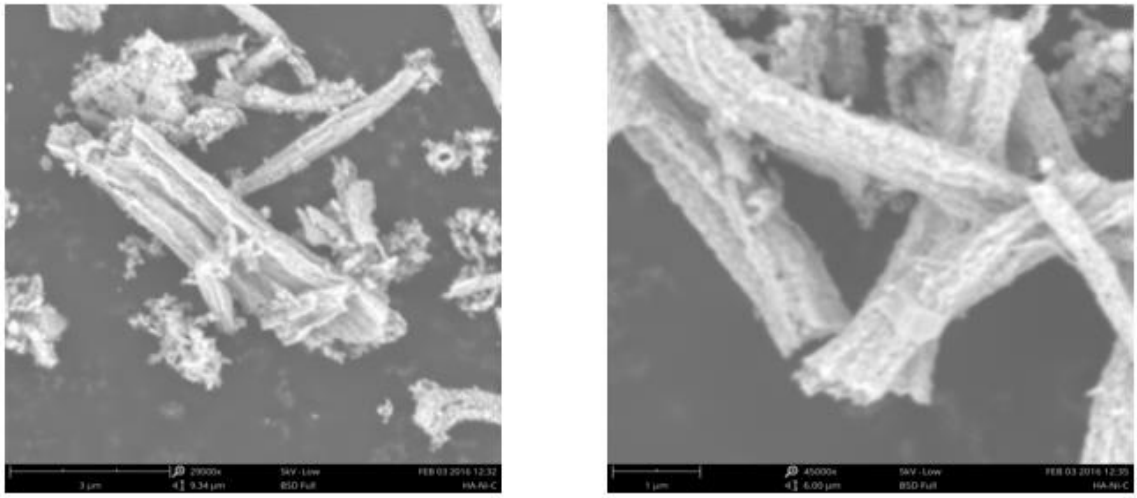

Figure 3.6: SEM images of NMO-C at various magnifications.

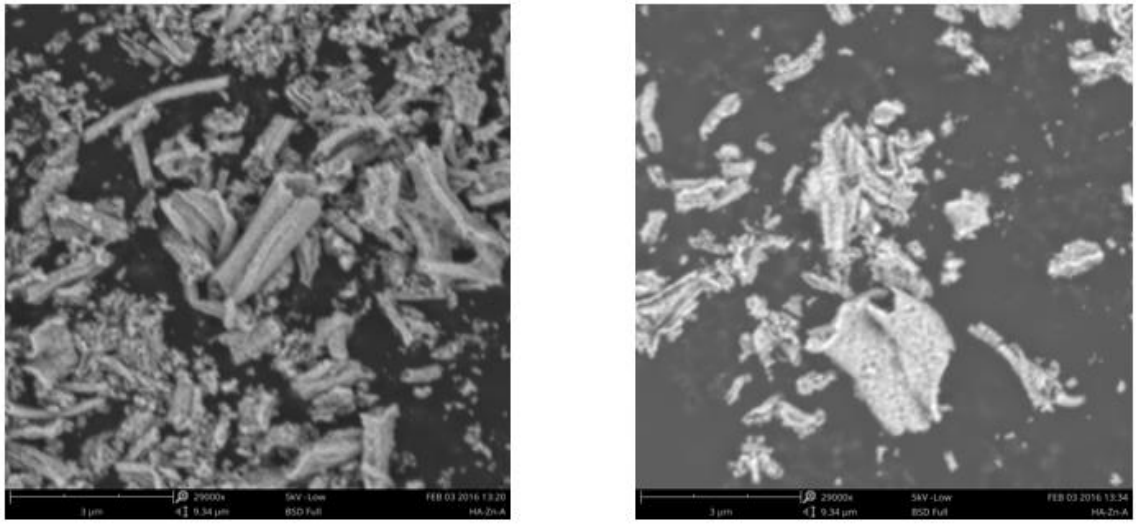

Figure 3.7: SEM images of ZMO-A at various magnifications.

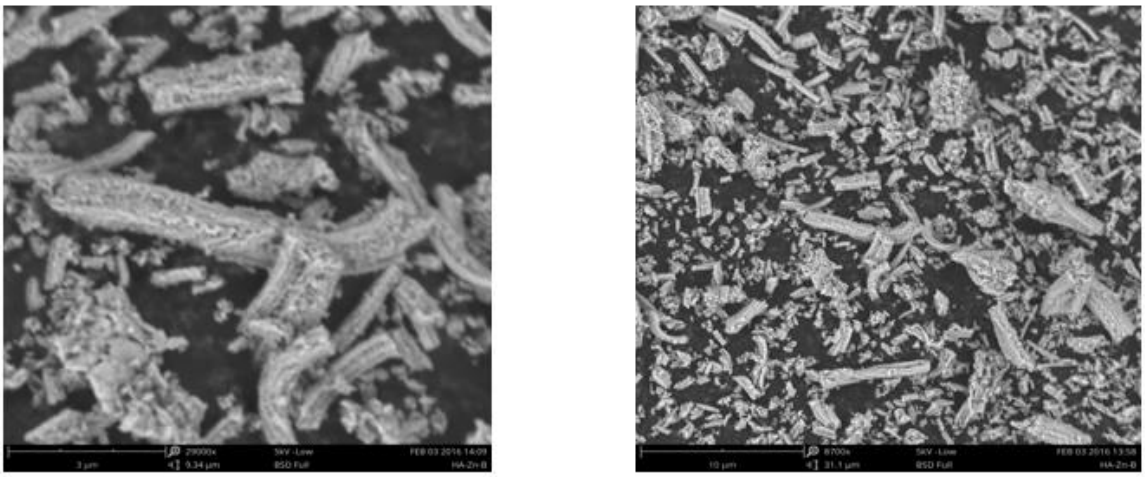

Figure 3.8: SEM images of ZMO-B at various magnifications.

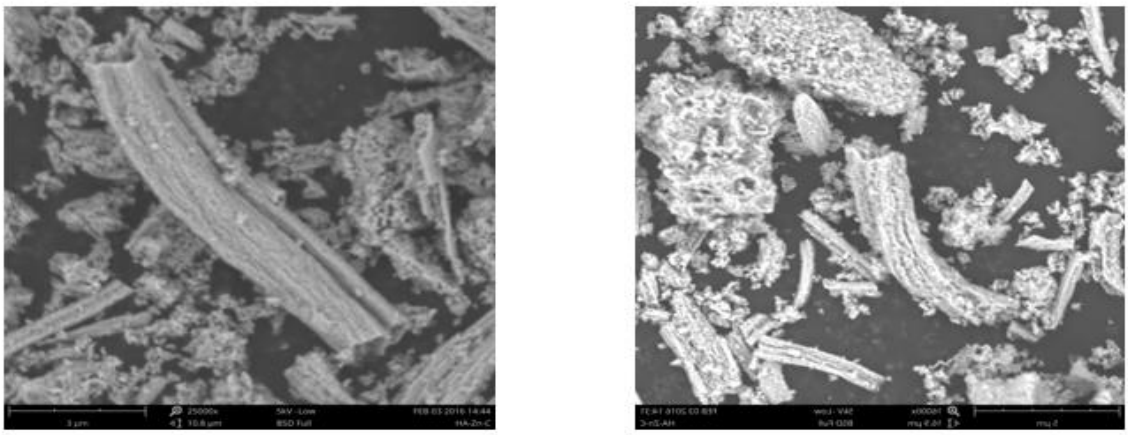

Figure 3.9: SEM images of ZMO-C at various magnifications.

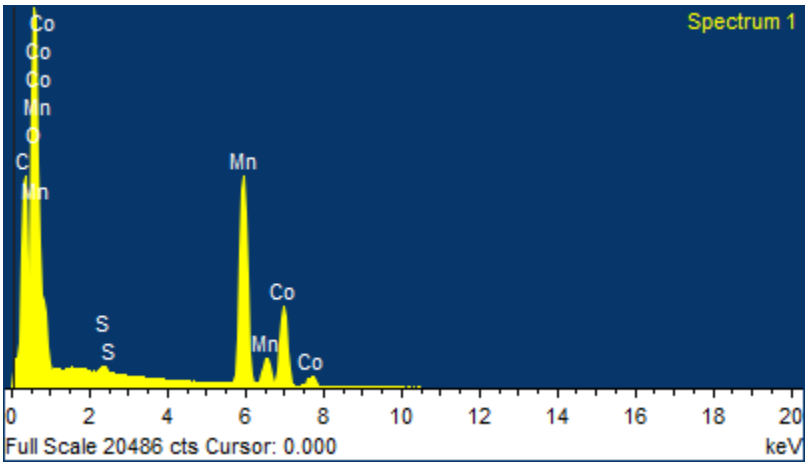

Figure 3.10: EDX images of CMO-A (Y-axis is count).

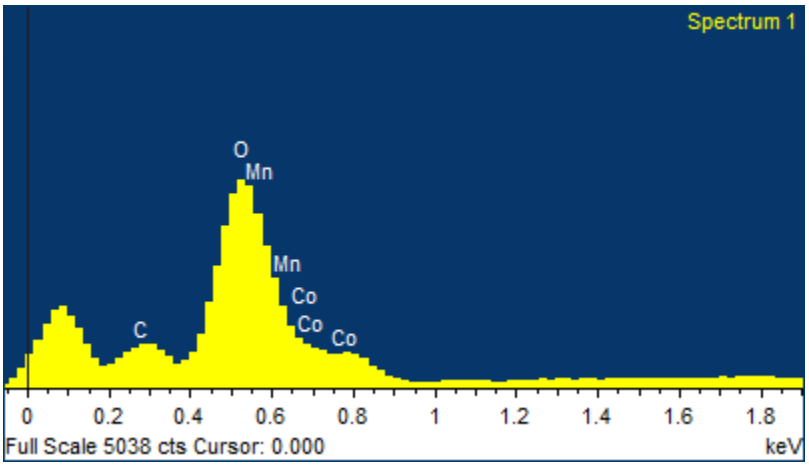

Figure 3.11: EDX images of CMO-C (Y-axis is count).

3.2. X-Ray Diffraction Analysis

The XRD patterns of all samples prepared using different heating rates and thus having various morphologies were recorded and studied. The diffraction patterns of the samples recorded in range of 25-70 degree are shown in Figures 3.12-3.14. Powder X-ray diffraction (XRD) confirmed that all of the synthesized powders such as $CoMn_2O_4$, $NiMn_2O_4$, and $ZnMn_2O_4$ are phase pure. The XRD patterns was readily assigned to crystalline phase of $CoMn_2O_4$ (JCPDS card no. 77-0471) without any other detectable phase, indicating the phase purity of the prepared samples.

The XRD data of the samples was used to evaluate the crystallite size of the synthesized $CoMn_2O_4$, $NiMn_2O_4$, and $ZnMn_2O_4$ nanofibers. The average crystallite size (t) of all the samples was calculated using the Debye Scherrer equation [19]:

$$t = \frac{0.9\,\lambda}{\beta\,cos\theta} \quad \text{.....(2)}$$

where λ is the X-ray wavelength, β is the full width at half maximum of the diffraction line, and θ is the diffraction angle of the XRD spectra. The average crystallite size of all the samples is given in Table 3.1.

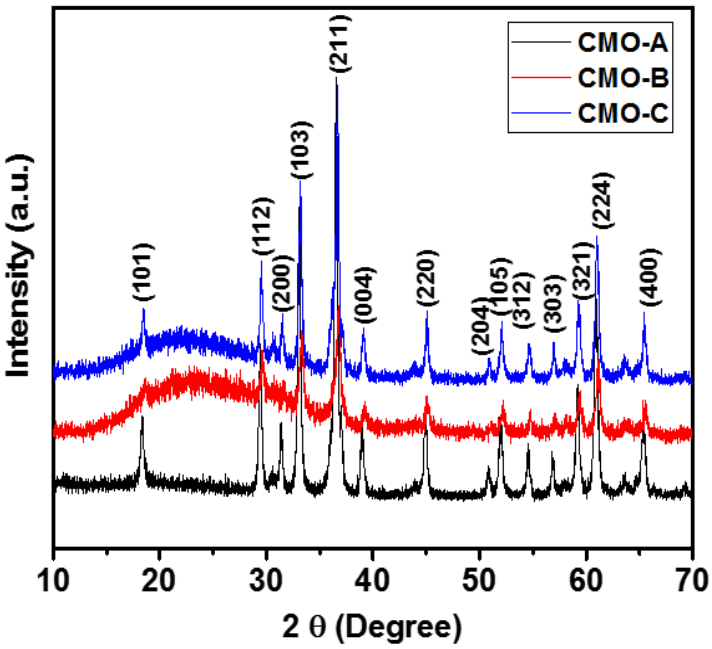

Figure3.12: XRD patterns of $CoMn_2O_4$ nanofibers.

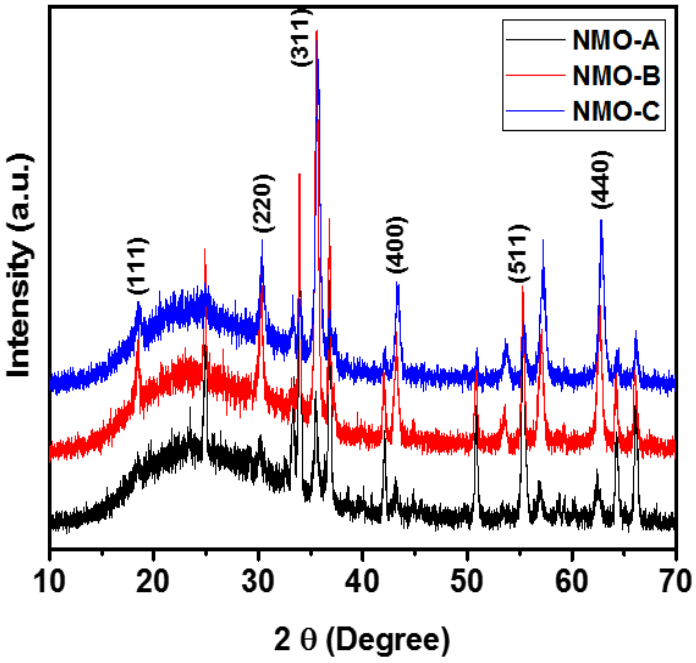

Figure3.13: XRD patterns of $NiMn_2O_4$ nanofibers.

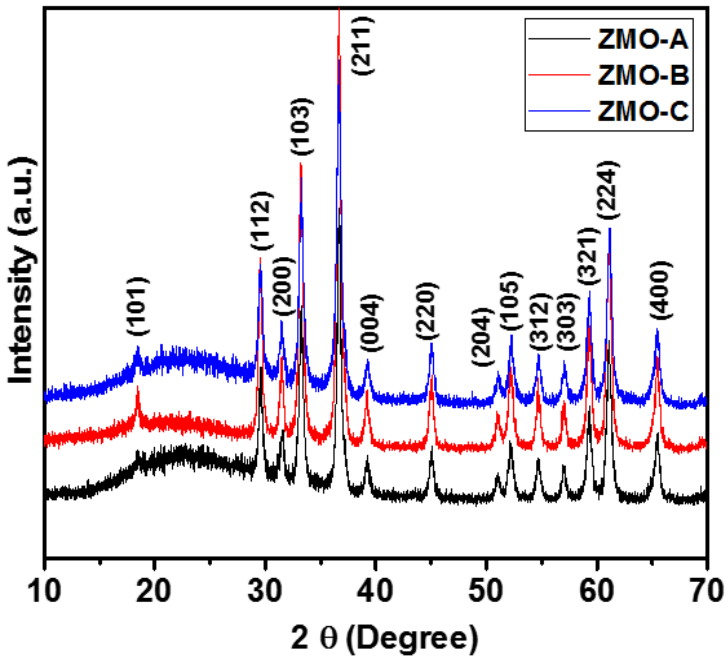

Figure3.14: XRD patterns of $ZnMn_2O_4$ nanofibers.

Table 3.1: Crystalline size of the synthesized $CoMn_2O_4$, $NiMn_2O_4$, and $ZnMn_2O_4$ nanofibers

Sample	FWHM (Degree)	Crystallite Size (nm)
CMO-A	0.0061	26.85
CMO-B	0.0080	21.42
CMO-C	0.0049	32.81
NMO-A	0.0045	35.65
NMO-B	0.0068	24.47
NMO-C	0.0092	19.31
ZMO-A	0.0075	22.59
ZMO-B	0.0082	21.07
ZMO-C	0.0084	20.73

3.3. Electrochemical Characterizations

3.3.1. For The Single Electrode:

Cyclic voltammetry and galvanostatic charge-discharge measurements were carried to study the electrochemical properties of the synthesized nanofibers of metal oxides. The effect of different electrolytes such as LiOH, NaOH and KOH on the electrochemical properties of the metal oxide nanofibers was also investigated in details. Cyclic voltammograms of CMO-A sample in different electrolytes at various scan rates are shown in Figures 3.15-3.17. As seen in the figures, the cyclic voltammograms of CMO showed the presence of redox peaks, indicating that redox process is the predominating mechanism for energy storage in this system. It's worth noting that for the EDLCs the shape of CV curves should be rectangular in nature. The shape and nature of the cyclic voltammograms of the synthesized samples suggest that the capacitance is mainly due to pseudocapacitance. The cyclic voltammograms of the CMO, NMO and ZMO show a pair of redox peaks in oxidation and reduction process. The mechanism for such a redox process in $CoMn_2O_4$ based electrode in alkaline aqueous electrolytes could be explained by the following reaction:

$$MnO_2 + M^+ + e^- \leftrightarrow MnOOM \qquad (\mathrm{M} = \mathrm{H}^+, \mathrm{Li}^+, \mathrm{Na}^+ \text{ or } \mathrm{K}^+)$$

Data from the cyclic voltammetric measurements was used to calculate the specific capacitance of the as-prepared electrode. The specific capacitance (C_{sp}) of the CMO,NMO and ZMO electrodes was calculated using the following expression [20].

$$C_{sp} = \frac{Q}{\Delta V \times (\frac{\partial v}{\partial t}) \times m} \quad \text{.....(3)}$$

where *Q* is the area under the CV curve, $\partial v/\partial t$ is the scan rate, ΔV is the potential window and *m* is the mass of the sample used in the electrode. The variation of specific capacitance as a function of scan rate in different electrolytes is shown in Figure 3.42. With increasing scan rate the specific capacitance was decreasing in all the studied electrolytes.The reason for that could be due to lack of time for the redox reaction at electrode. On the other hand, the concentration of the ions at the electrode/electrolyte interface, at a higher scan rate, increases quickly and the diffusion rate of electrolyte from electrode/electrolyte interface to electrode will be not enough to give good electrochemical reactions [21]. The specific capacitance basically depends on scan rate and the type of electrolyte used. As seen in the CV curves of these samples, the shape of the curves is very similar even at higher scan rates, indicating high electrochemical stability of the electrodes. In addition to this, it was observed that the peak position shifted towards higher potential during the oxidation process with increase in the scan rates. This suggests that charge transport in these materials are diffusion controlled.

The cyclic voltammograms and variation of specific capacitance as a function of scan rate for the other samples (CMO-B to ZMO-B) are shown in Figure 3.39 through Figure 3.70. As seen in the CV curves, these materials also exhibited pseudocapacitive

behavior. The maximum specific capacitance of 120 F/g was calculated for CMO-B sample in 3M NaOH electrolyte.

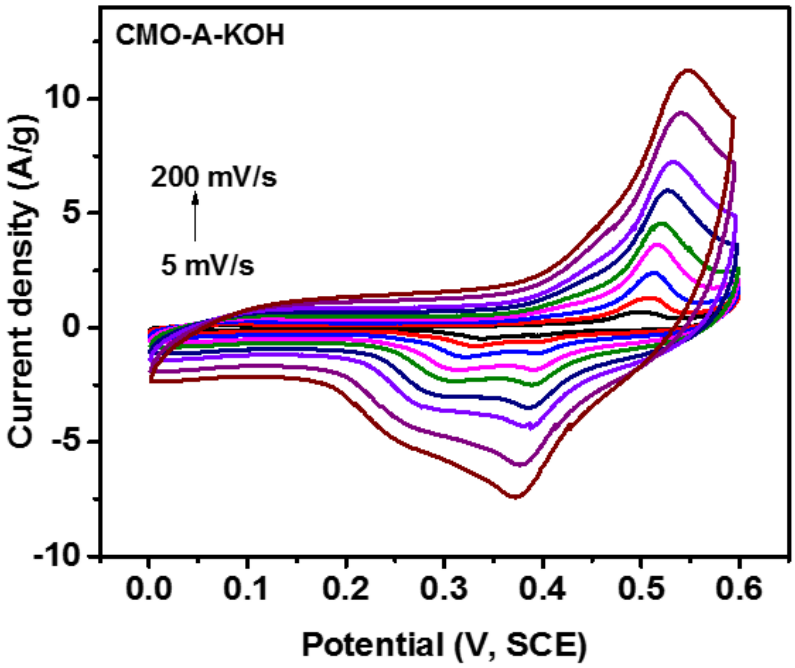

Figure 3.15: Cyclic voltammograms of CMO-A sample at various scan rates in 3 M KOH electrolyte.

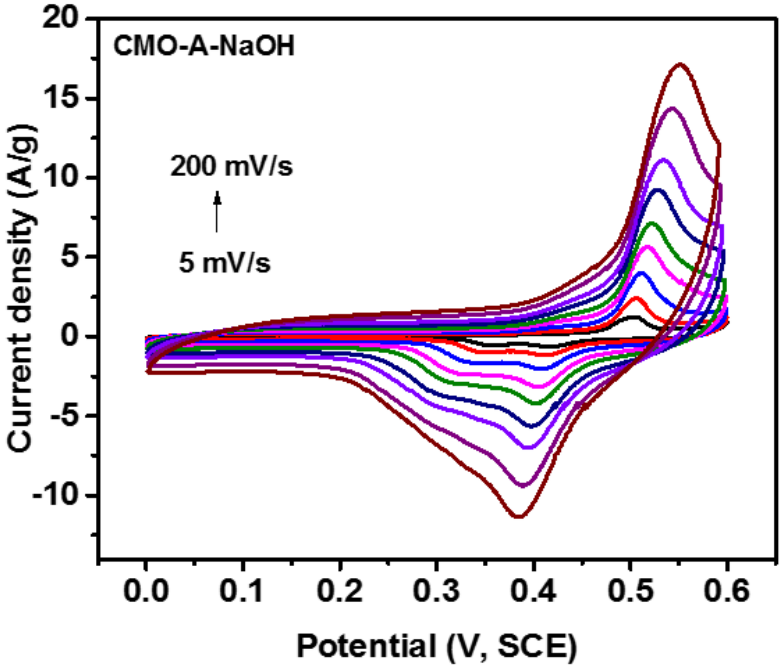

Figure 3.16: Cyclic voltammograms of CMO-A sample at various scan rates in 3 M NaOH electrolyte.

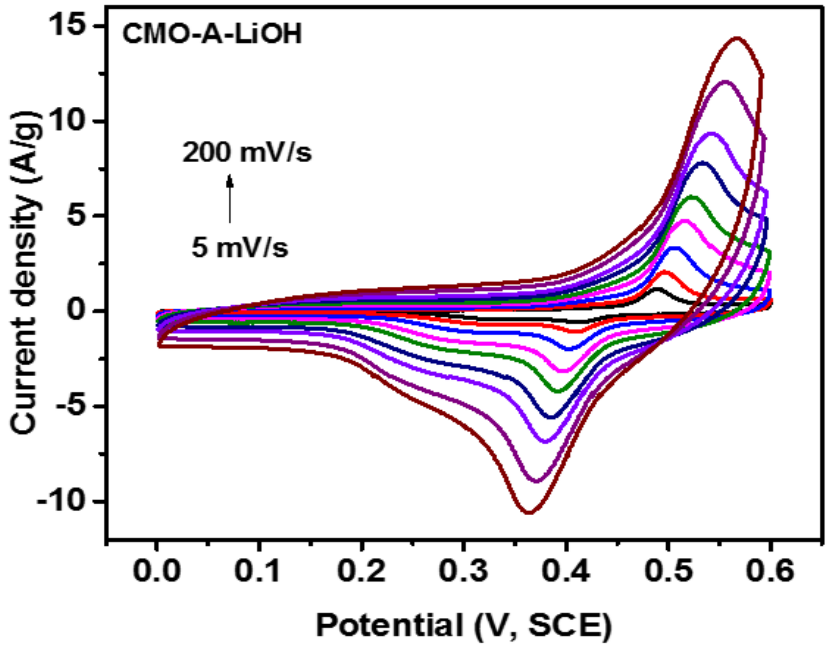

Figure 3.17: Cyclic voltammograms of CMO-A sample at various scan rates in 3 M LiOH electrolyte.

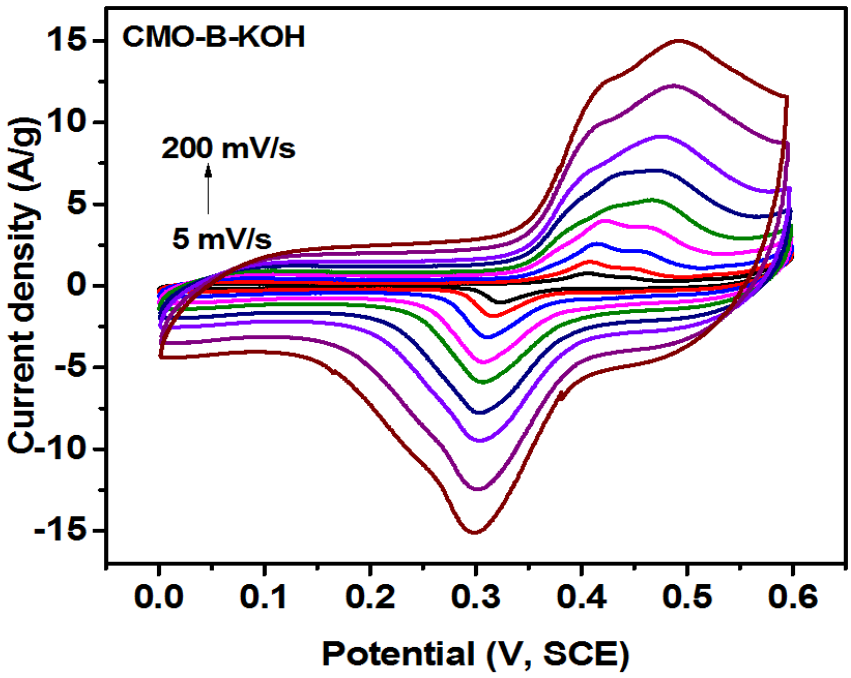

Figure 3.18: Cyclic voltammograms of CMO-B sample at various scan rates in 3 M KOH electrolyte.

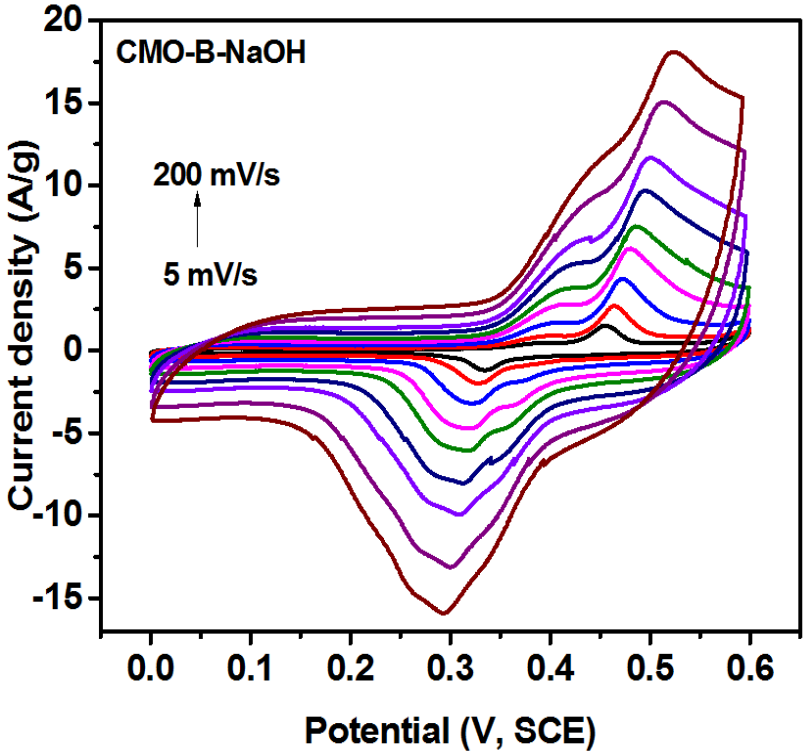

Figure 3.19: Cyclic voltammograms of CMO-B sample at various scan rates in 3 M NaOH electrolyte.

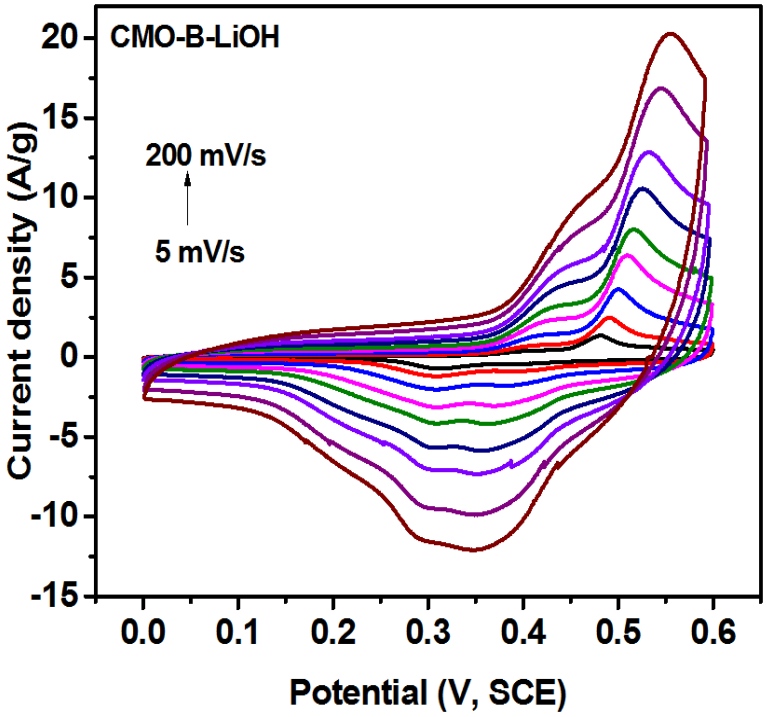

Figure 3.20: Cyclic voltammograms of CMO-B sample at various scan rates in 3 M LiOH electrolyte.

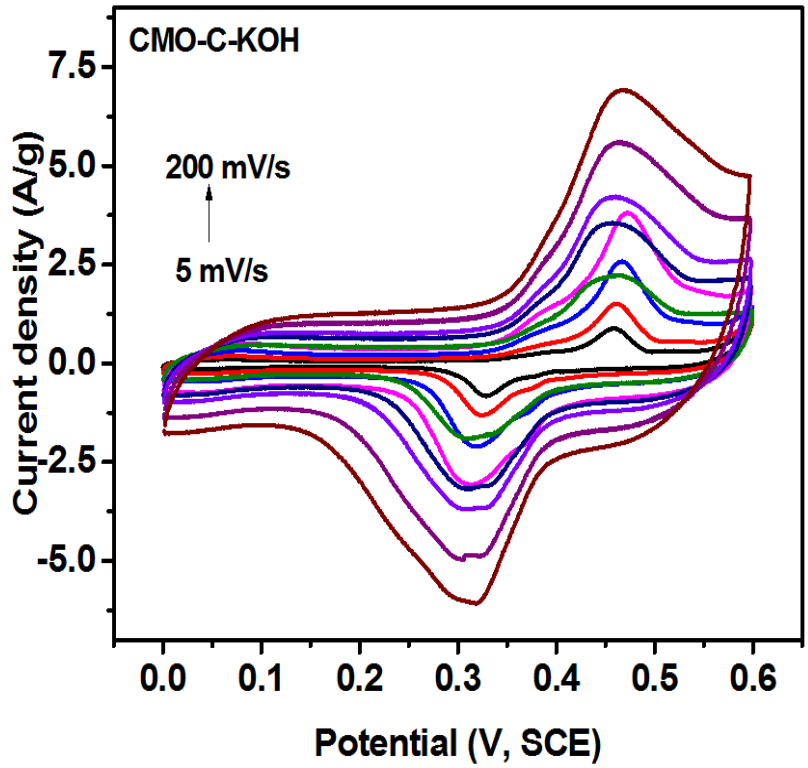

Figure 3.21: Cyclic voltammograms of CMO-C sample at various scan rates in 3 M KOH electrolyte.

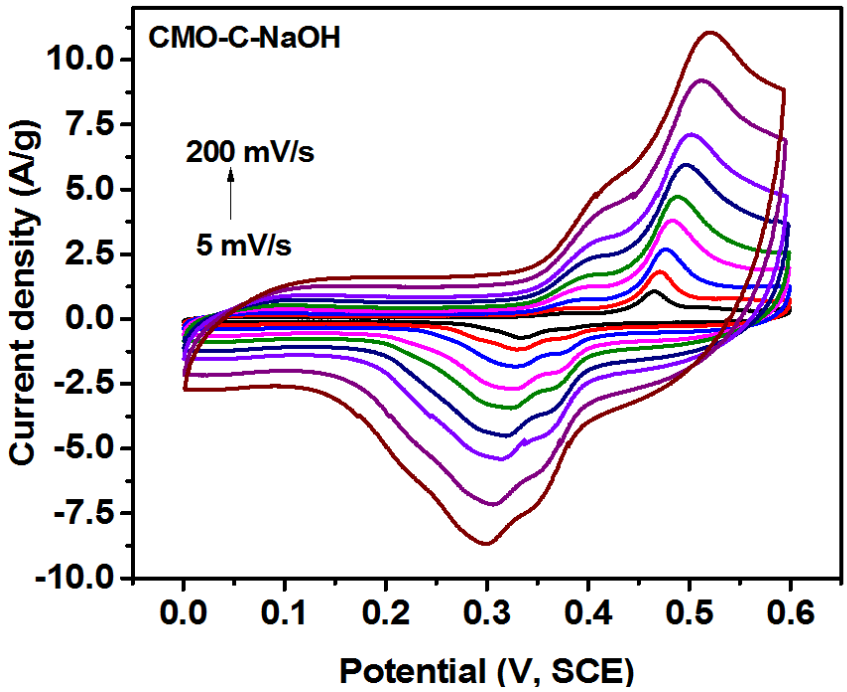

Figure 3.22: Cyclic voltammograms of CMO-C sample at various scan rates in 3 M NaOH electrolyte.

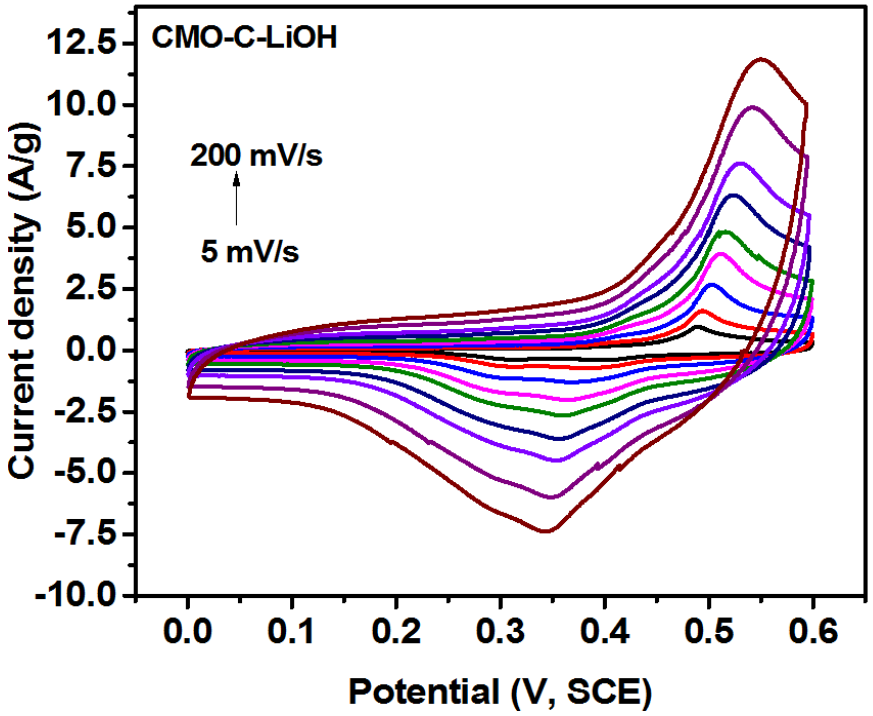

Figure 3.23: Cyclic voltammograms of CMO-C sample at various scan rates in 3 M LiOH electrolyte.

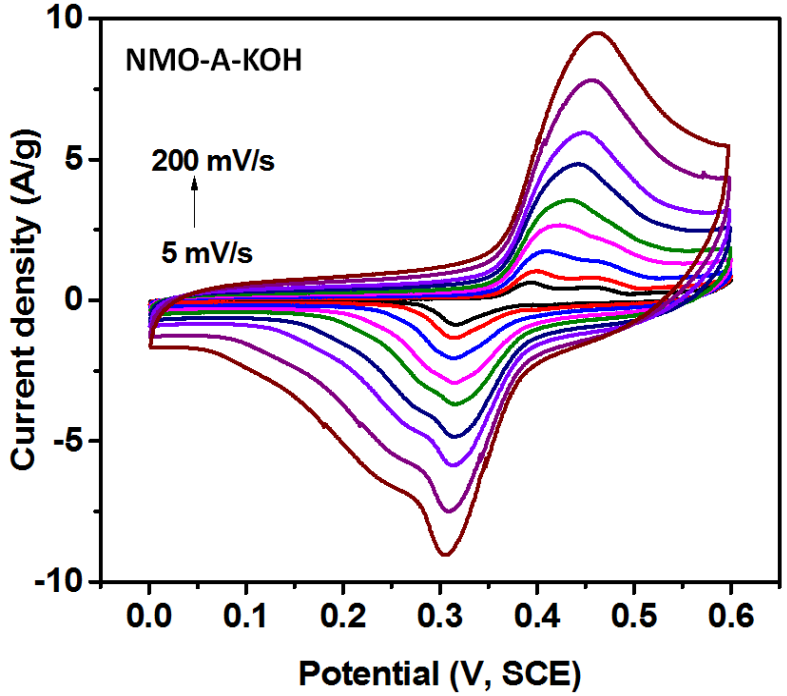

Figure 3.24: Cyclic voltammograms of NMO-A sample at various scan rates in 3 M KOH electrolyte.

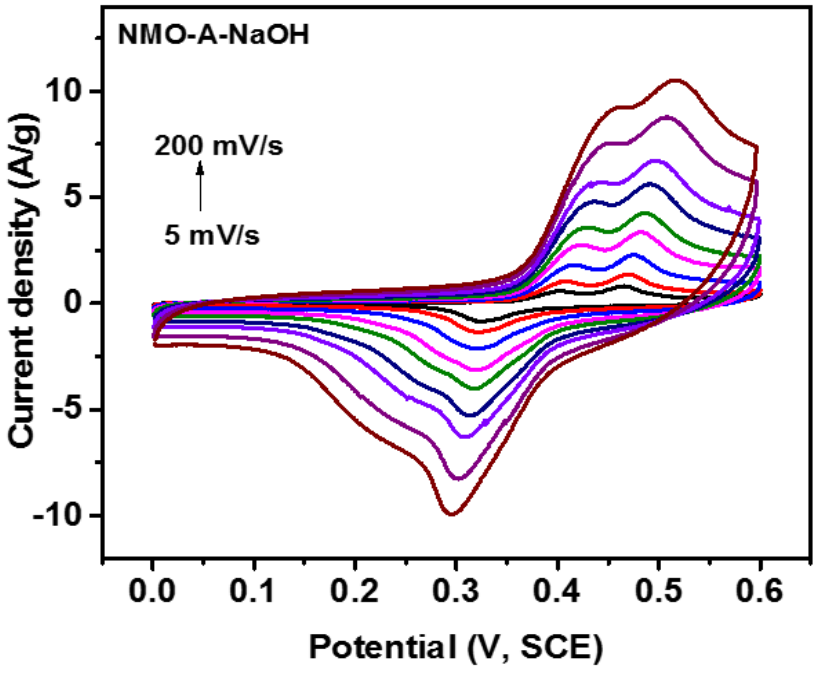

Figure 3.25: Cyclic voltammograms of NMO-A sample at various scan rates in 3 M NaOH electrolyte.

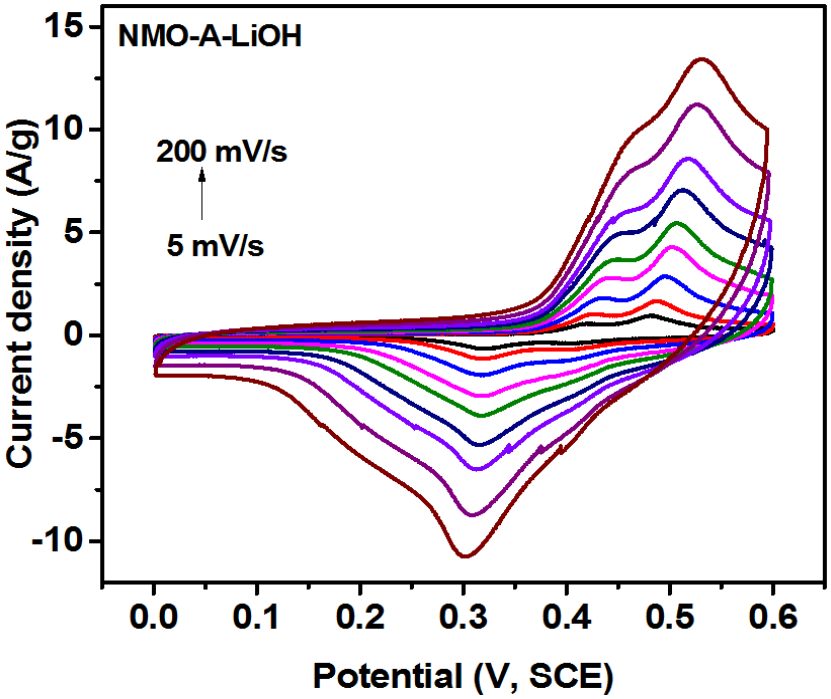

Figure 3.26: Cyclic voltammograms of NMO-A sample at various scan rates in 3 M LiOH electrolyte.

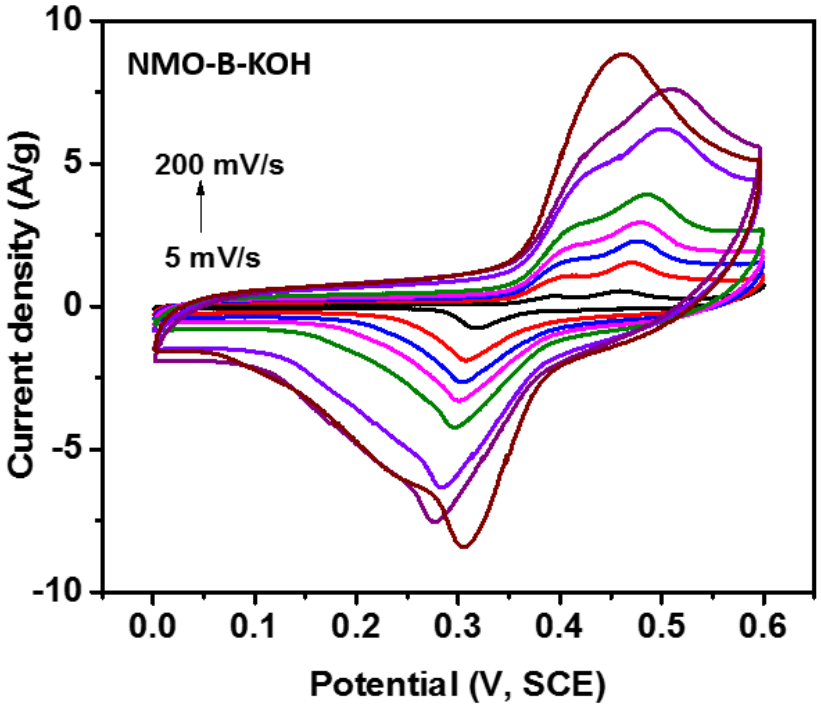

Figure 3.27: Cyclic voltammograms of NMO-B sample at various scan rates in 3 M KOH electrolyte.

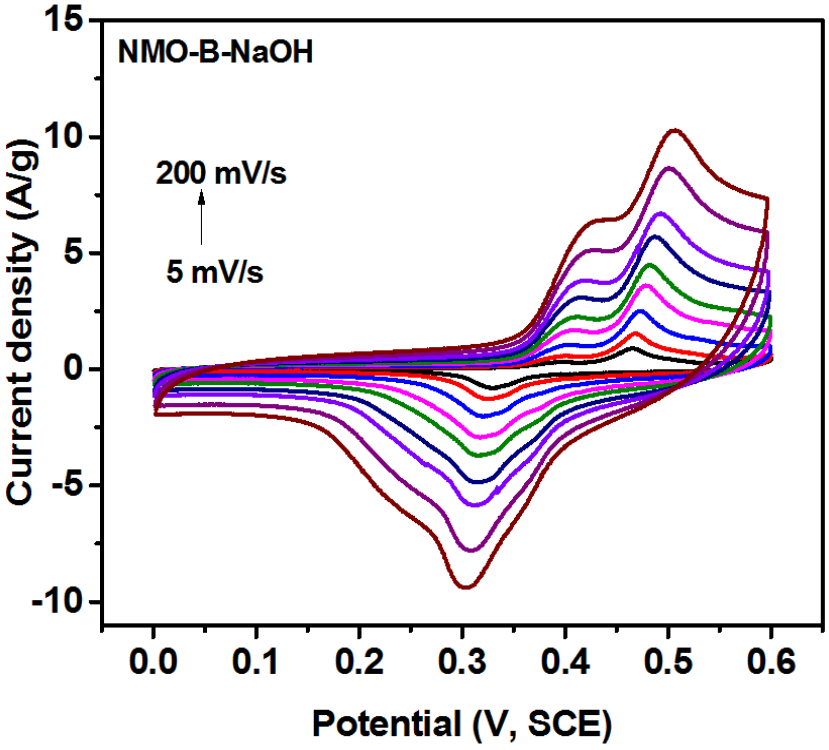

Figure 3.28: Cyclic voltammograms of NMO-B sample at various scan rates in 3 M NaOH electrolyte.

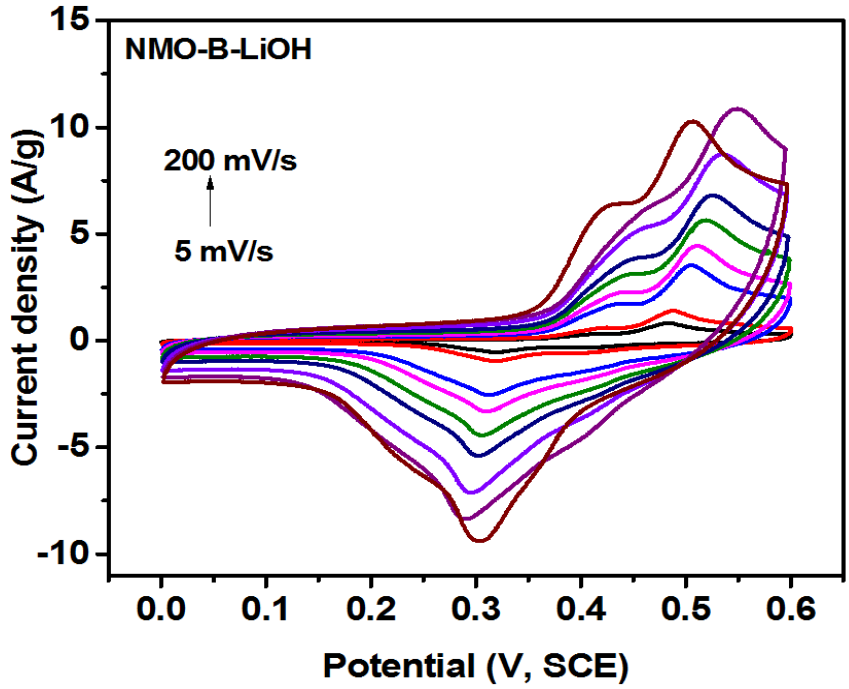

Figure 3.29: Cyclic voltammograms of NMO-B sample at various scan rates in 3 M LiOH electrolyte.

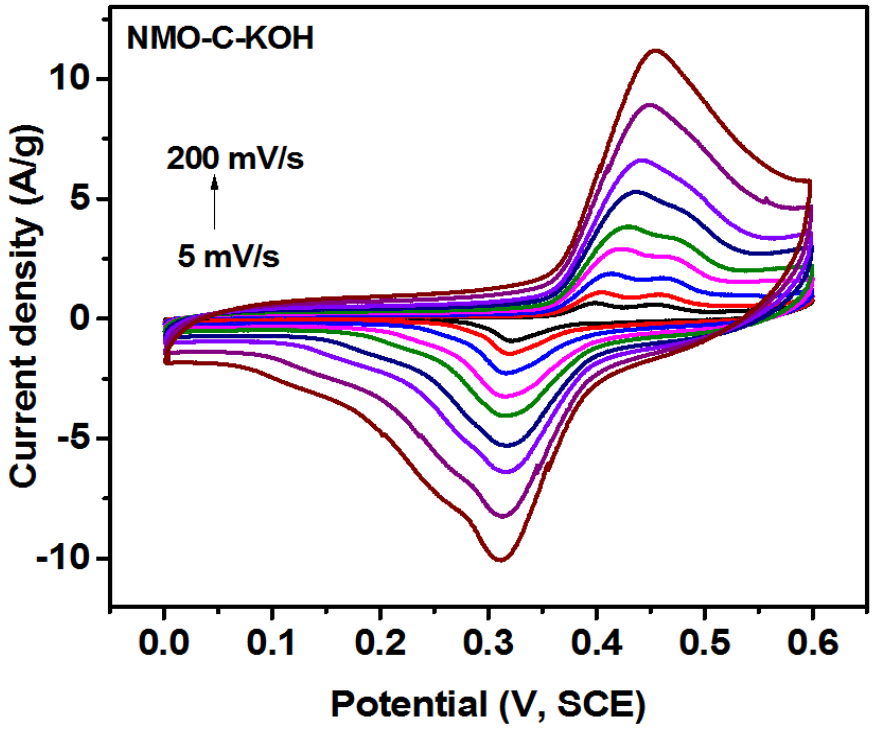

Figure 3.30: Cyclic voltammograms of NMO-C sample at various scan rates in 3 M KOH electrolyte.

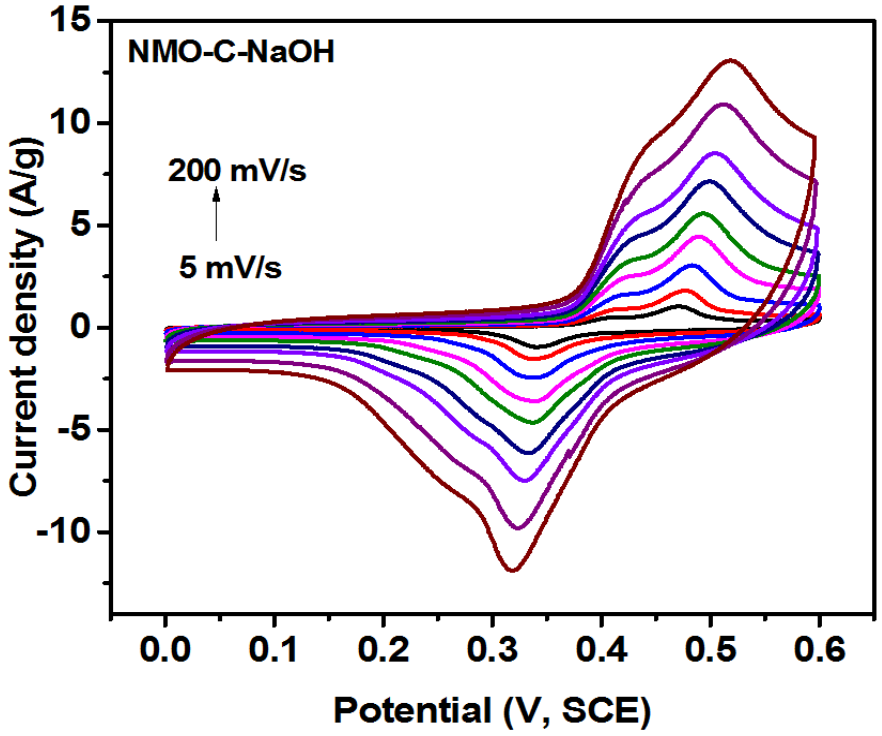

Figure 3.31: Cyclic voltammograms of NMO-C sample at various scan rates in 3 M NaOH electrolyte.

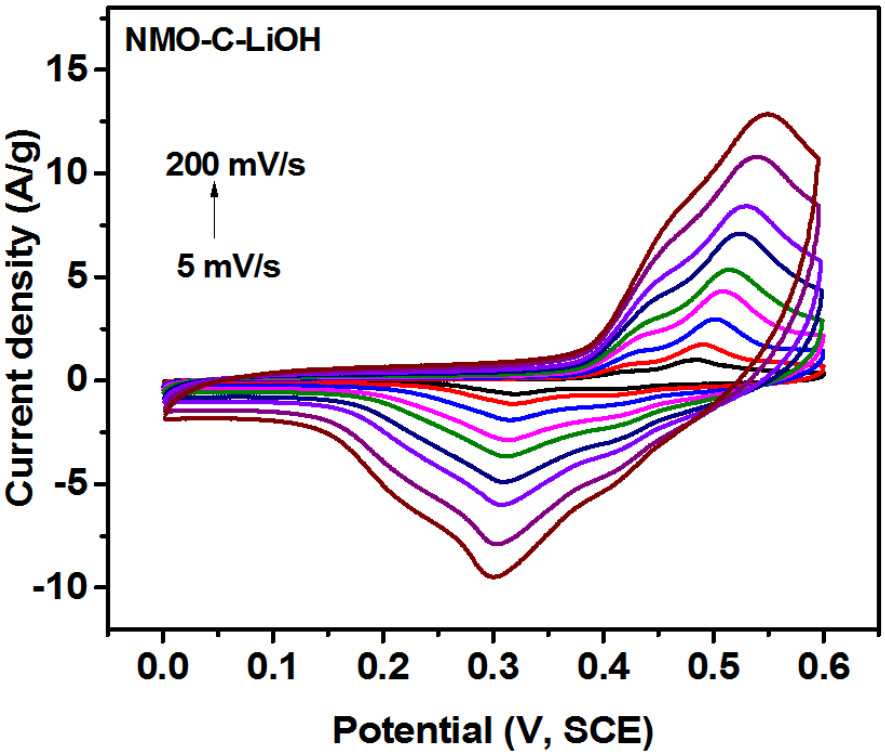

Figure 3.32: Cyclic voltammograms of NMO-C sample at various scan rates in 3 M LiOH electrolyte.

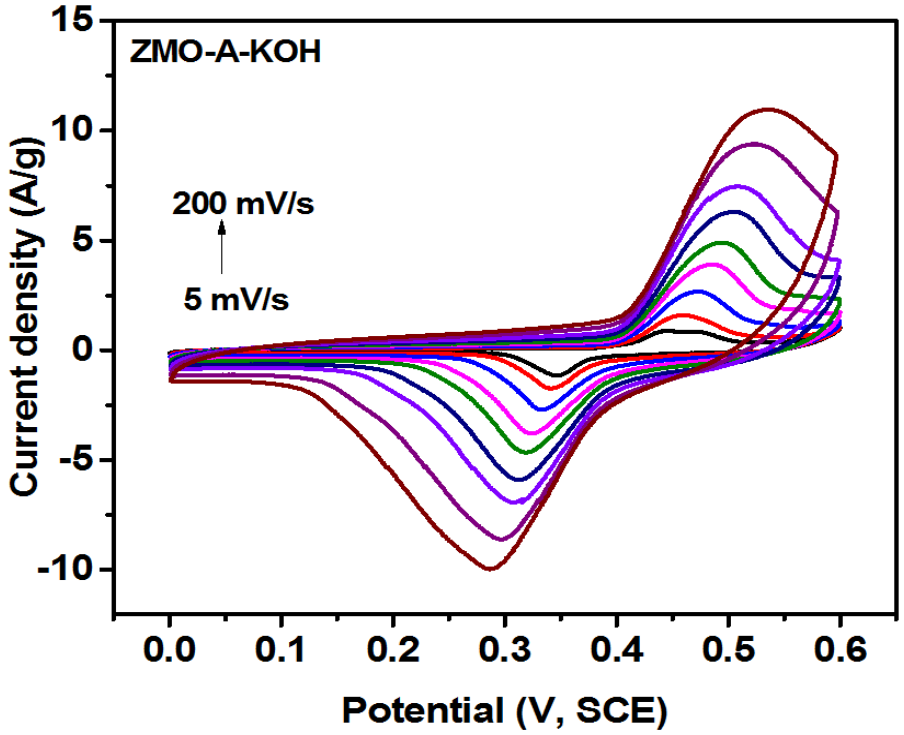

Figure 3.33: Cyclic voltammograms of ZMO-A sample at various scan rates in 3 M KOH electrolyte.

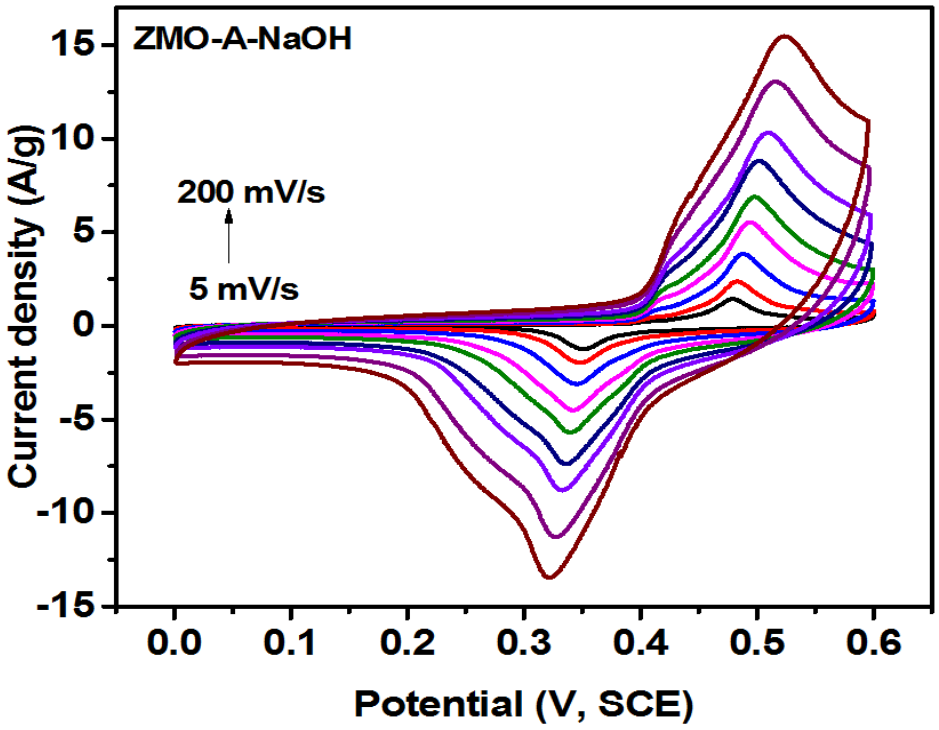

Figure 3.34: Cyclic voltammograms of ZMO-A sample at various scan rates in 3 M NaOH electrolyte.

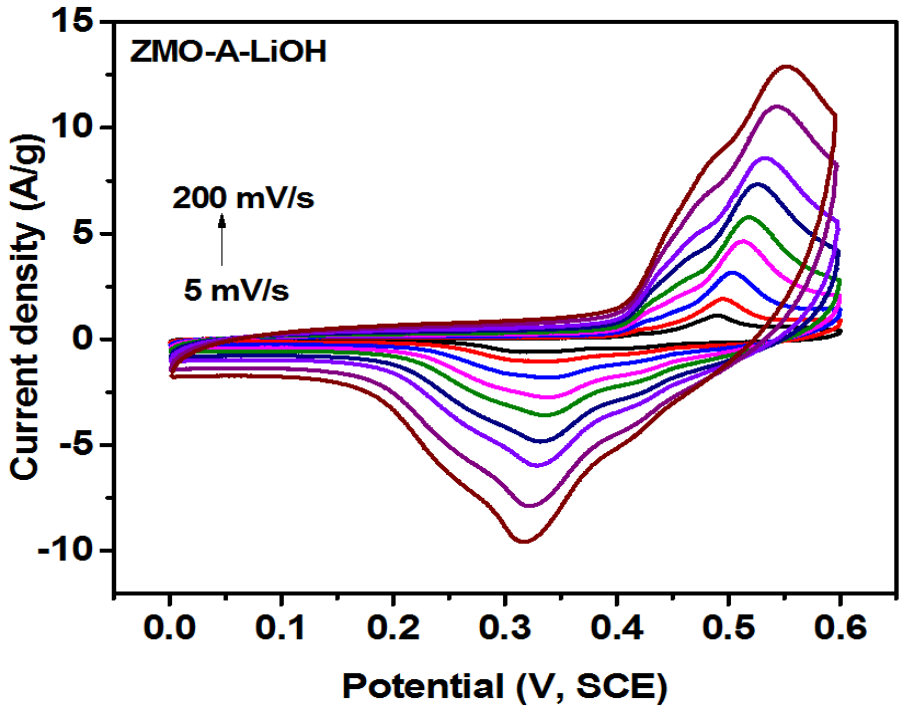

Figure 3.35: Cyclic voltammograms of ZMO-A sample at various scan rates in 3 M LiOH electrolyte.

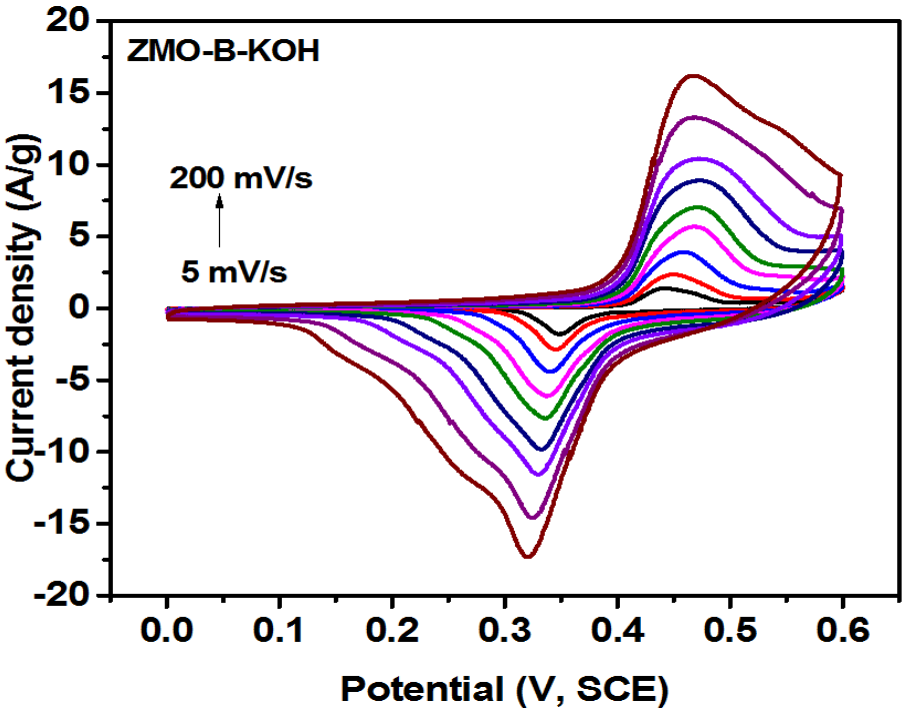

Figure 3.36: Cyclic voltammograms of ZMO-B sample at various scan rates in 3 M KOH electrolyte.

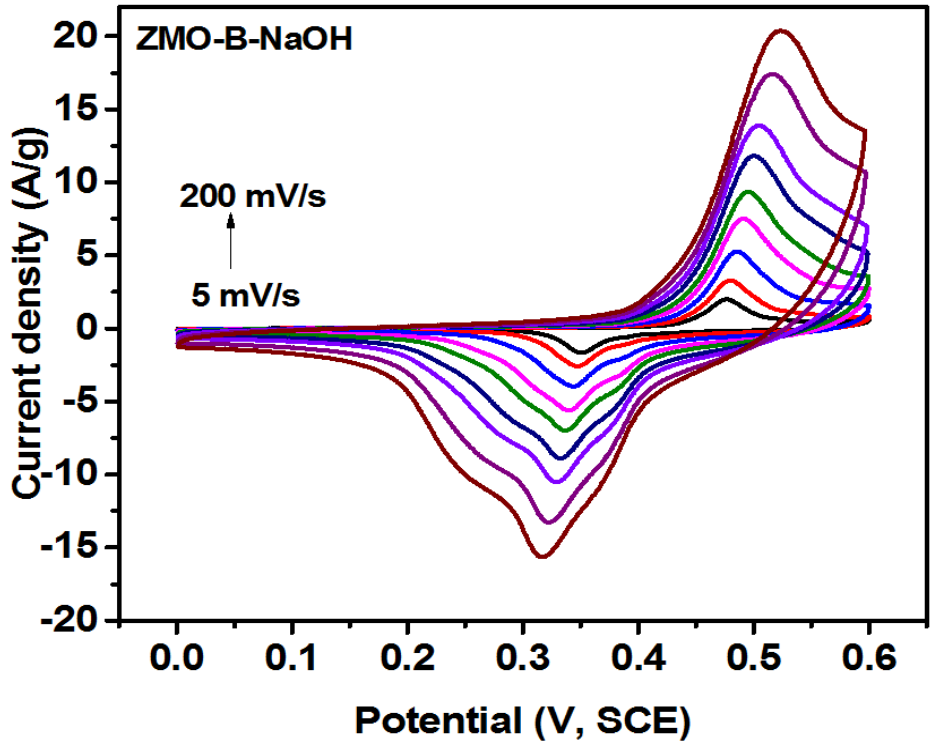

Figure 3.37: Cyclic voltammograms of ZMO-B sample at various scan rates in 3 M NaOH electrolyte.

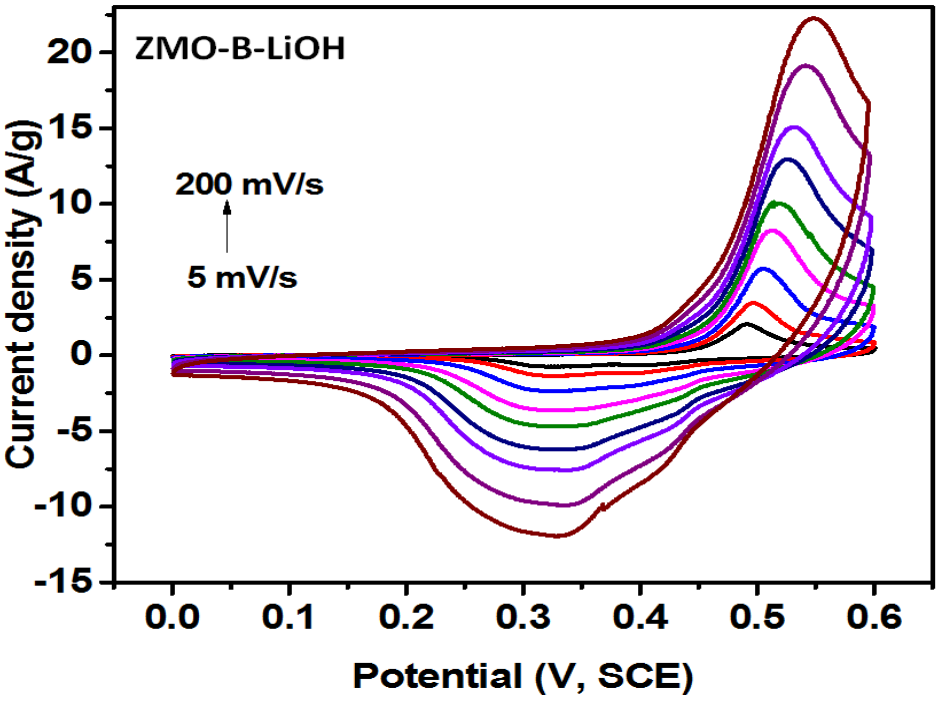

Figure 3.38: Cyclic voltammograms of ZMO-B sample at various scan rates in 3 M LiOH electrolyte.

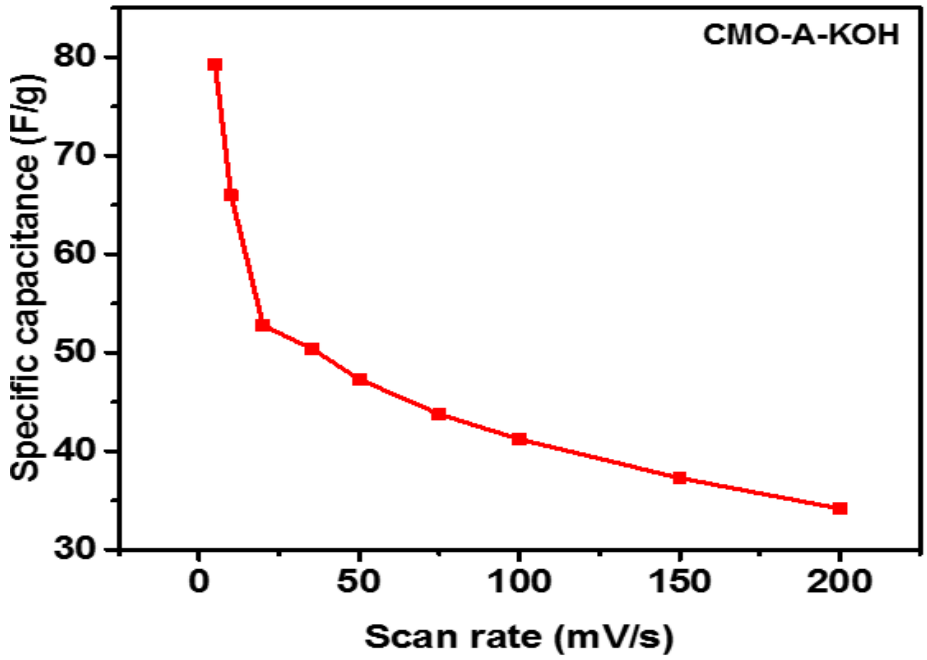

Figure 3.39: Specific capacitance as a function of scan rate for CMO-A sample in 3 M KOH electrolyte.

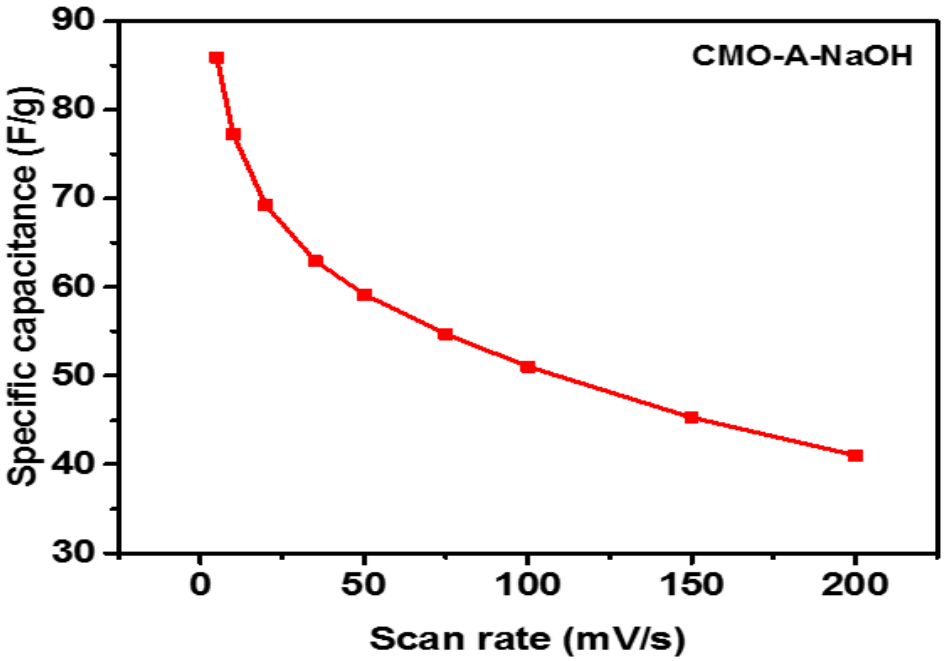

Figure 3.40: Specific capacitance as a function of scan rate for CMO-A sample in 3 M NaOH electrolyte.

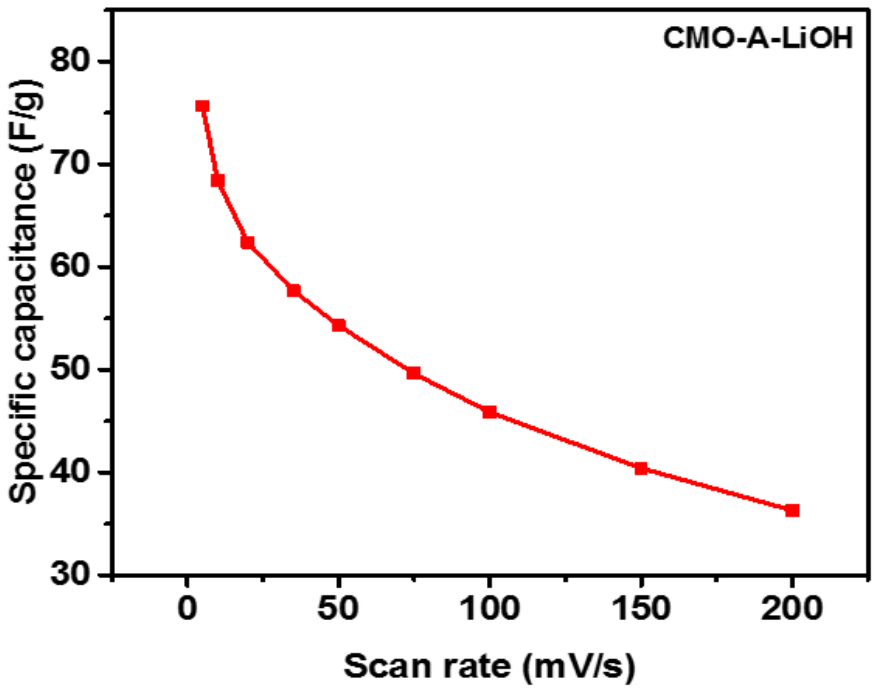

Figure 3.41: Specific capacitance as a function of scan rate for CMO-A sample in 3 M LiOH electrolyte.

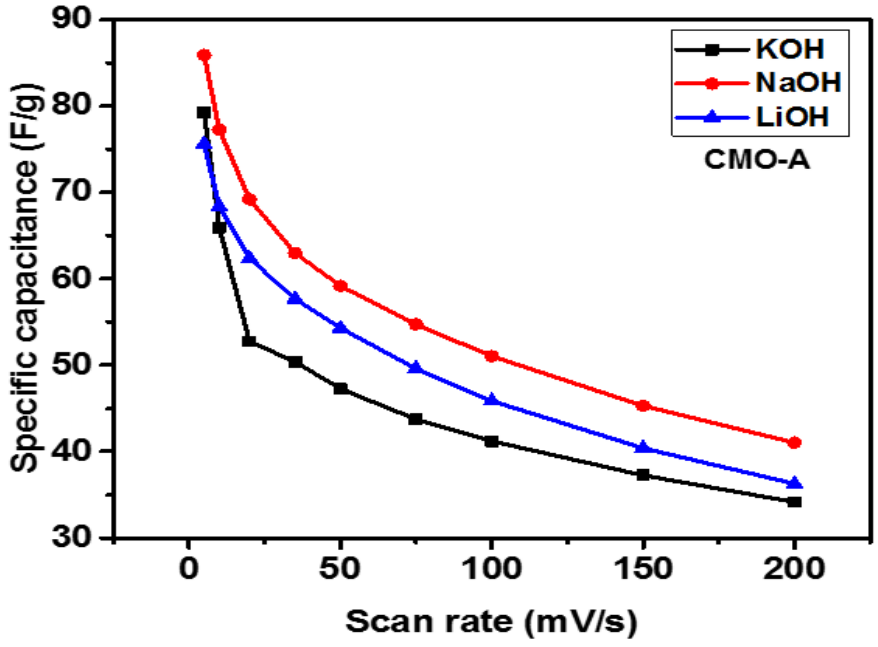

Figure 3.42: Variation of specific capacitance as a function of scan rate for CMO-A sample in different electrolytes.

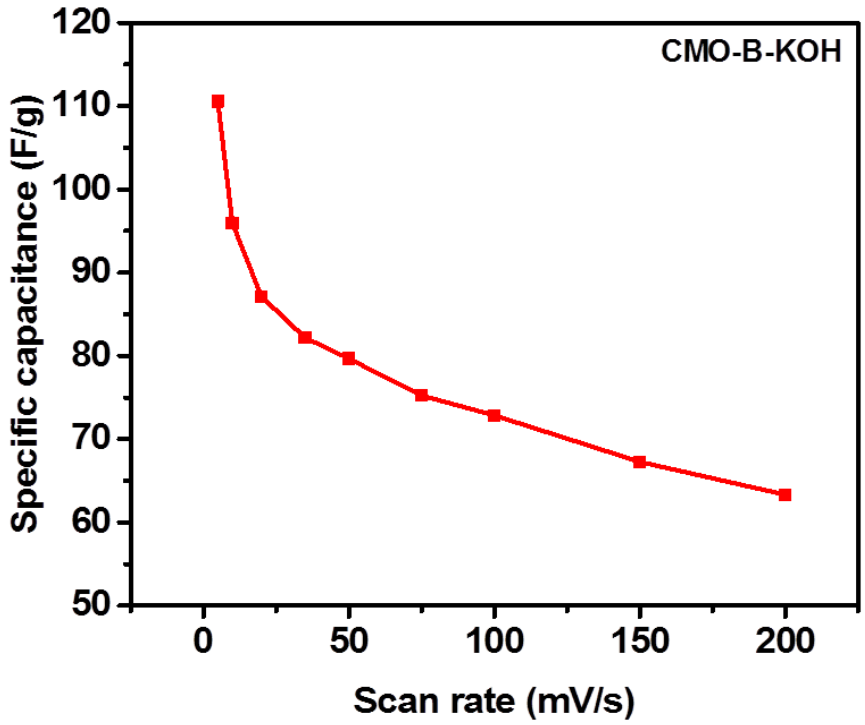

Figure 3.43: Specific capacitance as a function of scan rate for CMO-B sample in 3 M KOH electrolyte.

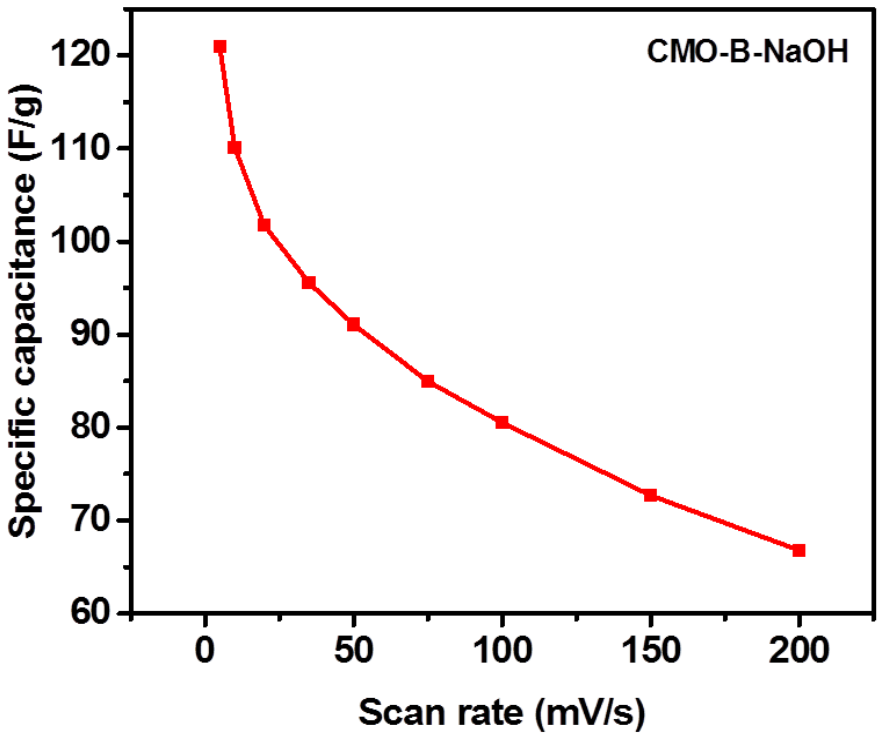

Figure 3.44: Specific capacitance as a function of scan rate for CMO-B sample in 3 M NaOH electrolyte.

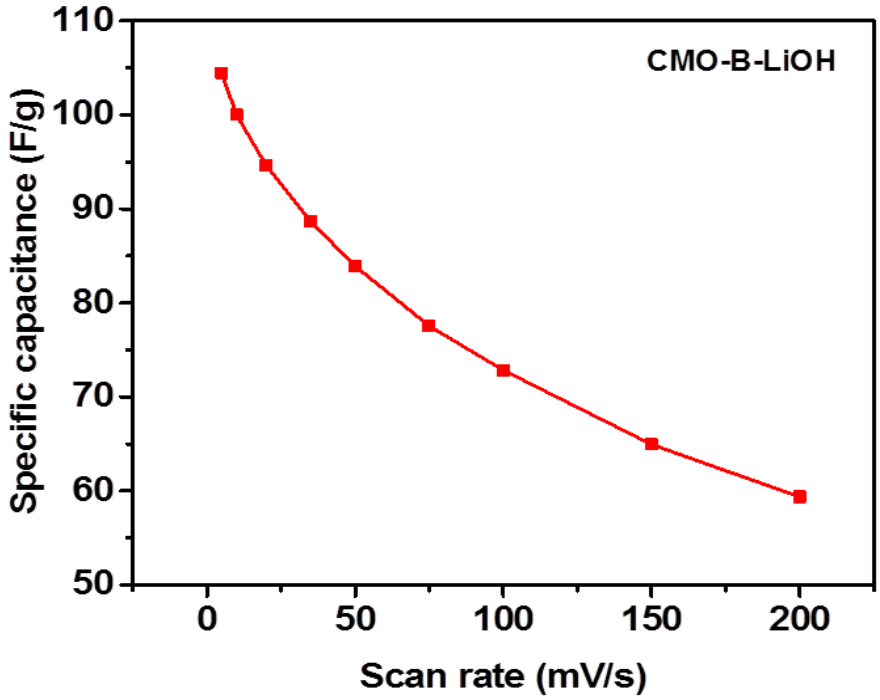

Figure 3.45: Specific capacitance as a function of scan rate for CMO-B sample in 3 M LiOH electrolyte.

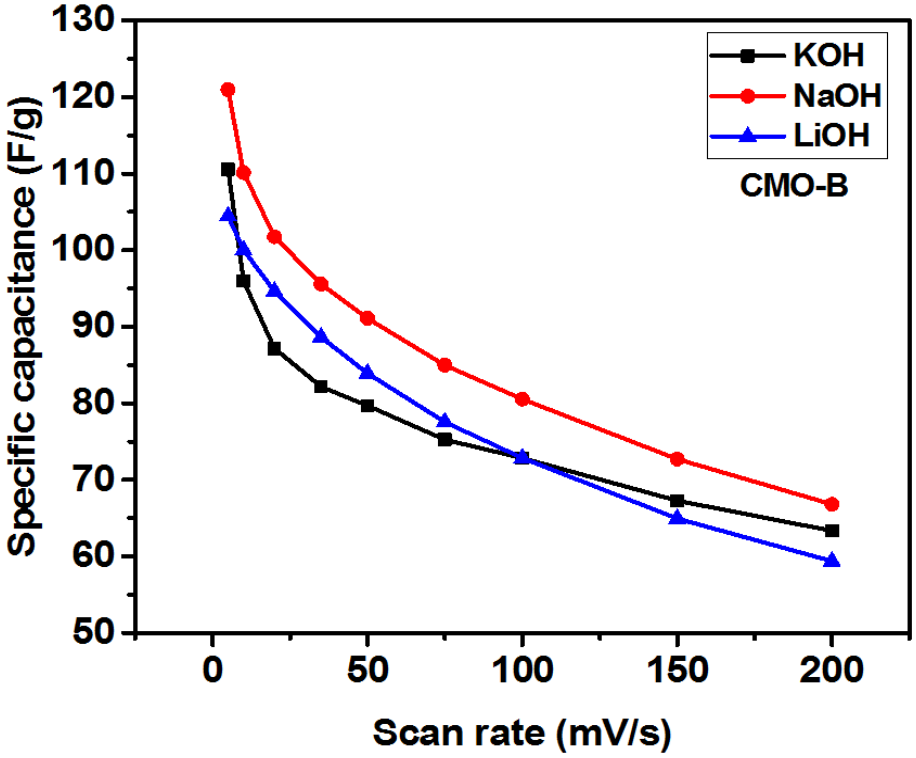

Figure 3.46: Variation of specific capacitance as a function of scan rate for CMO-B sample in different electrolytes.

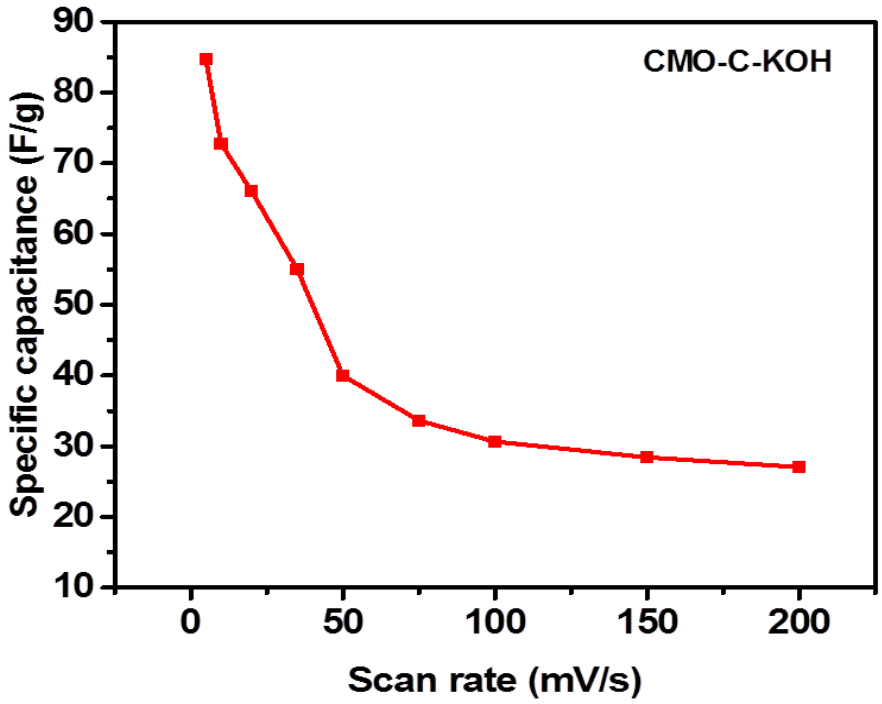

Figure 3.47: Specific capacitance as a function of scan rate for CMO-C sample in 3 M KOH electrolyte.

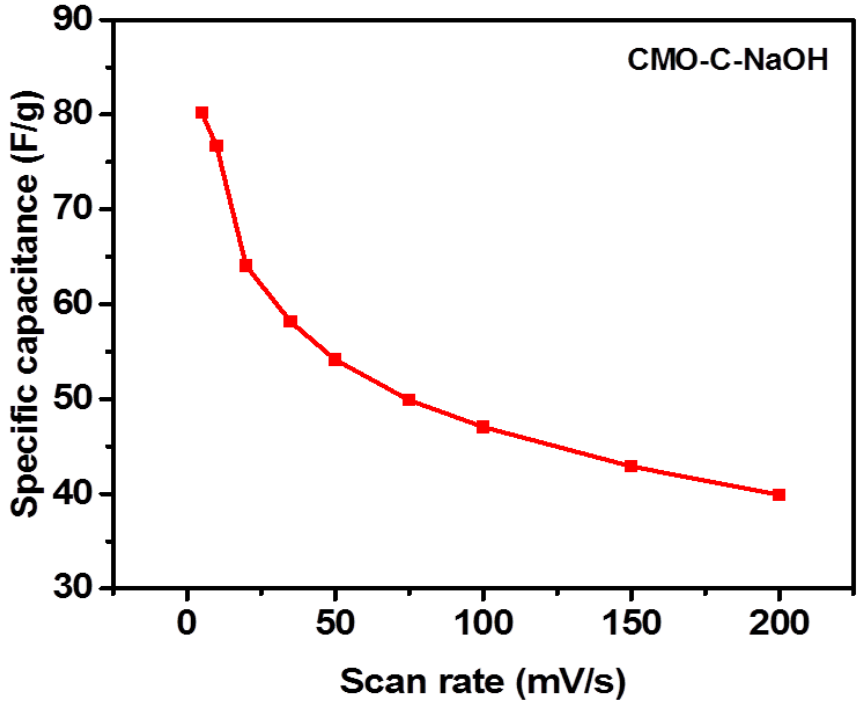

Figure 3.48: Specific capacitance as a function of scan rate for CMO-C sample in 3 M NaOH electrolyte.

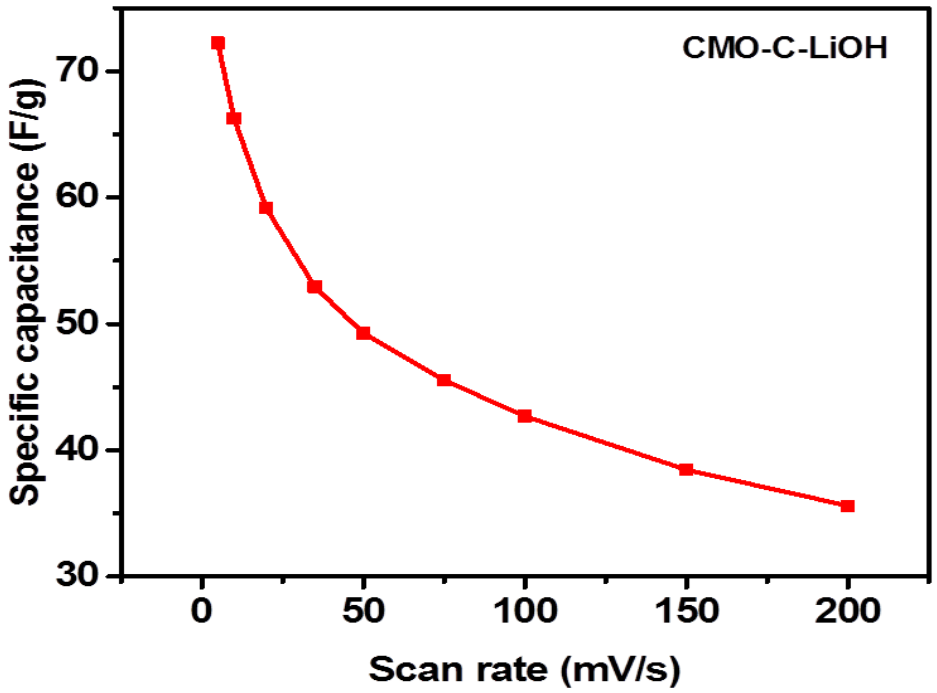

Figure 3.49: Specific capacitance as a function of scan rate for CMO-C sample in 3 M LiOH electrolyte.

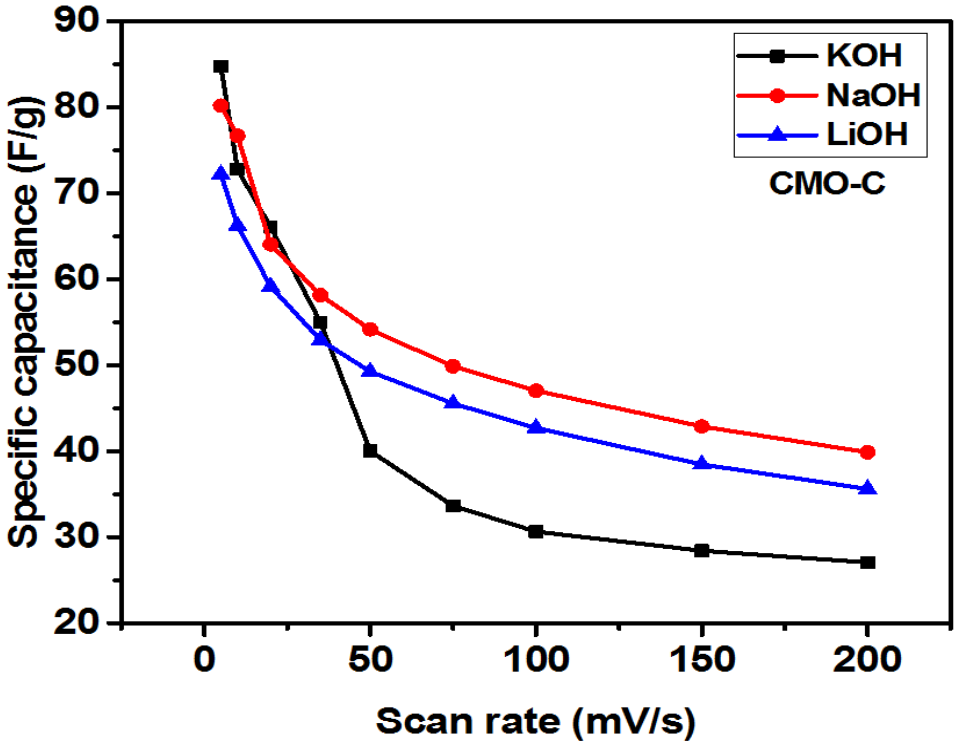

Figure 3.50: Variation of specific capacitance as a function of scan rate for CMO-C sample in different electrolytes.

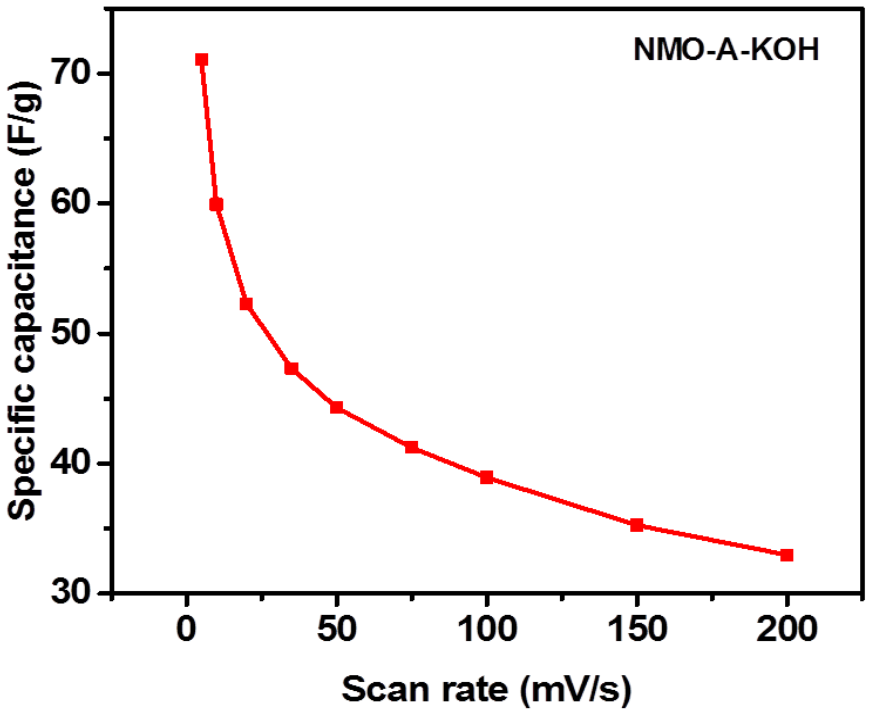

Figure 3.51: Specific capacitance as a function of scan rate for NMO-A sample in 3 M KOH electrolyte.

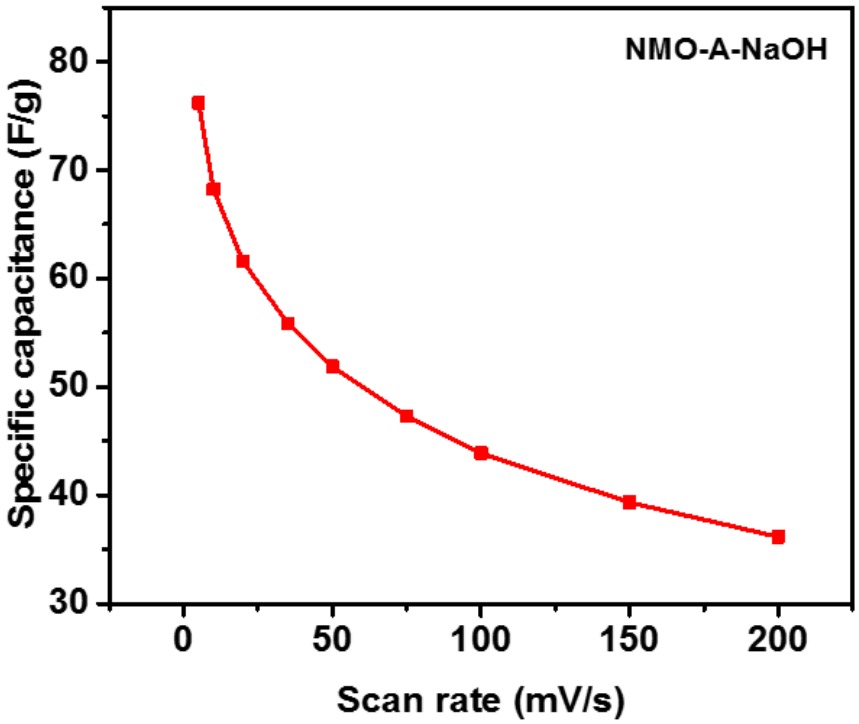

Figure 3.52: Specific capacitance as a function of scan rate for NMO-A sample in 3 M NaOH electrolyte.

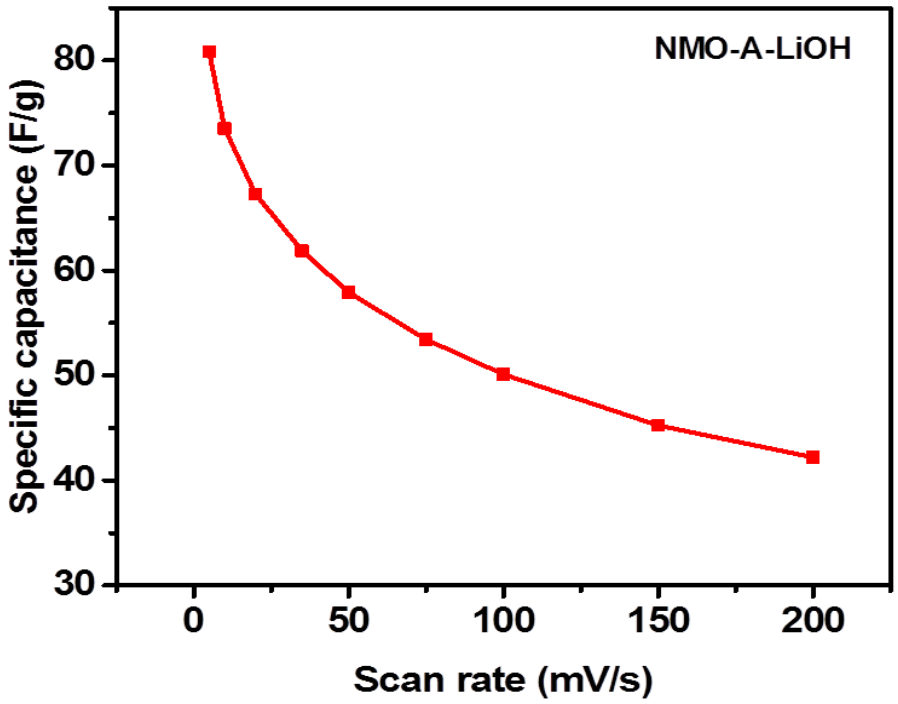

Figure 3.53: Specific capacitance as a function of scan rate for NMO-A sample in 3 M LiOH electrolyte.

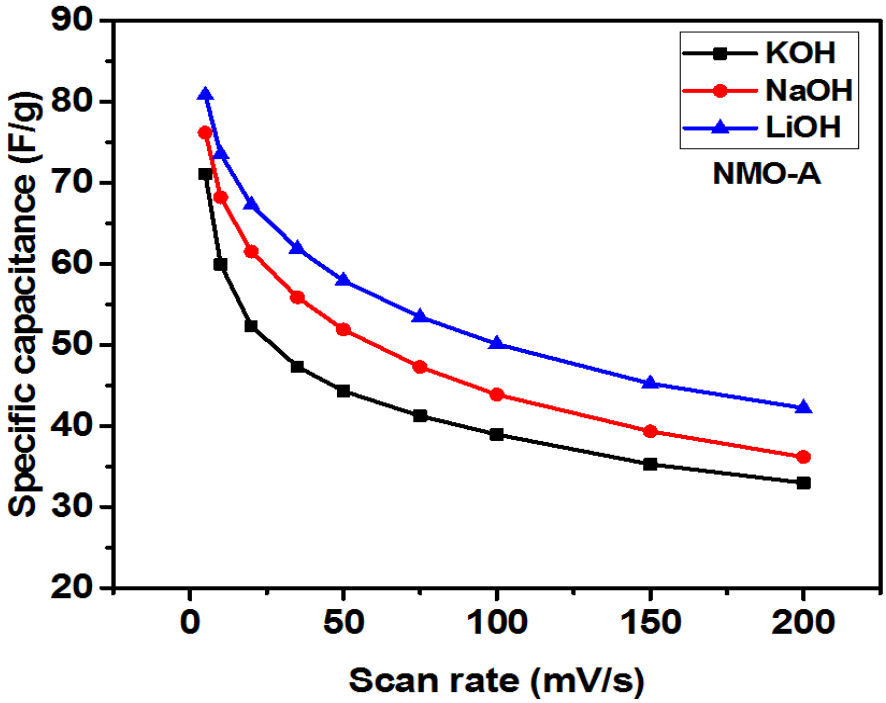

Figure 3.54: Variation of specific capacitance as a function of scan rate for NMO-A sample in different electrolytes.

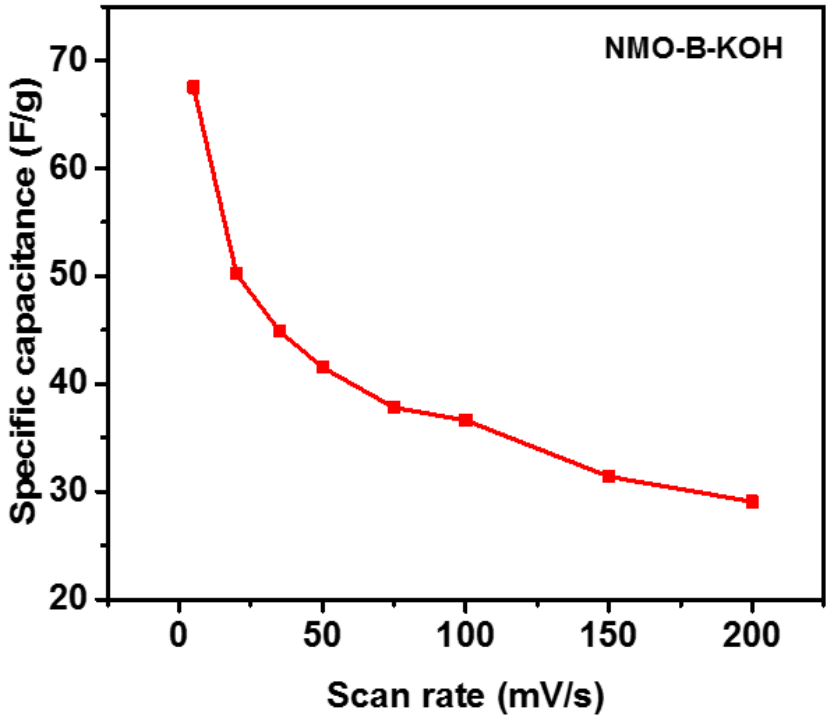

Figure 3.55: Specific capacitance as a function of scan rate for NMO-B sample in 3 M KOH electrolyte.

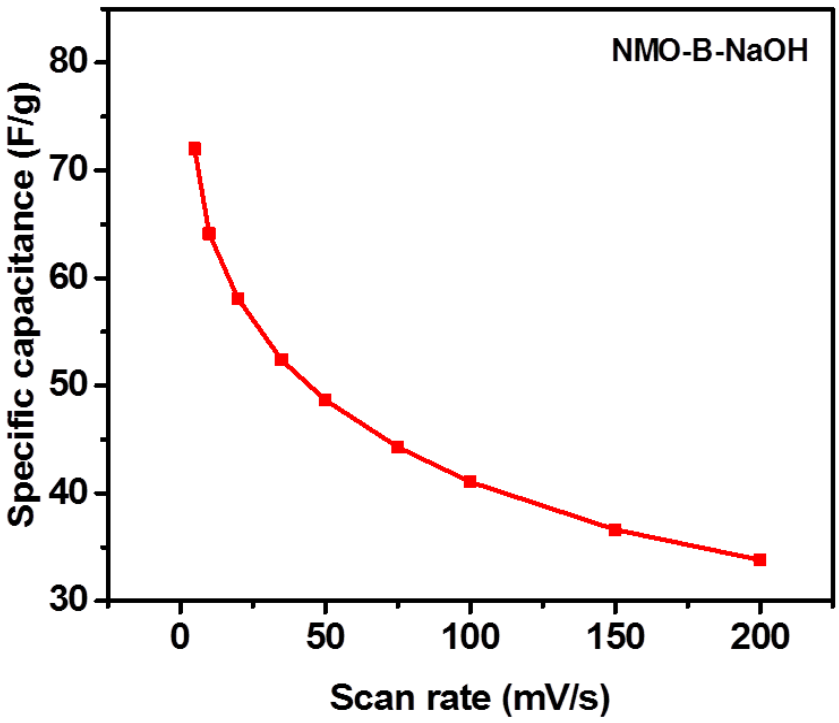

Figure 3.56: Specific capacitance as a function of scan rate for NMO-B sample in 3 M NaOH electrolyte.

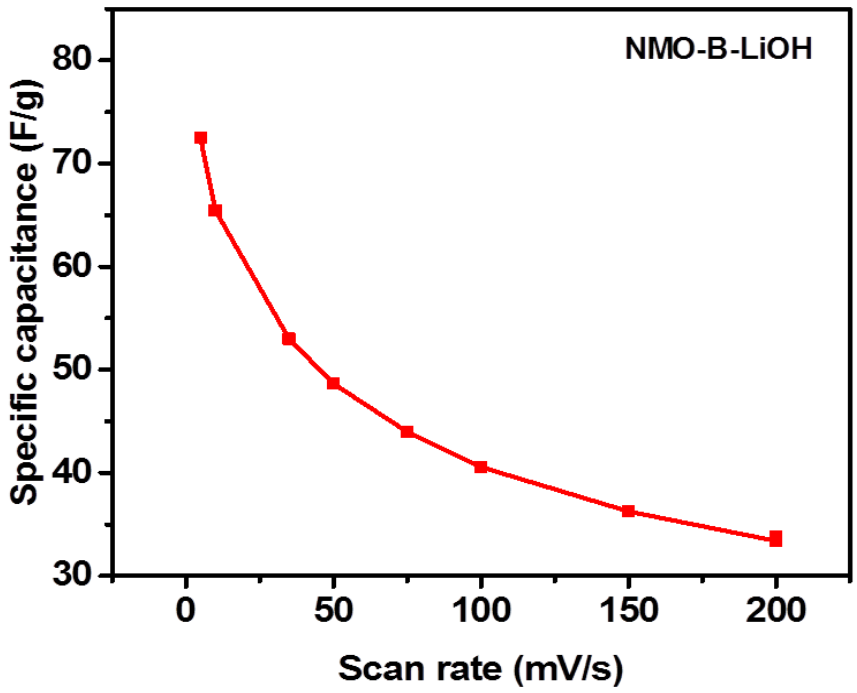

Figure 3.57: Specific capacitance as a function of scan rate for NMO-B sample in 3 M LiOH electrolyte.

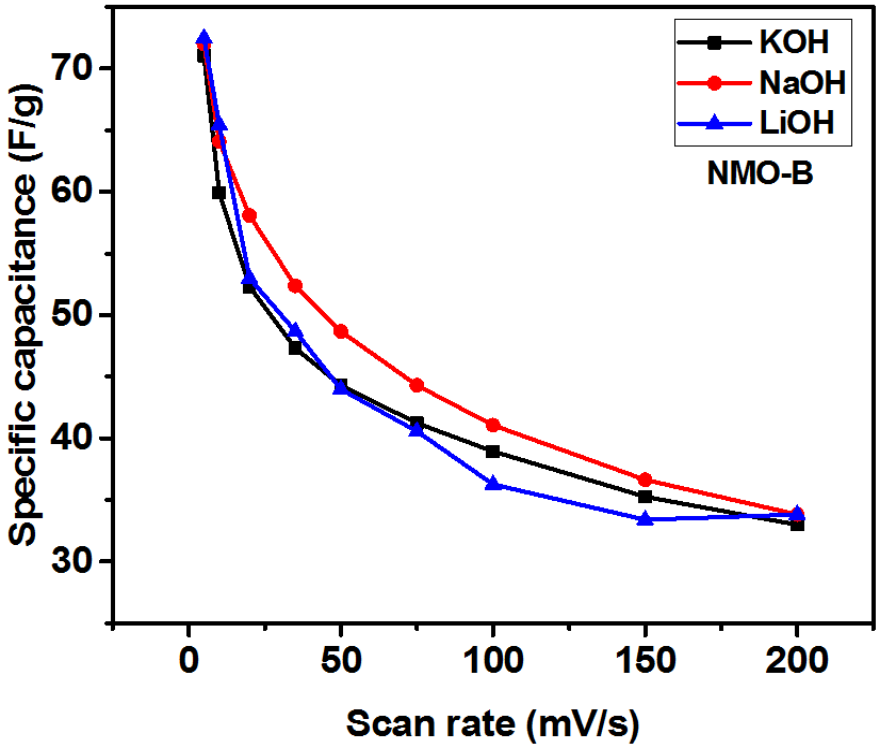

Figure 3.58: Variation of specific capacitance as a function of scan rate for NMO-B sample in different electrolytes.

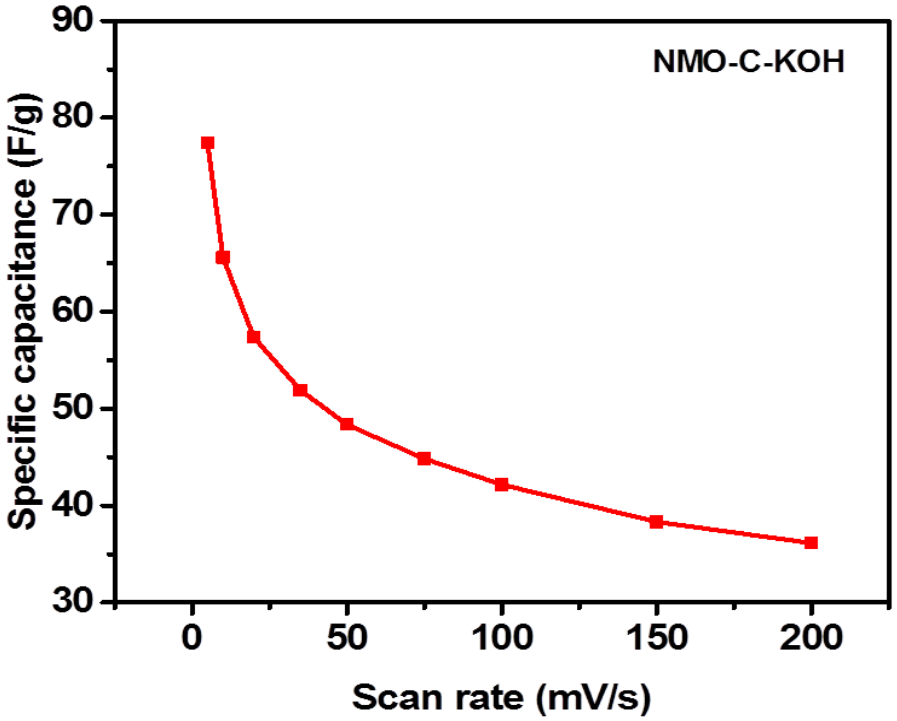

Figure 3.59: Specific capacitance as a function of scan rate for NMO-C sample in 3 M KOH electrolyte.

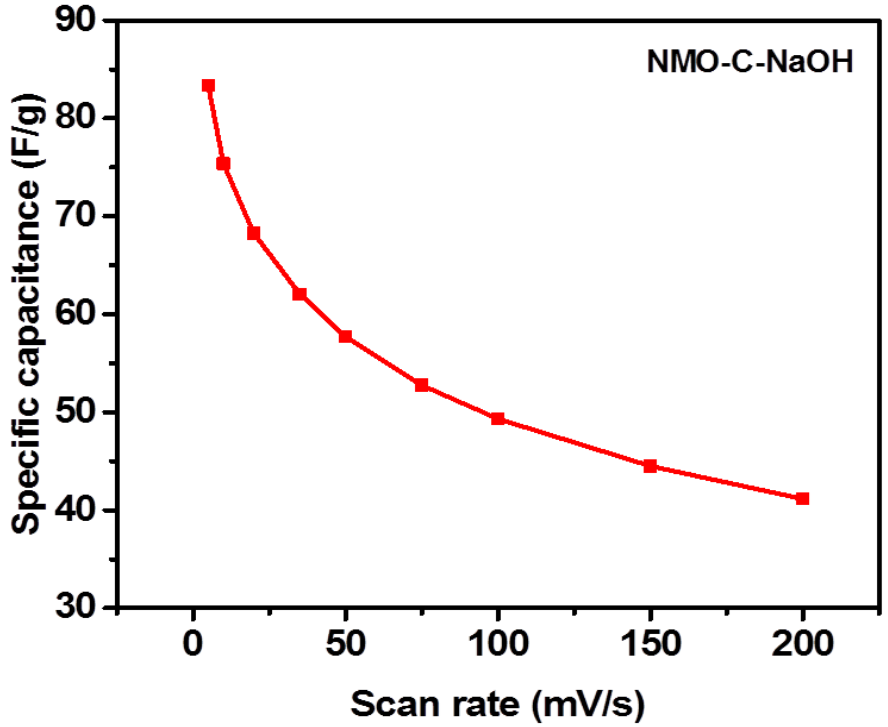

Figure 3.60: Specific capacitance as a function of scan rate for NMO-C sample in 3 M NaOH electrolyte.

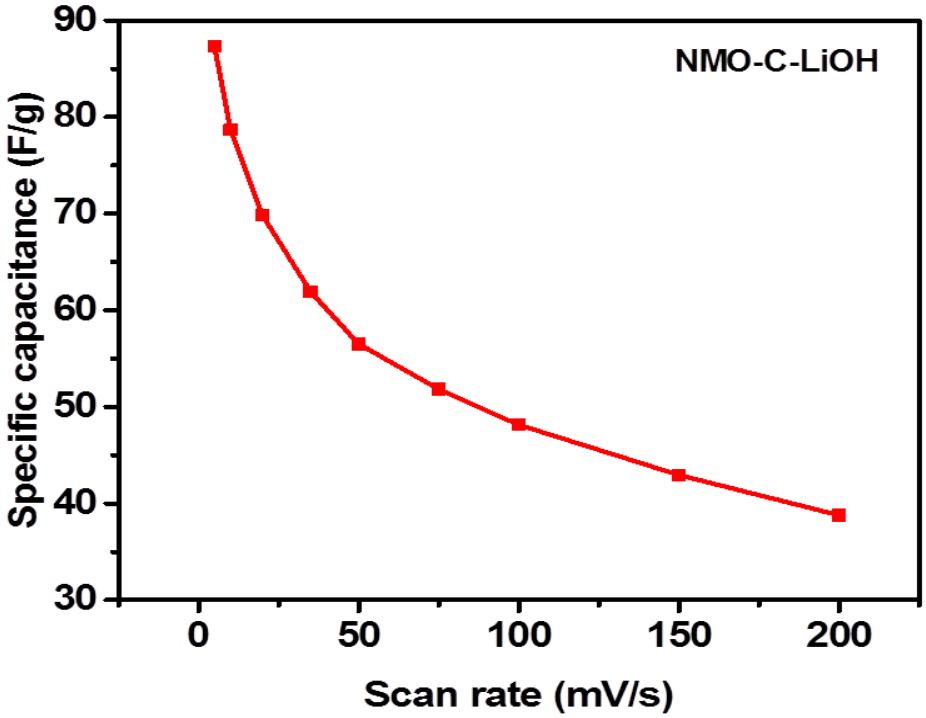

Figure 3.61: Specific capacitance as a function of scan rate for NMO-C sample in 3 M LiOH electrolyte.

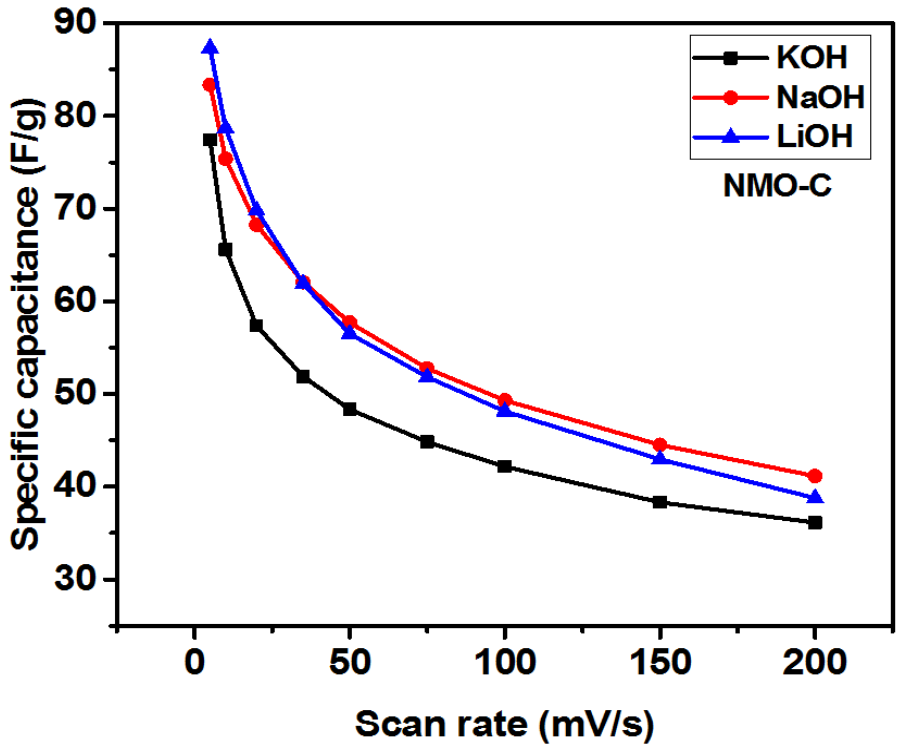

Figure 3.62: Variation of specific capacitance as a function of scan rate for NMO-C sample in different electrolytes.

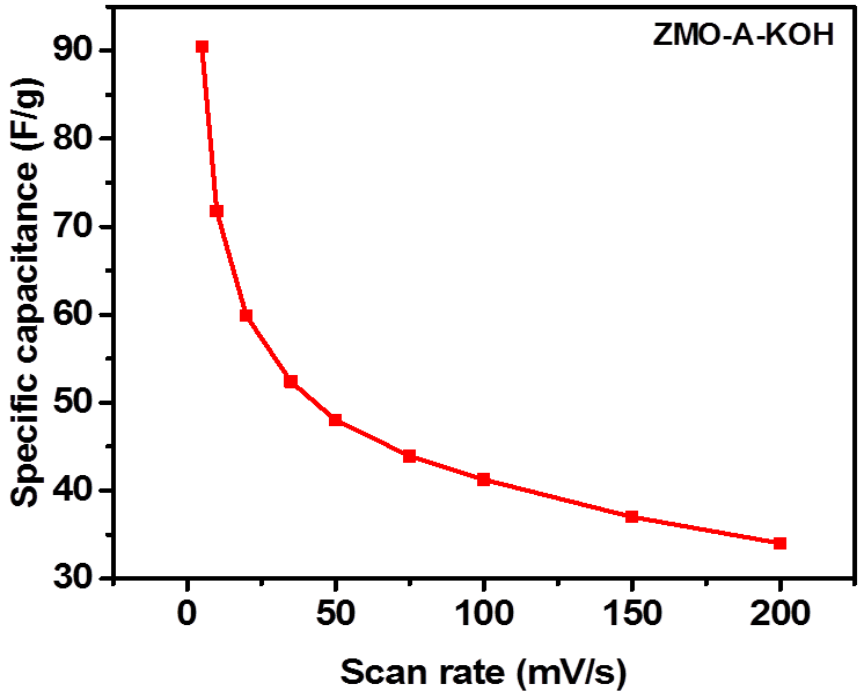

Figure 3.63: Specific capacitance as a function of scan rate for ZMO-A sample in 3 M KOH electrolyte.

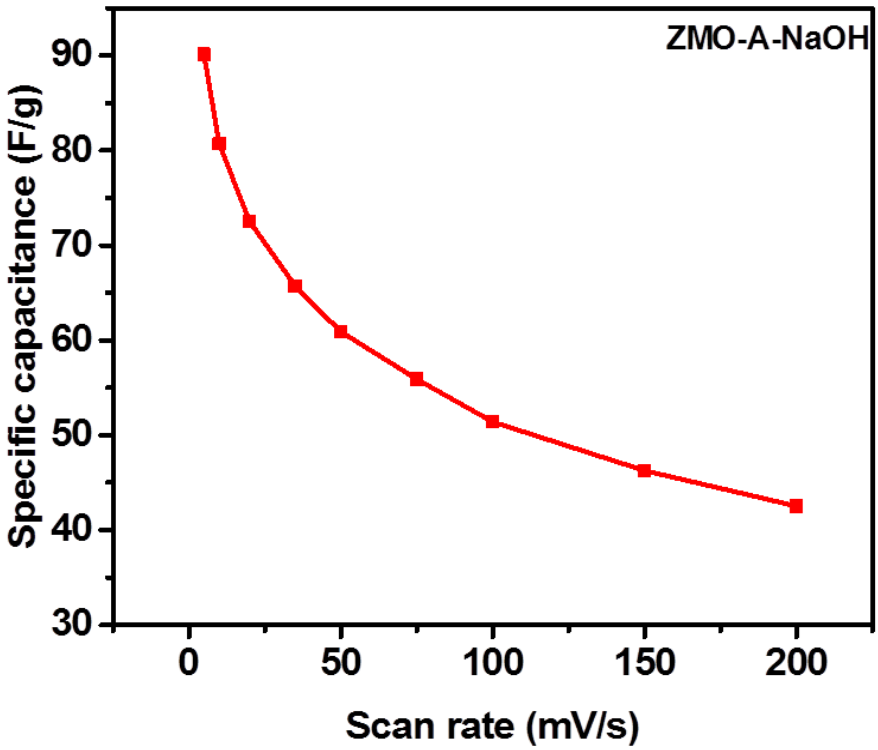

Figure 3.64: Specific capacitance as a function of scan rate for ZMO-A sample in 3 M NaOH electrolyte.

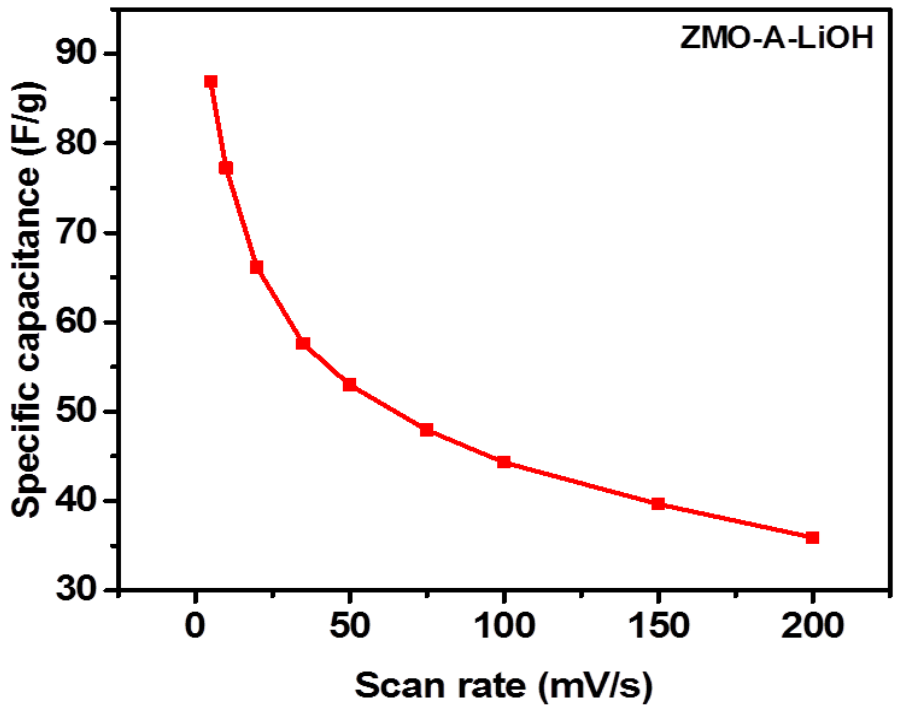

Figure 3.65: Specific capacitance as a function of scan rate for ZMO-A sample in 3 M LiOH electrolyte.

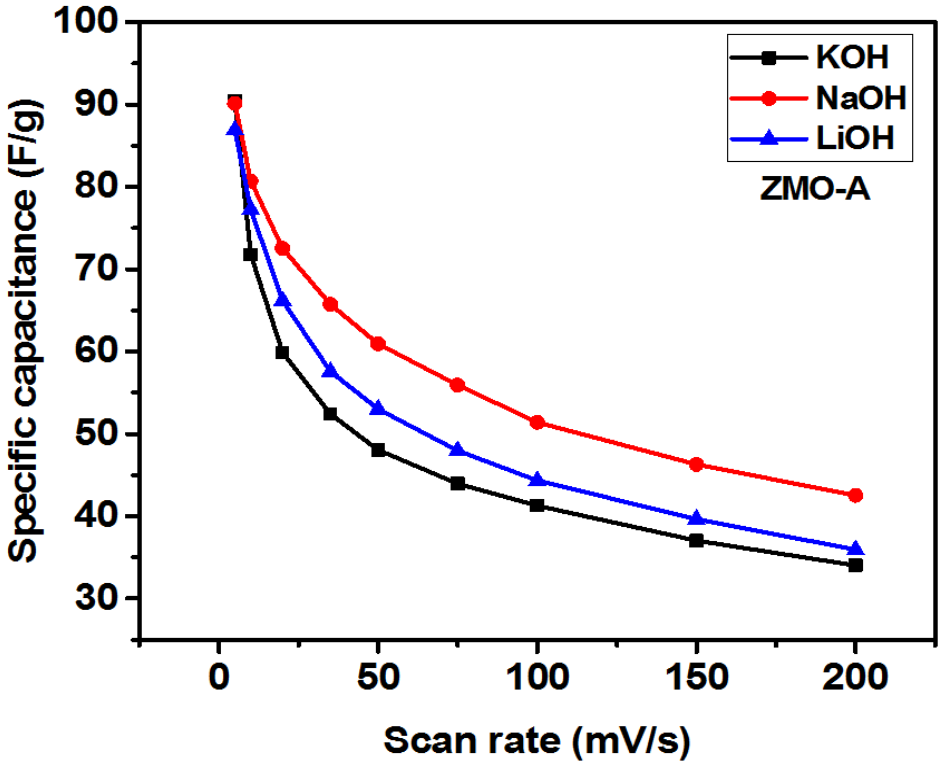

Figure 3.66: Variation of specific capacitance as a function of scan rate for ZMO-A sample in different electrolytes.

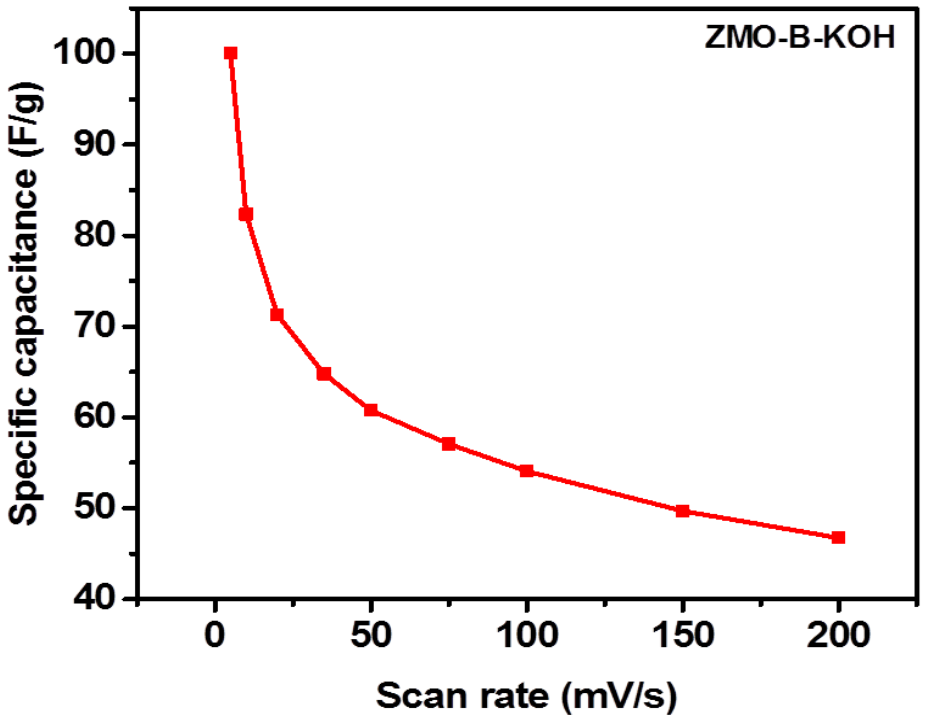

Figure 3.67: Specific capacitance as a function of scan rate for ZMO-B sample in 3 M KOH electrolyte.

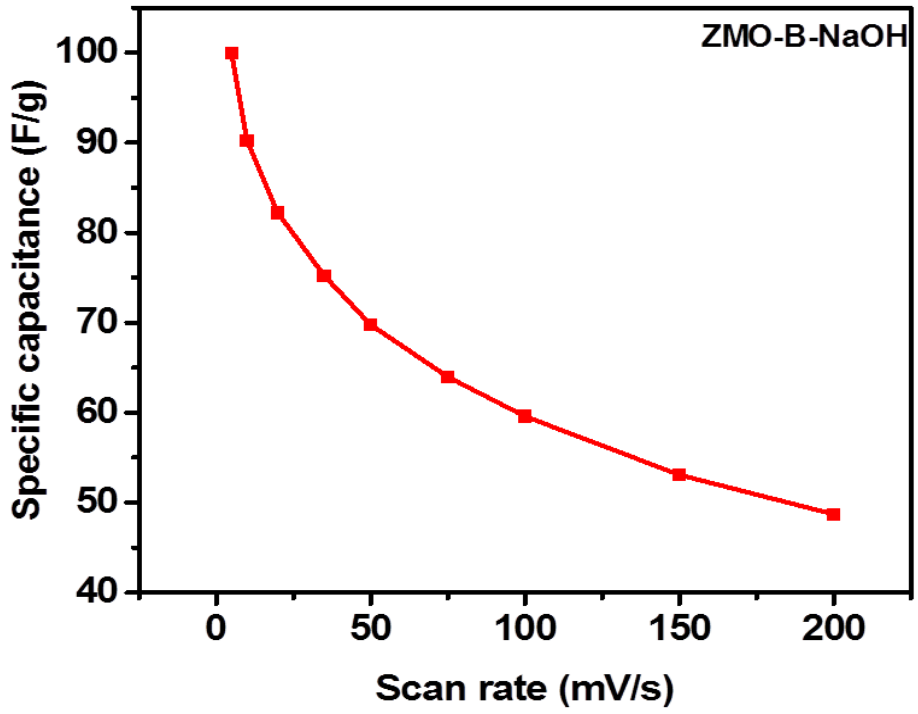

Figure 3.68: Specific capacitance as a function of scan rate for ZMO-B sample in 3 M NaOH electrolyte.

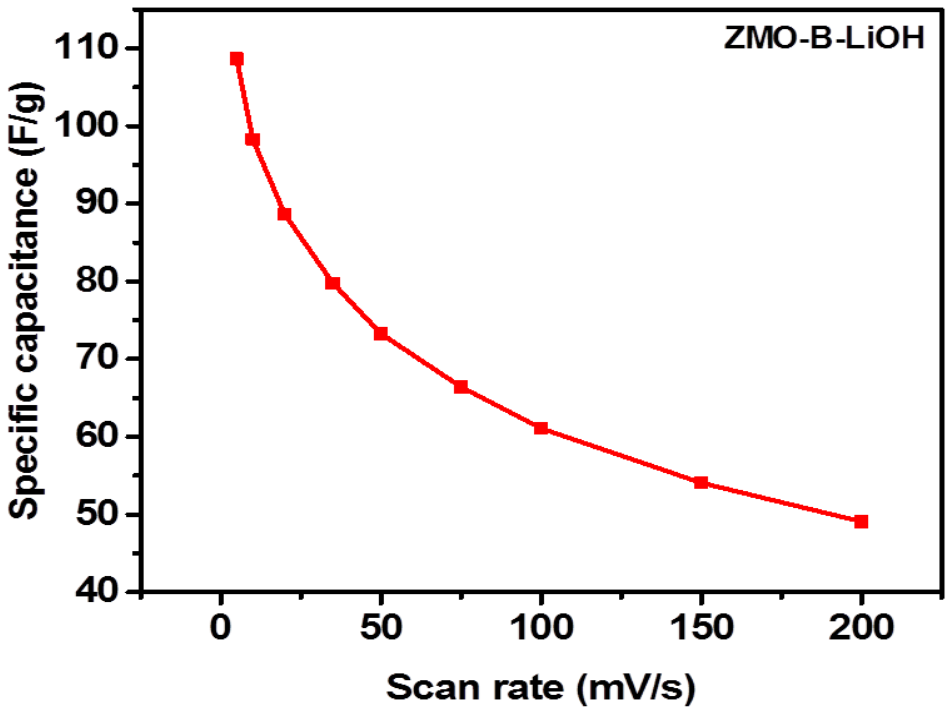

Figure 3.69: Specific capacitance as a function of scan rate for ZMO-B sample in 3 M LiOH electrolyte.

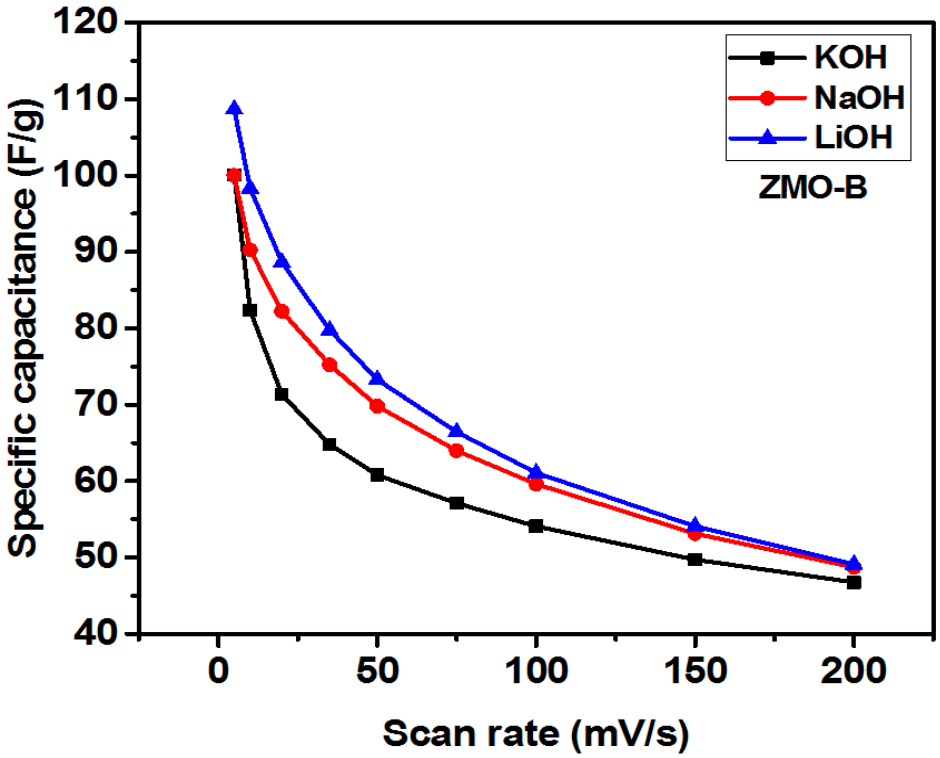

Figure 3.70: Variation of specific capacitance as a function of scan rate for ZMO-B sample in different electrolytes.

Galvanostatic charge-discharge measurements were performed to evaluate the potential application of the TMOs nanofibers as electrode materials for energy storage devices. The charge-discharge measurements were performed in three different electrolytes, 3M LiOH, NaOH and KOH, in the potential window of 0 to 0.6V (*vs.* SCE). The charge-discharge study was performed at various discharge current densities. The charge-discharge characteristics of CMO-B sample at various applied currents in different electrolytes are shown in Figures 3.71-3.73. As seen in these figures, the charge-discharge profile is very symmetrical in nature suggesting high electrochemical stability and reversibility of the Faradaic reactions [22][23].

The specific capacitance of the electrodes was calculated from the discharging curves. The specific capacitance (C_{sp}) of the electrode was calculated using the equation given below [24]:

$$C_{sp} = \frac{I \times \Delta t}{\Delta V \times m} \qquad \text{.....(4)}$$

where I is the discharge current (A), Δt is the discharge time (s), ΔV is the potential window (V), and m is the mass of the metal oxide powder. As seen, when discharge current is increased, the specific capacitance of the metal oxide nanofibers decreased (Figures 3.74-3.81). The decrease in the specific capacitance with increase in the discharge current is due to higher potential drop and insufficient Faradic redox reaction at higher discharge currents [25].

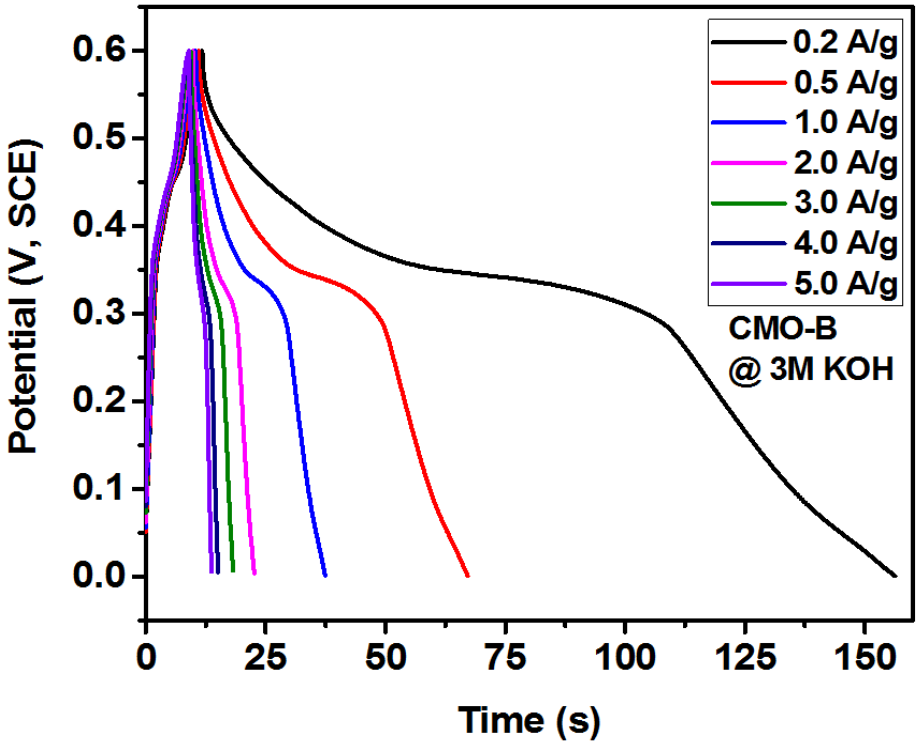

Figure 3.71: Galvanostatic charge-discharge characteristics of CMO-B electrode at various applied currents in 3M KOH electrolyte.

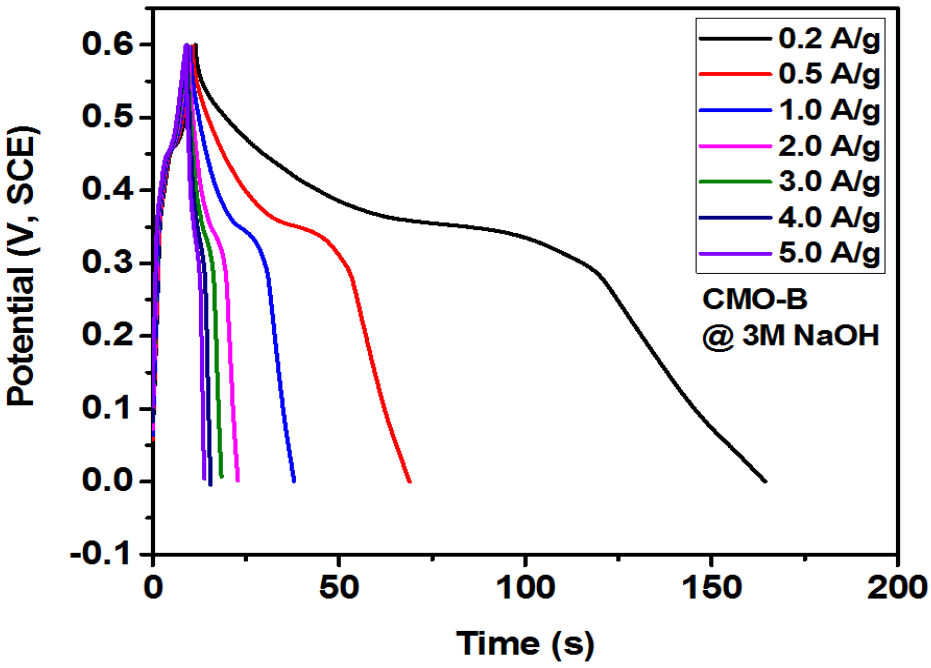

Figure 3.72: Galvanostatic charge-discharge characteristics of CMO-B electrode at various applied currents in 3M NaOH electrolyte.

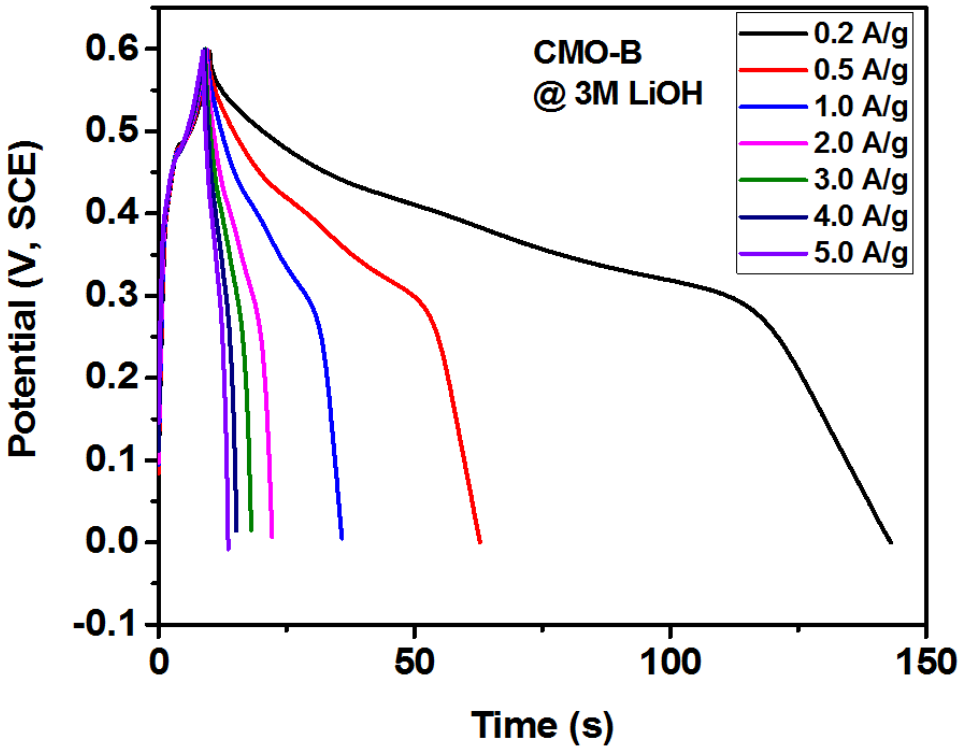

Figure 3.73: Galvanostatic charge-discharge characteristics of CMO-B electrode at various applied currents in 3M NaOH electrolyte.

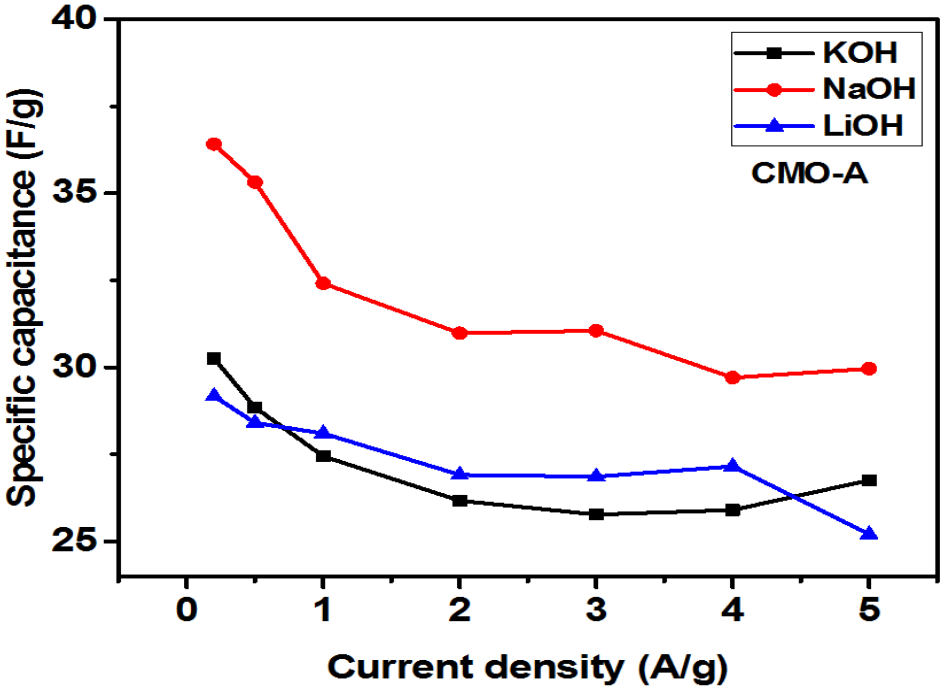

Figure 3.74: Variation of specific capacitance with applied current in different electrolytes for CMO-A sample.

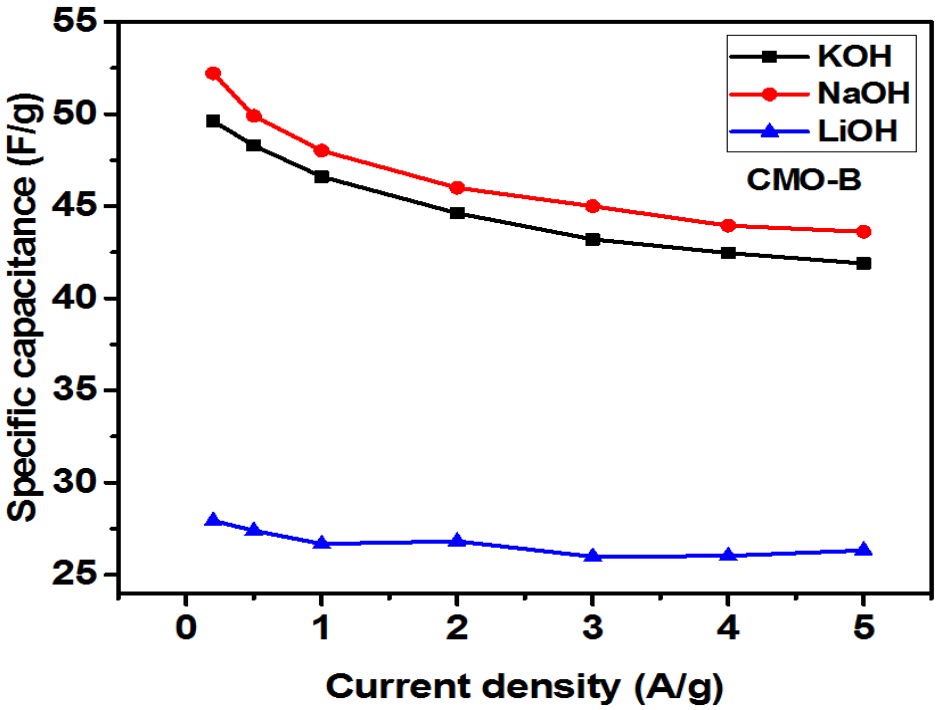

Figure 3.75: Variation of specific capacitance with applied current in different electrolytes for CMO-B sample.

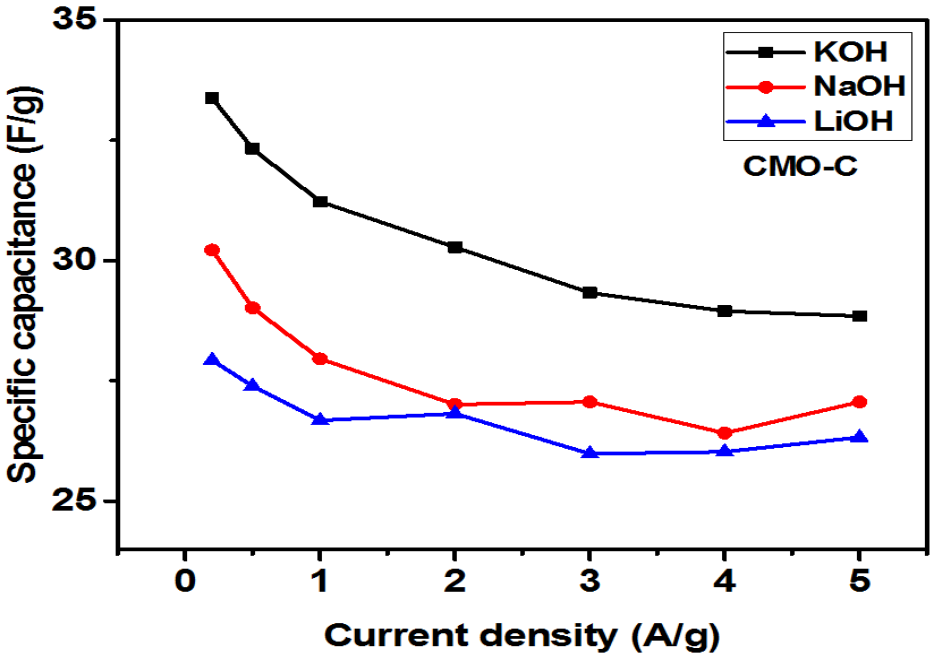

Figure 3.76: Variation of specific capacitance with applied current in different electrolytes for CMO-C sample.

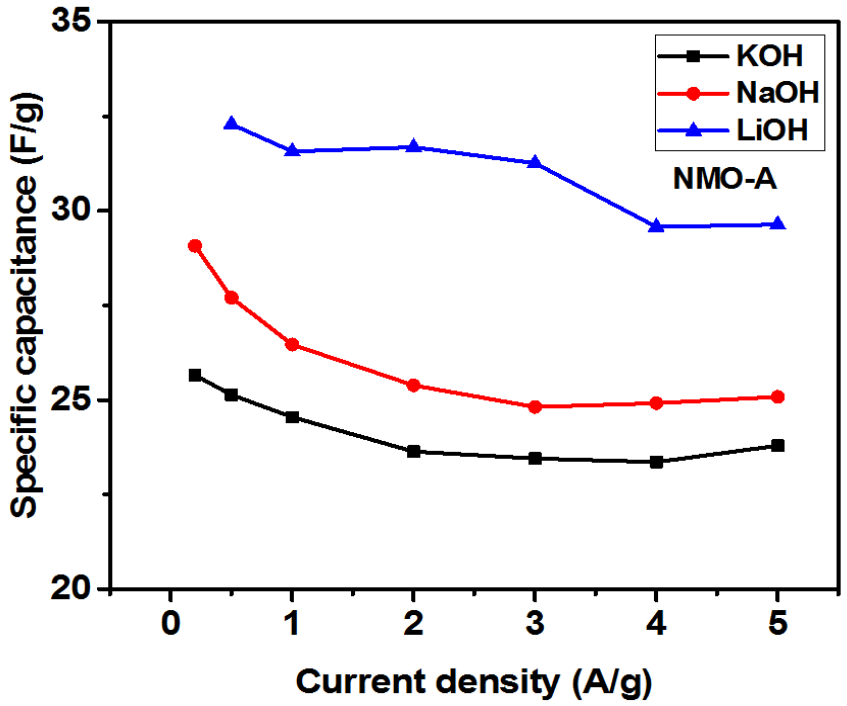

Figure 3.77: Variation of specific capacitance with applied current in different electrolytes for NMO-A sample.

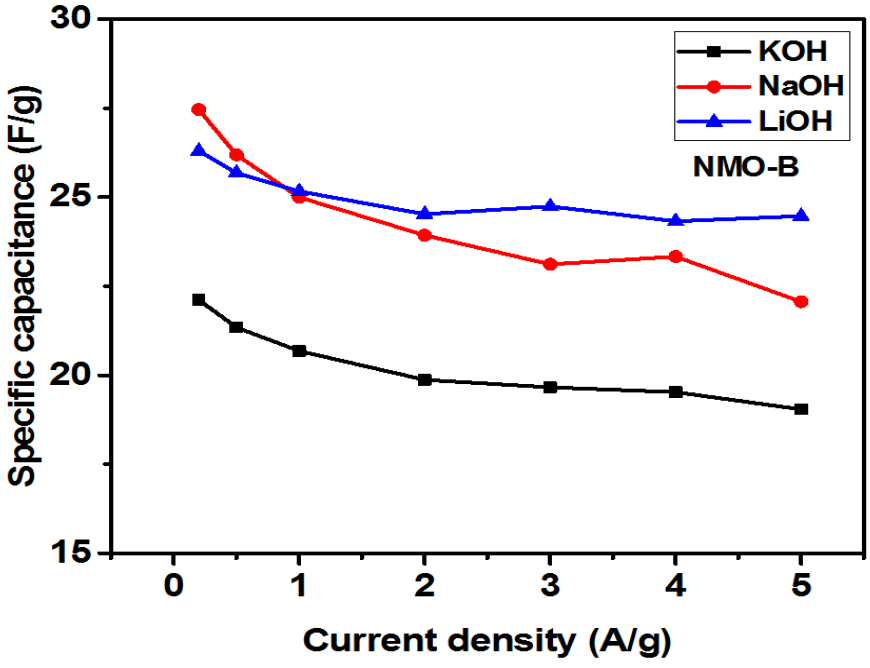

Figure 3.78: Variation of specific capacitance with applied current in different electrolytes for NMO-B sample.

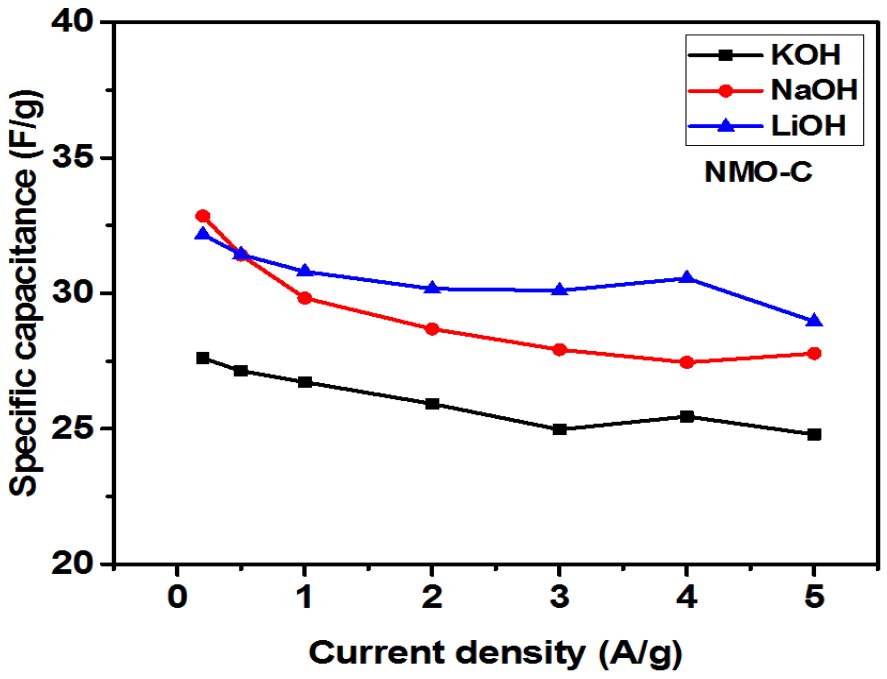

Figure 3.79: Variation of specific capacitance with applied current in different electrolytes for NMO-C sample.

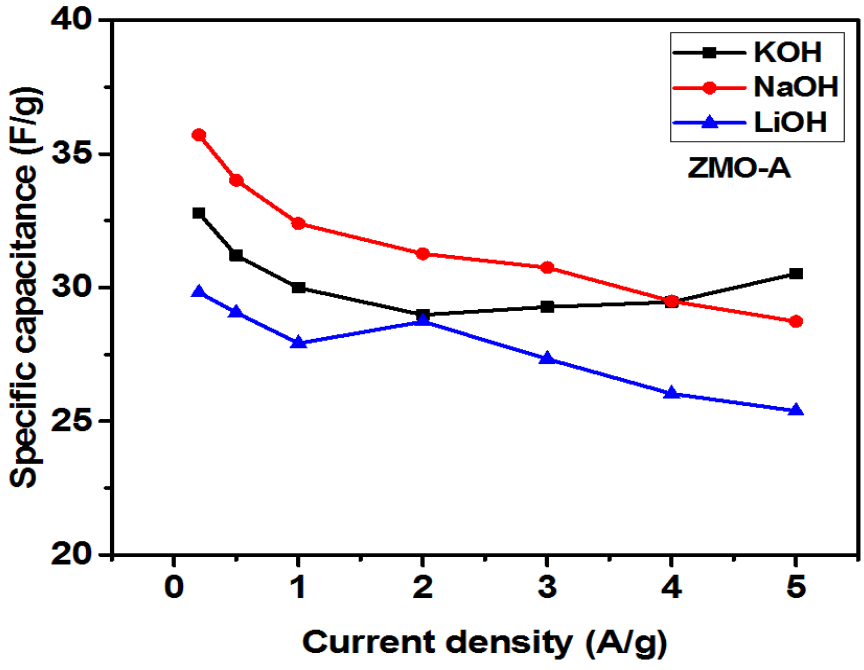

Figure 3.80: Variation of specific capacitance with applied current in different electrolytes for ZMO-A sample.

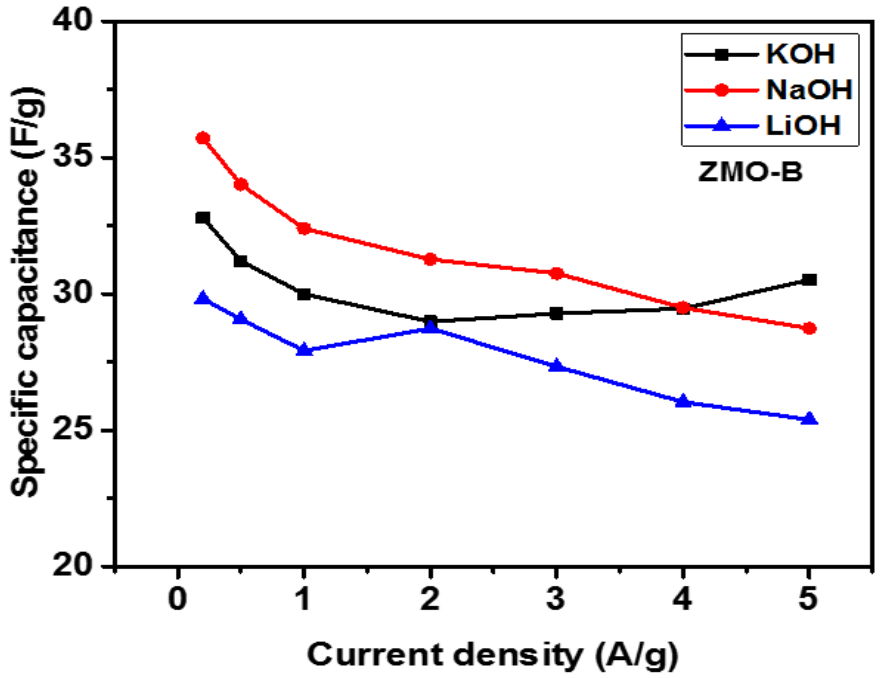

Figure 3.81: Variation of specific capacitance with applied current in different electrolytes for ZMO-B sample.

The performance of the supercapacitors was further evaluated by calculating the energy density and the power density of the metal oxide based nanofibers. The energy density and the power density of the metal oxide based electrode was calculated using the following equations [26].

$$E\left(\frac{Wh}{kg}\right) = \frac{C_{sp} \times \Delta V^2}{7.2} \quad \text{.....(5)}$$

$$P\left(\frac{W}{kg}\right) = \frac{E \times 3600}{t} \quad \text{.....(6)}$$

where C_{sp} (F/g) is the specific capacitance calculated from charge-discharge measurements, ΔV (V) is the potential window and t (s) is the discharge time.

Figures 3.81-3.88 show the relationship between power density and energy density (Ragone plot) for all the samples in 3M LiOH, NaOH and KOH electrolytes. As seen in these figures, the higher energy density is observed for the lower discharge currents, but the higher discharge currents result in higher power density. Impressively, a high energy density of 2.5 Wh/kg was obtained at a power density of 1400 W/kg for $CoMn_2O_4$ having a tube-in-tube structure. The high performance of the tube-in-tube structure could be due to the high surface area and thus more interaction of electrolyte ions with the metal oxide.

Figure 3.90 shows the variation of specific capacitance as a function of charge-discharge cycles in NaOH electrolyte for CMO-B electrode. It was observed that the specific capacitance of the electrode slowly increased with the number of cyclic charge discharge measurements. The increase in the capacitance with cyclic charge-discharge process could be due to more activation of the metal oxide sites with time [27][28].

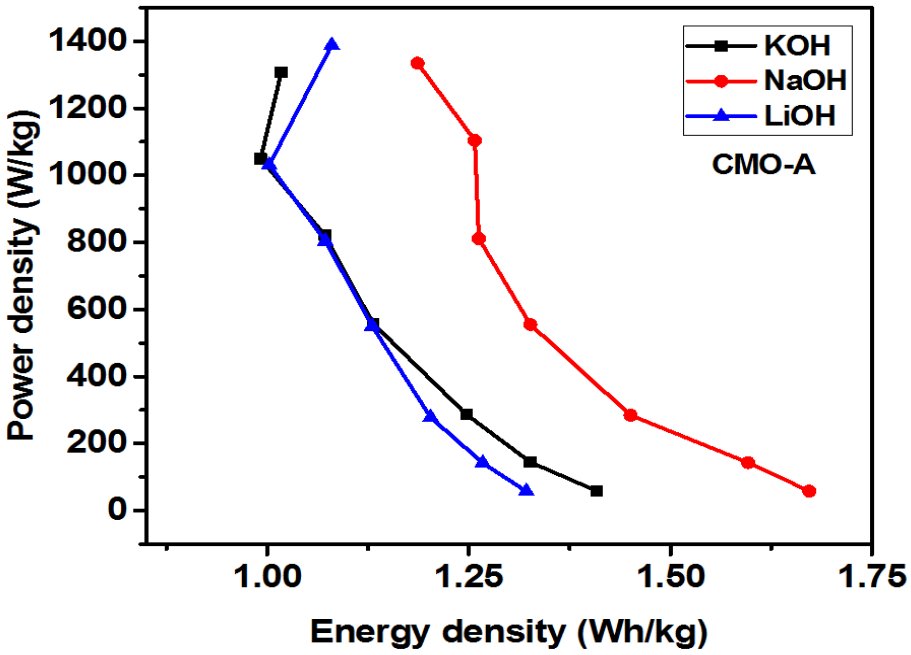

Figure 3.82: Power density versus energy density plots for CMO-A in various electrolytes.

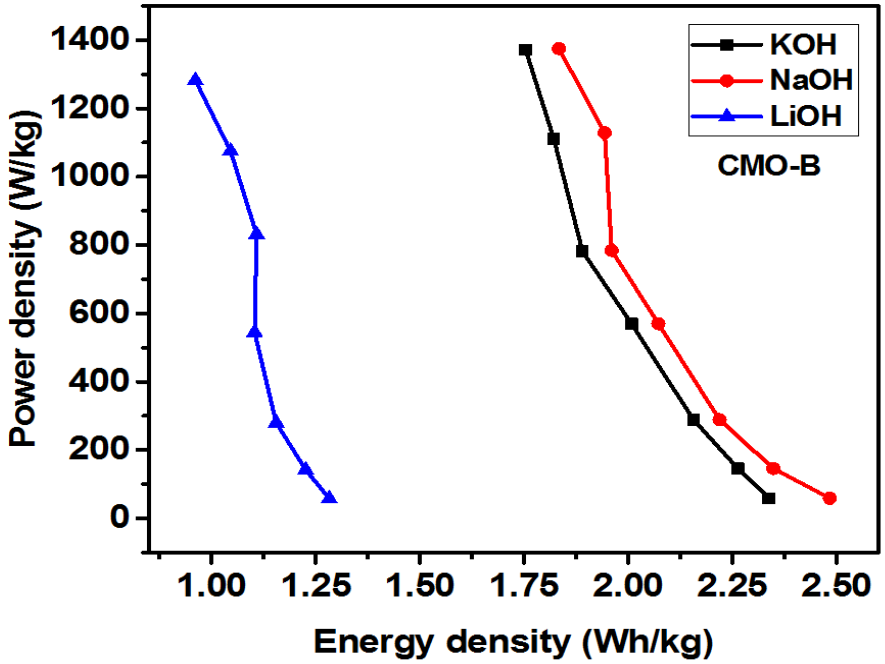

Figure 3.83: Power density versus energy density plots for CMO-B in various electrolytes.

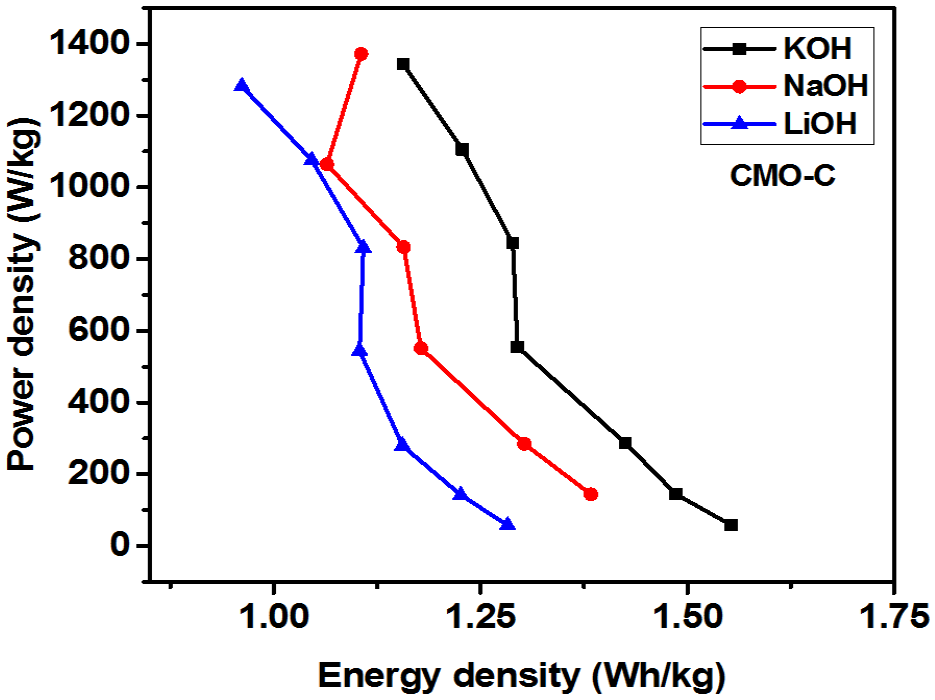

Figure 3.84: Power density versus energy density plots for CMO-C in various electrolytes.

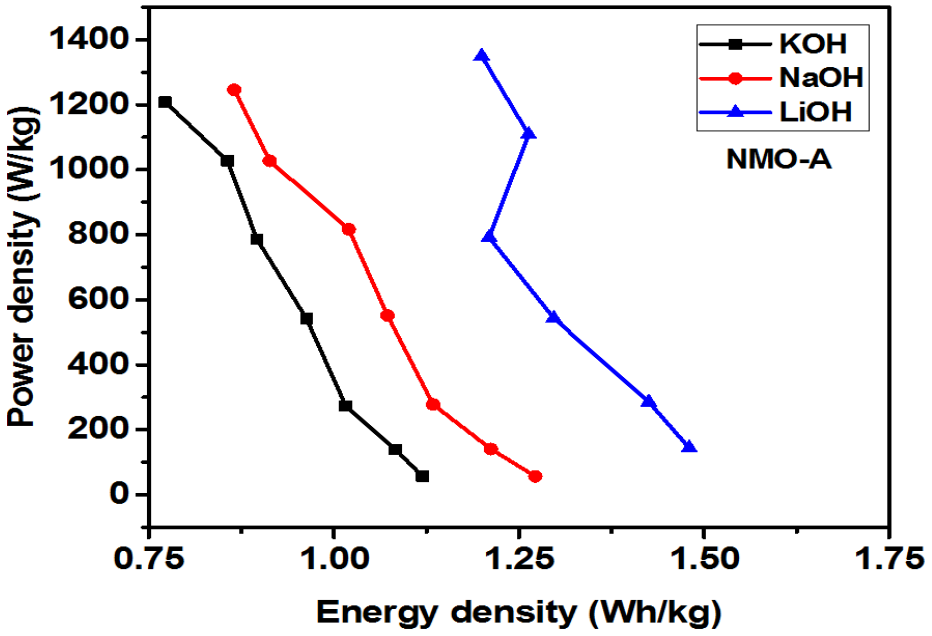

Figure 3.85: Power density versus energy density plots for NMO-A in various electrolytes.

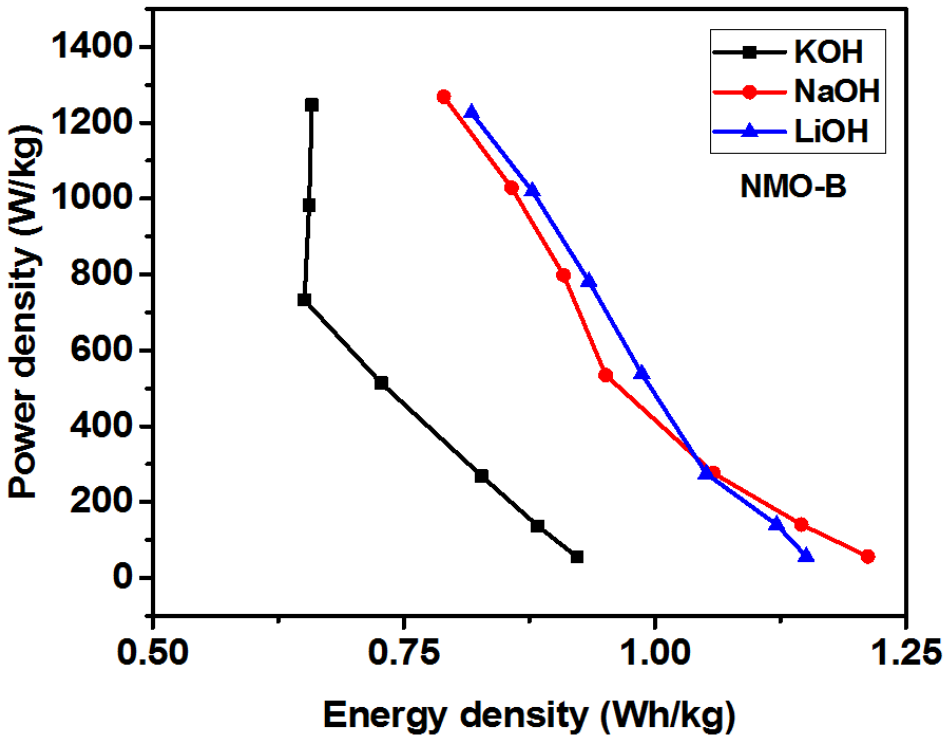

Figure 3.86: Power density versus energy density plots for NMO-B in various electrolytes.

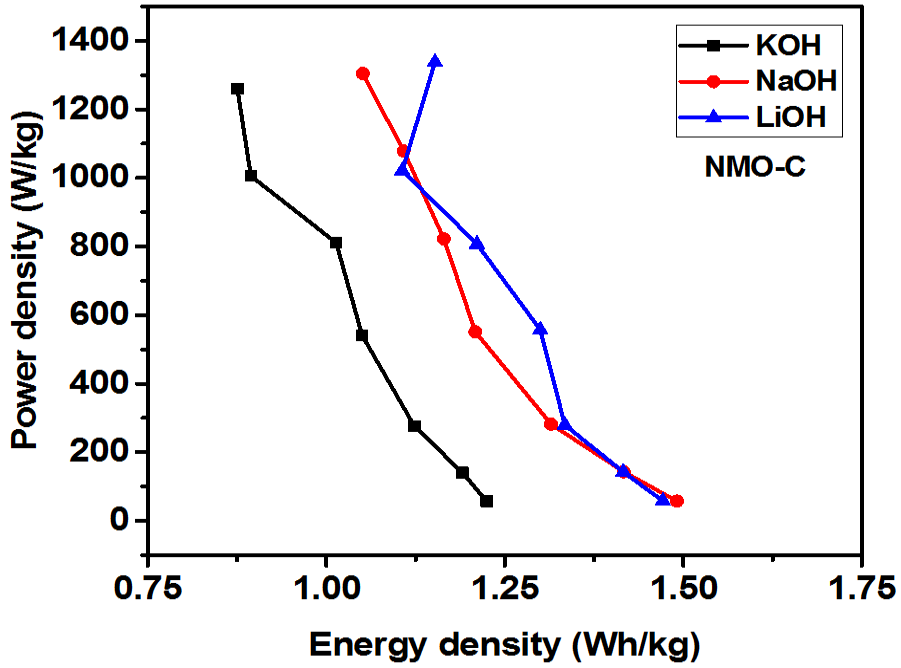

Figure 3.87: Power density versus energy density plots for NMO-C in various electrolytes.

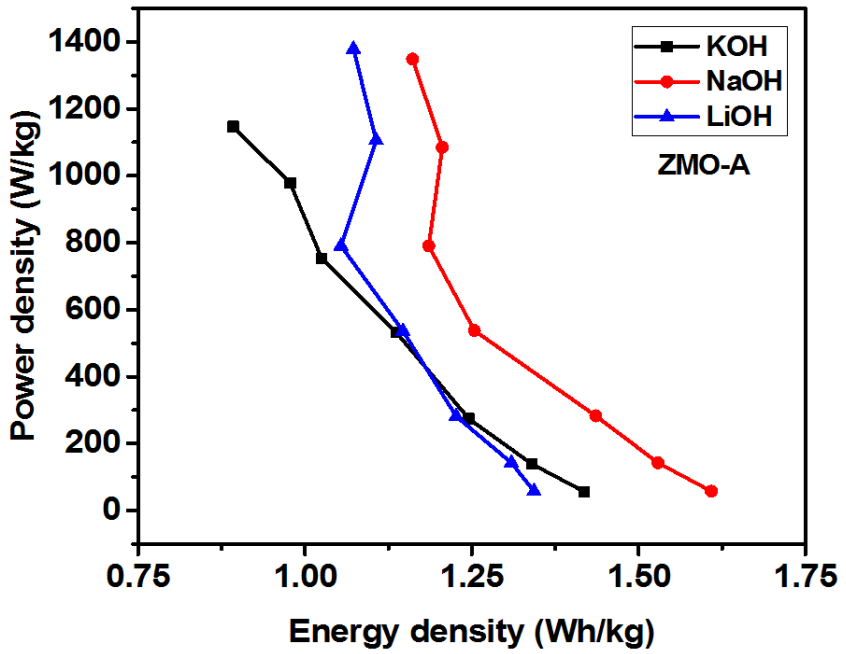

Figure 3.88: Power density versus energy density plots for ZMO-A in various electrolytes.

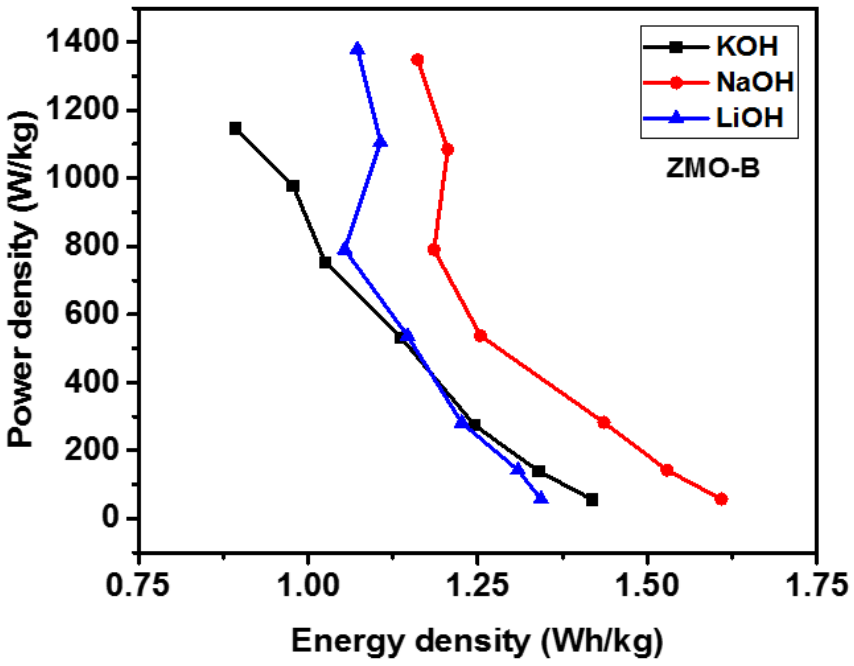

Figure 3.89: Power density versus energy density plots for ZMO-B in various electrolytes.

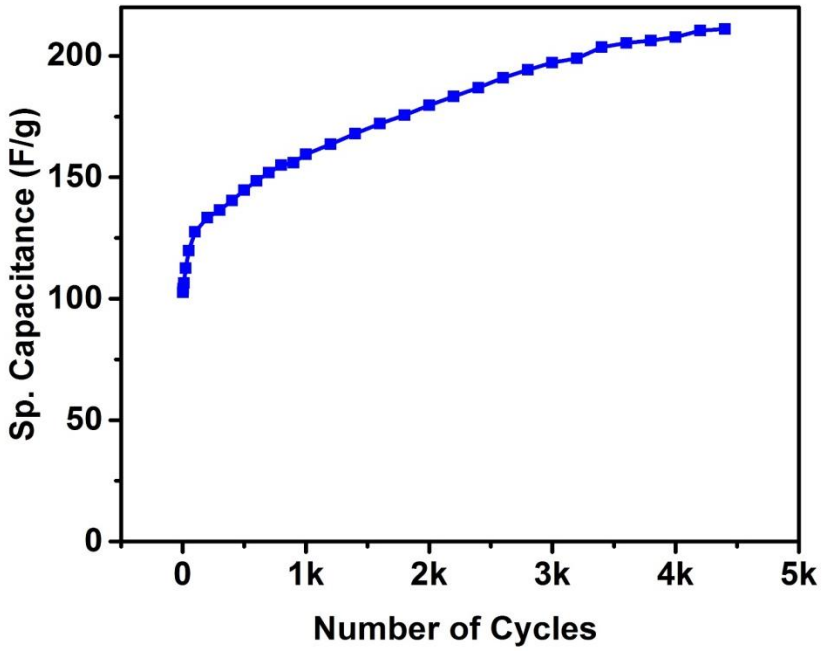

Figure 3.90: Variation of specific capacitance with number of charge-discharge cycles in NaOH electrolyte for CMO-B electrode.

3.3.2. Electrochemical Behavior Of The Device:

The symmetrical supercapacitor device was fabricated using $CoMn_2O_4$ tube-in-tube and the performance of the device was studied using cyclic voltammetry and electrochemical impedance spectroscopy (EIS). In addition to room temperature measurements, the effect of temperature on the electrochemical properties of the device was investigated.

The cyclic voltammograms of the device at room temperature at various scan rates are shown in Figure 3.91. As observed in the CV curves of the device, the shape and nature of the voltammogram was nearly identical even at higher scan rates, suggesting high electrochemical stability of the fabricated device. Additionally, the shape of the voltammogram is observed to be near rectangular in nature, suggesting near ideal capacitive behavior. The specific capacitance as a function of scan rate for the supercapacitor device in 3 M NaOH electrolyte is shown in Figure 3.92. It is seen that charge storage capacity of the device decreases with an increase in scan rate.

Cyclic voltammograms of the device at various temperatures in shown in Figure 3.93. The CV curves were still observed to be near rectangular in shape and the shape was retained even at higher temperature, suggesting high temperature stability of the device. The area of voltammogram was observed to increase with an increase in temperature indicating improvement in charge storage capacity with temperature. About 75% improvement in charge storage capacity was observed by increasing temperature from 10 to 70^{o} C. The effect of temperature on the charge storage capacity

of the device is shown in Figure 3.94. Based on the results, it can be concluded that the supercapacitor devices based on metal oxide nanofibers could be used in a wide temperature range with improved properties.

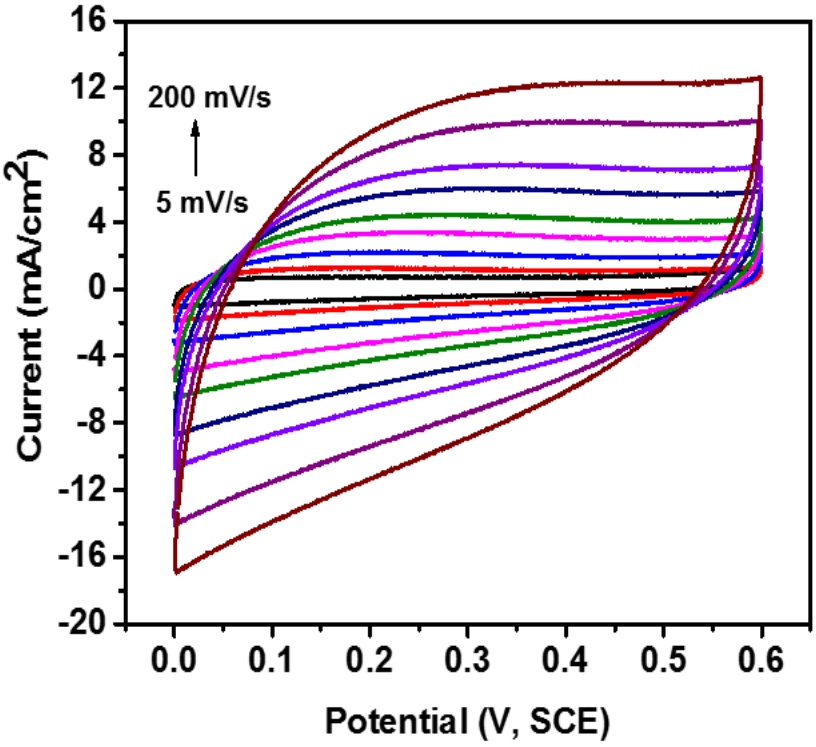

Figure 3.91: Cyclic voltammograms of the device at room temperatures in various scan rates.

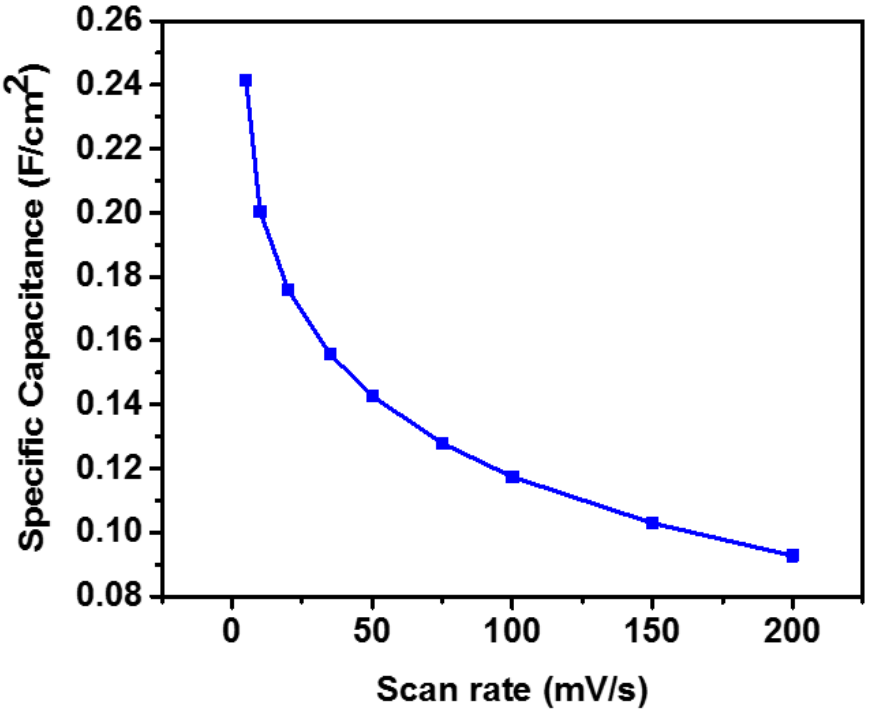

Figure 3.92: specific capacitance as a function of scan rate for the device in 3 M NaOH electrolyte.

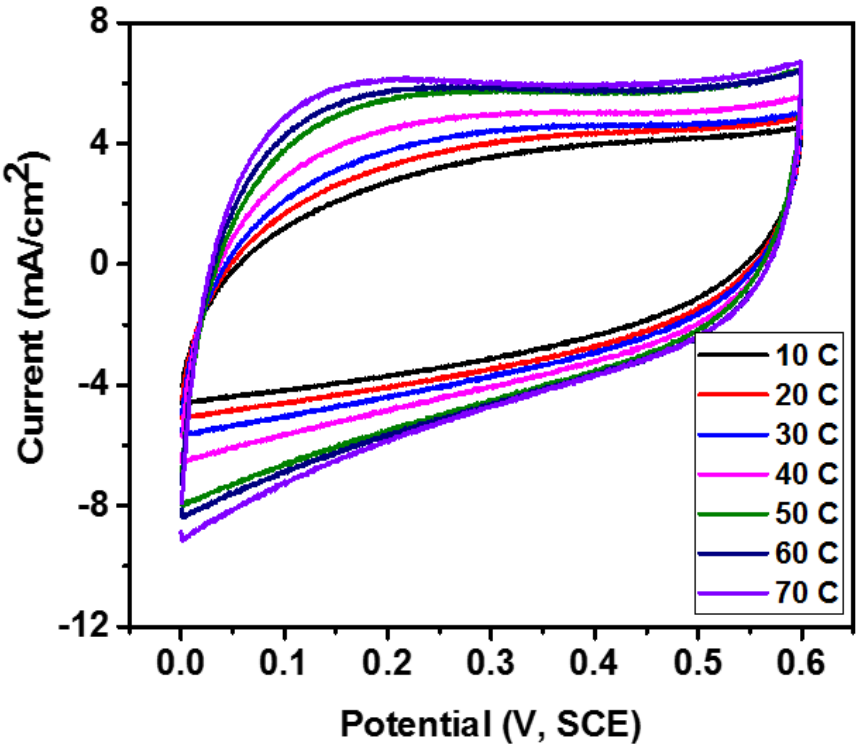

Figure 3.93: Cyclic voltammograms of the device at various temperatures.

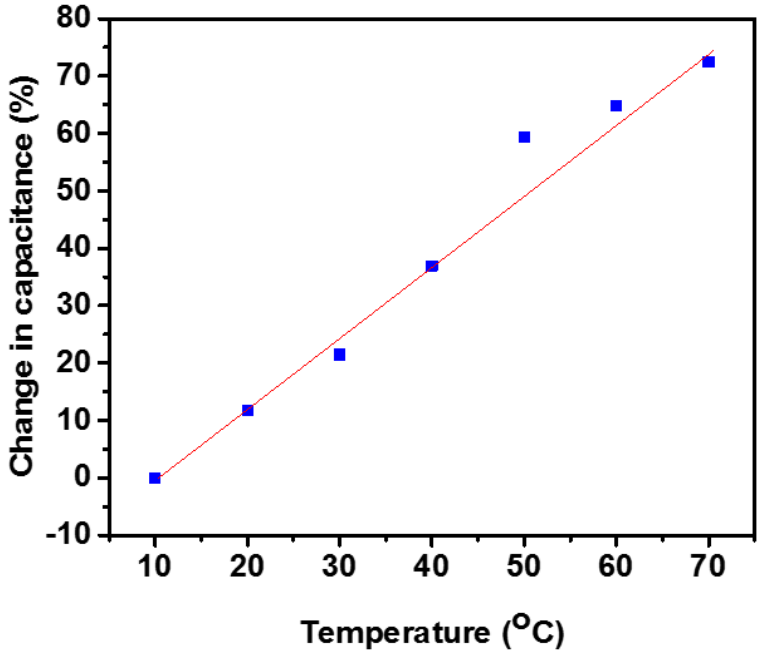

Figure 3.94: % change in specific capacitance of the device versus temperatures.

Figure 3.95 shows the galvanostatic charge-discharge characteristics of the device at various temperature in 3M NaOH electrolyte. As seen in this figure, the potential-time curves are almost symmetrical at all temperatures indicating the high charge-discharge stability of the device. In addition, the discharge time and thus the charge storage capacity was observed to increase with increasing temperature. Figure 3.96 shows the improvement in the specific capacitance of the device with increased temperatures based on the charge-discharge data. As seen in the figure, about 55% improvement in the charge storage capacity was observed by increasing temperature from 10° C to 70° C.

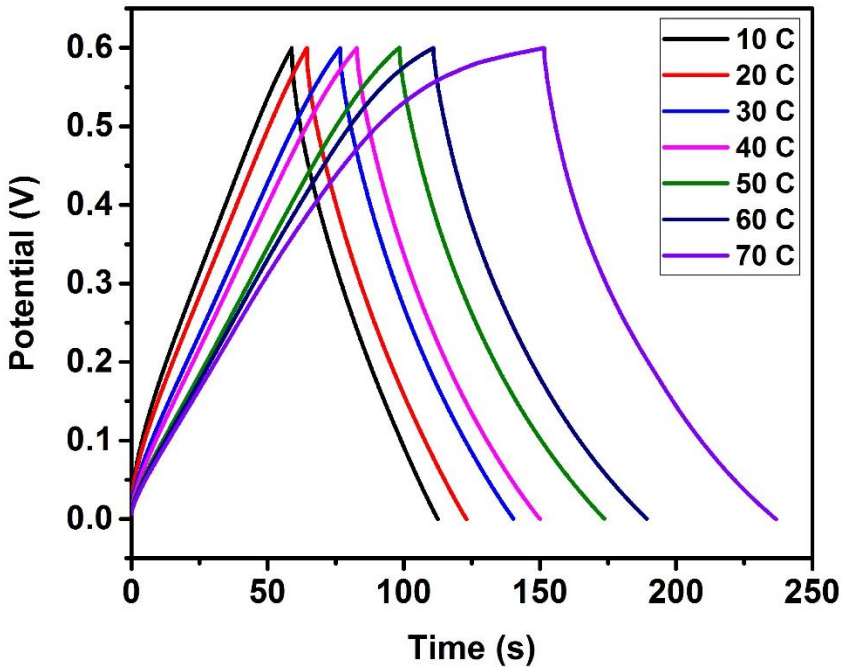

Figure 3.95: Galvanostatic charge-discharge characteristics of CMO-B device at various applied temperatures in 3M NaOH electrolyte.

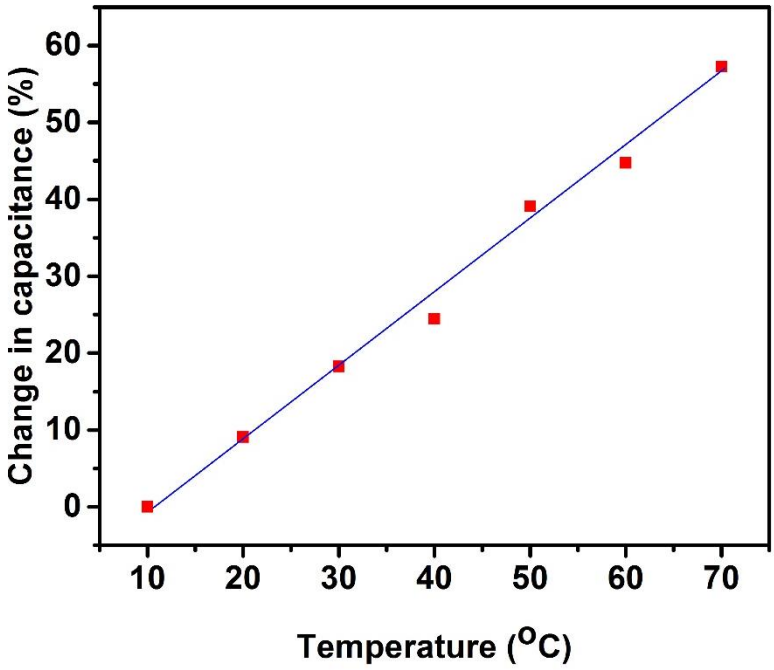

Figure 3.96: % change in specific capacitance of the device versus temperatures.

Electrochemical impedance spectroscopy (EIS) was conducted to analyze the internal resistance of the device and to determine the effect of temperature on the resistive and capacitive properties. The EIS spectra of the device at various temperatures are shown in Figure 3.97. As seen in the figure, the equivalent series resistance (ESR) of the device decreases with increase in temperature. The decrease in the ESR value might be related to the higher mobility of the ions in the electrolyte which increases the conductivity of the electrolyte [29]. It was also observed that impedance decreases with an increase in temperature, as seen in Figure 3.98.

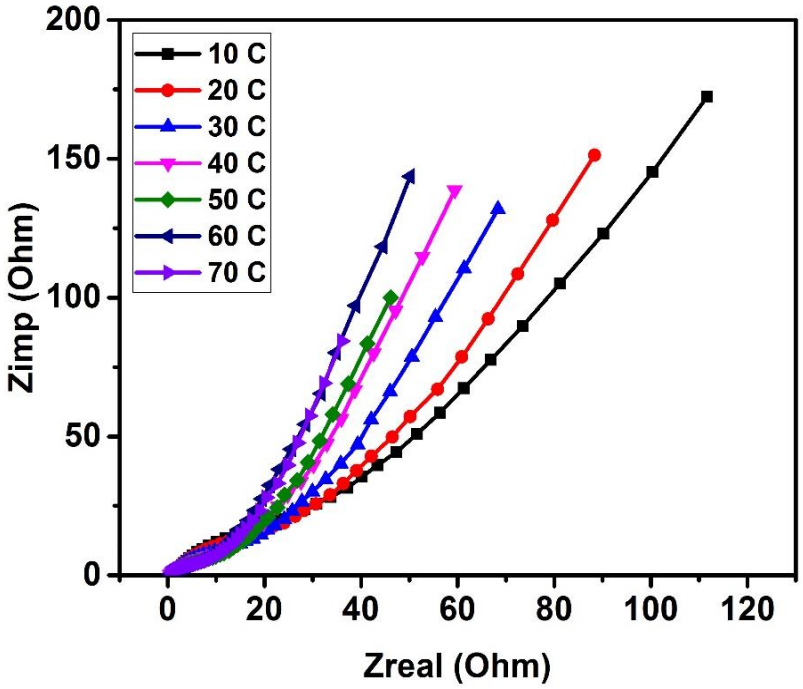

Figure 3.97: Z_{im} versus Z_{re} plots of the device at various temperatures.

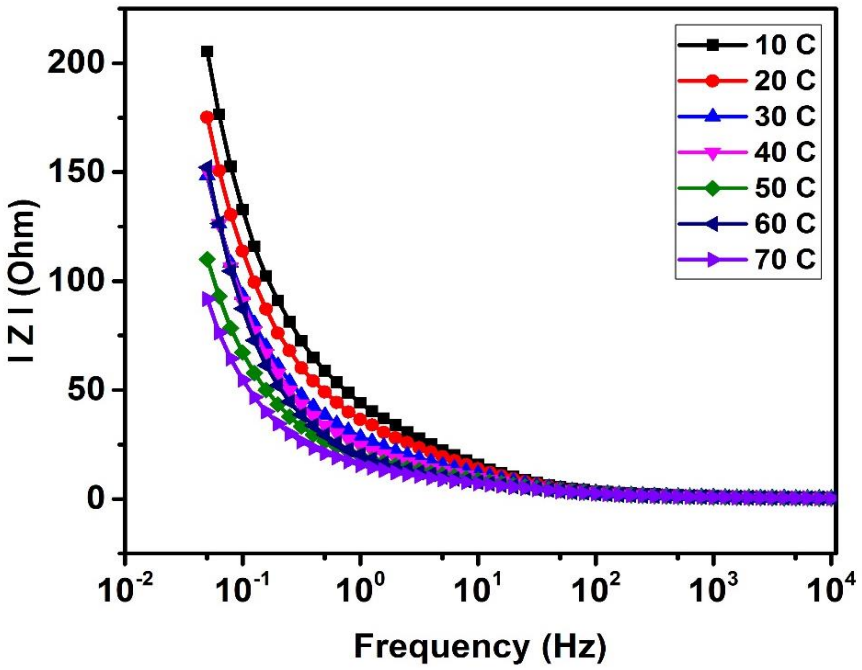

Figure 3.98: Variation of impedance as a function of frequency and temperature.

CHAPTER IV

CONCLUSION

In summary, we have used an electrospinning technique to synthesize metal oxide nanofibers such as $CoMn_2O_4$, $NiMn_2O_4$, and $ZnMn_2O_4$. It was observed that the heating rate during calcination affected the morphology of the nanofibers. The synthesized metal oxide based nanofibers were structurally characterized using X-ray diffraction, scanning electron microscopy and energy-dispersive X-ray spectrometry. Using scanning electron microscopy, it was discovered that adjusting the precursor polymers and heating rates provided three different morphologies with high surface areas. An Energy-dispersive X-ray spectrometer was used to further confirm the $CoMn_2O_4$, $NiMn_2O_4$, and $ZnMn_2O_4$ nanofibers' formation. X-ray diffraction was used to study the phase purity and crystallinity of the samples. It was observed that all the synthesized metal oxides were phase pure. The crystallite size of the $CoMn_2O_4$, $NiMn_2O_4$, and $ZnMn_2O_4$ nanofibers was estimated using XRD data. The average crystallite size of all the samples was in the range of 19.3 to 35.7 nm.

Electrochemical studies were performed to measure the effect of morphologies and electrolytes on the charge storage capacity of $CoMn_2O_4$, $NiMn_2O_4$, and $ZnMn_2O_4$

nanofibers. Using cyclic voltammetry and galvanostatic charge-discharge measurements, the potential application of the $CoMn_2O_4$, $NiMn_2O_4$, and $ZnMn_2O_4$ nanofibers for the supercapacitor applications was tested. The cyclic voltammograms of $CoMn_2O_4$, $NiMn_2O_4$, and $ZnMn_2O_4$ nanofibers showed pseudocapacitance behavior with the presence of a pair of redox peaks. It was observed that the specific capacitance of cobalt sulfides depends on scan rate. The specific capacitance was decreasing with increasing scan rate. The specific capacitance also depended on the morphology of the nanofibers and the electrolyte used. The highest specific capacitance of 120 F/g for sample CMO-B was observed in 3 M NaOH electrolyte. The cyclic stability test confirmed a remarkable long-term electrochemical stability of $CoMn_2O_4$. The electrochemical properties were further analyzed using galvanostatic charge-discharge measurements. The specific capacitance of electrospun nanofiber was observed to decrease with increasing current density. A maximum specific capacitance of 53 F/g was observed in 3 M NaOH solution for CMO-B sample. The electrochemical properties of metal oxides nanofibers were tested at higher temperatures to study their behavior. We observed about 75% improvement in the charge storage capacity of the supercapacitor device with increase in temperature in temperature from 10 to 70 ^{o}C.

Our studies suggest that nanofibers of metal oxides such as $CoMn_2O_4$, $NiMn_2O_4$, and $ZnMn_2O_4$ nanofibers could be grown using electrospun technique for their applications in supercapacitor device for wide temperature applications.

REFERENCE

1. R. Signorelli, D. C Ku, J. G. Kassakian, J. E. Schindall, Electrochemical Double-Layer Capacitors Using Carbon Nanotube Electrode Structures, DSpace MIT, 11 (2009) 1837-1847.
2. A. B. Iozzo, Michael Tong, Gang Wu, Edward P. Furlani, Numerical Analysis of Electric Double Layer Capacitors with Mesoporous Electrodes: Effects of Electrode and Electrolyte Properties Dante, The Journal of Physical Chemistry, 45 (2015) 25235-25242
3. B. E. Conway, Electrochemical Supercapacitors: Scientific Fundamentals and Technological Applications, Springer, (1999) 689.
4. R. Kotz, M. Carlen, Principles and applications of electrochemical capacitors, Electrochimica Acta, 45(2000) 2483-2498.
5. D. Y. Qu, H. Shi, Studies of activated carbons used in double-layer capacitors, Journal of Power Sources, 74 (1998) 99-107.
6. E. Frackowiak, K. Jurewicz, S. Delpeux, F. Béguin, Nanotubular Materials For Supercapacitors, Journal of Power Sources, 98 (2001) 822–825.
7. E. Frackowiak, F. Beguin, Carbon Materials For The Electrochemical Storage Of Energy In Capacitors, carbon, 39 (2001) 937–950.
8. S. R. Sivakkumar, A. G. Pandolfo ,Evaluation of lithium-ion capacitors assembled with pre-lithiated graphite anode and activated carbon cathode, Electrochimica Acta, 6 (2012) 280–287.

9. H. Zhou, Nanoscale perturbations of room temperature ionic liquid structure at charged and uncharged interfaces, ACS Nano 6 (2012) 9818–9827.
10. A. Kumar, K. Khasdeo, Nano-Fibers Application, International Journal of Nano Science and Nanotechnology, 4 (2013) 7-18.
11. Anthony L. Andrady, Science and Technology of Polymer Nanofibers, Wiley, (2008) 404.
12. S. Ramakrishna, K. Fujihara, W. Teo, T. Cheng Lim, Zuwei, An Introduction to Electrospinning and Nanofibers, World Scientific, (2005) 396.
13. P. Shengjie, L. Linlin, H. Yuxiang , S. Madhavi, C. Fangyi, J. Chen, S. Ramakrishna, Fabrication of Spinel One-Dimensional Architectures by Single-Spinneret Electrospinning for Energy Storage Applications, ACS Nano, 9 (2015) 1945-1954.
14. L. Eunhee, L. Taemin, S. Byeong, Electrospun nanofiber of hybrid manganese oxides for supercapacitor: Relevance to mixed inorganic interfaces, Journal of Power Sources, 255 (2014) 335–340.
15. B. Rena, M. Fana, Q. Liua, J. Wanga, D. Songa, X. Bahia, Hollow NiO nanofibers modified by citric acid and the performances as supercapacitor electrode, Electrochimica Acta, 92 (2013) 197–204.
16. Y. Wua, R. Balakrishnaa, M. V. Reddyb, A. Sreekumaran Naira, B. V. R. Chowdarib, S. Ramakrishnaa, Functional properties of electrospun NiO/RuO2 composite carbon nanofibers, Journal of Alloys and Compounds, 517 (2012) 69–74.

17. Z. Donga, J. Kennedyb, Yiquan Wua, Electrospinning materials for energy-related applications and devices, J. Power Sources, 196 (2011) 4873-4885.
18. J. Gan Wang, Y. Yang, Z. Hong Huang, F. Kang a, A high-performance asymmetric supercapacitor based on carbon and carbon–MnO2 nanofiber electrodes, Nano letter, 11 (2013) 4438-4442.
19. H. Zhang, S. C. Wang, D. Xue, Q. Chen, Z. C. Li, Preparation of nanocrystalline CeO 2 by nanocasting with mesoporous silica, Journal of Physics: Conference Series, 152 (2009) 012070.
20. J. Gomez, E. E. Kalu, High-performance binder-free Co–Mn composite oxide supercapacitor electrode, J. Power Sources, 230 (2013) 218-224.
21. S. H. Mujawar, S. B. Ambade, T. Battumur, R. B. Ambade, S. H. Lee, Electropolymerization of polyaniline on titanium oxide nanotubes for supercapacitor application, Electrochim. Acta, 56 (2011) 4462-4466.
22. F. Zhao, Y. Wang, X. Xu, Y. Liu, R. Song, G. Lu, Y. Li, Cobalt Hexacyanoferrate Nanoparticles as a High-Rate and Ultra-Stable Supercapacitor Electrode Material, ACS Applied Materials & Interfaces, 6 (2014) 11007-11012.
23. L. J. Xie, J. F. Wu, C.-M. Chen, C. M. Zhang, L. Wan, J. L. Wang, Q. Kong, C. X. Lv, K. X. Li, G. H. Sun, A novel asymmetric supercapacitor with an activated carbon cathode and a reduced graphene oxide–cobalt oxide nanocomposite anode, J. Power Sources, 242 (2013) 148-156.

24. E. Mitchell, F. De Souza, R.K. Gupta, P.K. Kahol, D. Kumar, L. Dong, B.K. Gupta, Probing on the hydrothermally synthesized iron oxide nanoparticles for ultra-capacitor applications, Powder Technol., 272 (2015) 295-299.
25. E. Mitchell, A. Jimenez, R.K. Gupta, B.K. Gupta, K. Ramasamy, M. Shahabuddin, S.R. Mishra, Ultrathin porous hierarchically textured NiCo2O4-graphene oxide flexible nanosheets for high-performance supercapacitors, New J. Chem., (2015).
26. C. Xiang, M. Li, M. Zhi, A. Manivannan, N. Wu, A reduced graphene oxide/Co_3O_4 composite for supercapacitor electrode, J. Power Sources, 226 (2013) 65-70.
27. W. Tang, S. Tian, L.L. Liu, L. Li, H.P. Zhang, Y.B. Yue, Y. Bai, Y.P. Wu, K. Zhu, Nanochain LiMn2O4 as ultra-fast cathode material for aqueous rechargeable lithium batteries, Electrochem. Commun, 13 (2011) 205-208.
28. M.-C. Liu, L.-B. Kong, X.-J. Ma, C. Lu, X.-M. Li, Y.-C. Luo, L. Kang, Hydrothermal process for the fabrication of CoMoO4 middle dot]0.9H2O nanorods with excellent electrochemical behavior, New J. Chem., 36 (2012) 1713-1716.
29. W. Li, K. Xu, L. An, F. Jiang, X. Zhou, J. Yang, Z. Chen, R. Zou, J. Hu, Effect of temperature on the performance of ultrafine MnO2 nanobelt supercapacitors, Journal of Materials Chemistry A, 2 (2014) 1443-1447.